Joule

Article

Hybrid solvating electrolytes for practical sodium-metal batteries

Graphical abstract

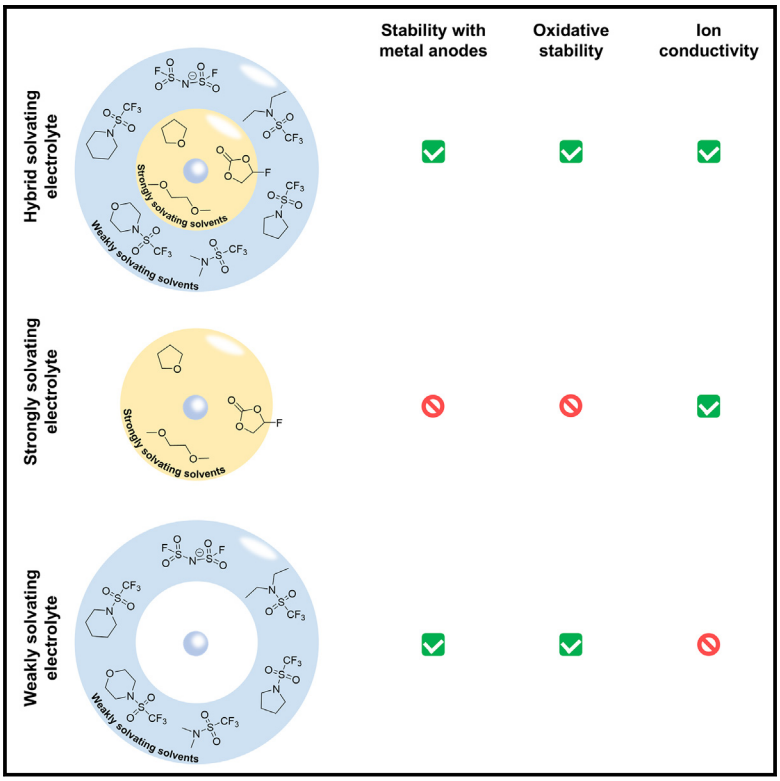

Highlights

- Strong and weak solvent pairs demonstrate strong beyond-rule-of-mixture effects
- Fifty HSEs are prepared to reveal distinct selection rules for each solvent types
- HSEs enable reversible fast cycling of metal anodes with high-voltage cathodes

Authors

Weiyin Chen, Jin-Sung Park, Choah Kwon, ..., Yang Shao-Horn, Jeremiah A. Johnson, Ju Li

Correspondence

liju@mit.edu

In brief

We report hybrid solvating electrolytes (HSEs), which are composed of both strong and weak solvents of sodium salts. The solvent pairs can achieve a good balance between the low polarization and high redox stability, demonstrating strong beyond-rule-of-mixture effects. A model HSE with DMTMSA and THF demonstrates extraordinarily stable cycling performance against $Na_3V_2(PO_4)_3$ and $Na_{0.44}MnO_2$ cathodes and Na-metal anode. We studied 50 HSEs and found distinct selection requirements for each solvent type to guide the electrolyte design for practical alkali-metal batteries.

Chen et al., 2025, Joule 9, 101811
March 19, 2025 © 2024 Elsevier Inc. All rights are reserved, including those for text and data mining, AI training, and similar technologies.
https://doi.org/10.1016/j.joule.2024.101811

CellPress

Please cite this article in press as: Chen et al., Hybrid solvating electrolytes for practical sodium-metal batteries, Joule (2024), https://doi.org/10.1016/j.joule.2024.101811

Joule

CellPress

Article

Hybrid solvating electrolytes for practical sodium-metal batteries

Weiyin Chen,[1,2] Jin-Sung Park,[1,2,5,6] Choah Kwon,[1,2] Christian O. Plaza-Rivera,[2] Chia-Wei Hsu,[2] Jason Khoi Phong,[2] Landon James Kilgallon,[3] Daniel Wang,[4] Tao Dai,[1,2] So Yeon Kim,[1,2] Guanzhou Zhu,[1,2] Yifan Gao,[1,2] Zhichu Ren,[2] Zhen Zhang,[2] Hyojun Lim,[1,2] Yang Shao-Horn,[2,4] Jeremiah A. Johnson,[3] and Ju Li[1,2,7,*]

[1]Department of Nuclear Science and Engineering, Massachusetts Institute of Technology, Cambridge, MA 02139, USA
[2]Department of Materials Science and Engineering, Massachusetts Institute of Technology, Cambridge, MA 02139, USA
[3]Department of Chemistry, Massachusetts Institute of Technology, Cambridge, MA 02139, USA
[4]Department of Mechanical Engineering, Massachusetts Institute of Technology, Cambridge, MA 02139, USA
[5]Department of Materials Science and Engineering, Ajou University, Suwon 16499, Republic of Korea
[6]Department of Energy Systems Research, Ajou University, Suwon 16499, Republic of Korea
[7]Lead contact
*Correspondence: liju@mit.edu
https://doi.org/10.1016/j.joule.2024.101811

CONTEXT & SCALE Sodium-metal batteries show great application potential as next-generation energy storage technology due to the natural abundance and low cost of sodium. However, the incompatibility of common electrolytes with high-reactivity sodium-metal anodes and cathodes poses performance limitations. Here, we invented hybrid solvating electrolytes (HSEs), composed of both strong and weak solvents of sodium salts, to modify the key physical and chemical properties of the electrolytes. We found that HSEs demonstrate strong beyond-rule-of-mixture effects and can achieve a good balance between the low polarization and high redox stability. We demonstrated that one model HSE can sustain highly reversible sodium-metal cycling at 3.0 mA cm^{-2} and enable the extraordinarily stable cycling performance against the sodium cathodes up to 4.0 V. Our work presents a guiding principle for electrolyte design to enable practical alkali-metal batteries.

SUMMARY

Sodium-metal batteries could be competitive against Li-metal batteries, but their applications depend on the stability of electrolytes against sodium-metal anodes and cathodes simultaneously. Here, we propose hybrid solvating electrolytes (HSEs), composed of both strongly and weakly solvating solvents of sodium salts, to tune the solubility, solvation structure, and electrochemical decomposition properties. Fifty HSEs are prepared using the pre-screened candidate molecules, validating the mixture selection requirements and correlations between salt/solvent types and their mixture-dependent performance, including oxidative stability, Coulombic efficiency, and cycling overpotential. A model hybrid solvent formed by mixing weakly solvating N,N-dimethyltrifluoromethane sulfonamide (DMTMSA) with strongly solvating tetrahydrofuran (THF) demonstrates strong beyond-rule-of-mixture effects, showing extraordinarily stable cycling performance against $Na_3V_2(PO_4)_3$ and $Na_{0.44}MnO_2$ cathodes and Na-metal anode. Spectroscopic analysis and molecular dynamics simulations reflect the corresponding change in ion-dipole interaction and solvation structures. The strong-weak hybrid solvating principle for electrolyte design enables practical alkali-metal batteries.

INTRODUCTION

Sodium batteries offer great potential as next-generation energy storage technologies for electric vehicles and the grid.[1–3] Besides the natural abundance (>1,000-fold) and lower cost (<1%)[4,5] of sodium compared with lithium minerals, the existing infrastructure for lithium batteries can be adapted to achieve large-scale production.[6] A sodium-metal anode could be the ultimate candidate for sodium rechargeable batteries, due to its high theoretical specific capacity (1,165 mA h g^{-1}) and low redox potential (−2.714 V versus the standard hydrogen electrode).[7,8]

The incompatibility of common electrolytes with high-reactivity sodium-metal anodes[9–11] and cathodes[12–14] poses performance limitations. The equilibrium potentials of these electrodes

All rights are reserved, including those for text and data mining, AI training, and similar technologies.

are outside the stable voltage window of most electrolytes, leading to electrolyte decomposition and insoluble products atop the electrodes.[15,16] On the cathode side, the interfacial reaction can also induce irreversible surface phase transformation of cathode particles and polarization buildup,[17,18] leading to gradual capacity decay. On the anode side, further chemo-mechanical instability of the so-called solid electrolyte interphase (SEI)[5,19] during metal plating and stripping leads to morphological degradations and isolated metals,[5] accelerated consumption of the electrolyte, low reversibility, and a short cycle life.[20,21] Moreover, the presence of metallic protrusions can bridge the electrodes, resulting in internal short circuit and thermal runaway.

Recent research in sodium-metal batteries (SMBs) has focused on the electrodeposition and stripping behavior of sodium metal,[22,23] and the structure and composition of the SEI.[5,21] To alleviate the accumulation of isolated Na^0 and improve Coulombic efficiency (CE), various strategies have been proposed, including electrolyte engineering,[13] interface functionalization,[8,24] porous electrode development,[25] and cycling protocol optimization.[21,26] For the electrolyte, different salts,[2,13] solvents,[1,7] additives,[9] and their combinations[3] have been applied to achieve wider redox voltage tolerance and cycling reversibility. As shown in Figure S1, single-salt-single-solvent electrolytes suffer from the trade-off between low polarization and high redox stability. The conventional electrolytes use strongly cation-solvating solvents, which enhance the cation-dipole interaction and facilitate the formation of solvent-separated ion pairs (SSIPs), promoting high solubility and ionic conductivity.[27] Unfortunately, the free solvent molecules can be vulnerable to parasitic reactions with the electrodes during continuous cycling.[9] By contrast, weakly solvating solvents allow the incorporation of anions within the first solvation sheath,[28] contributing to the accumulation of contact-ion pairs (CIPs) and ion aggregates (AGGs) with higher electrochemical stabilities.[29,30] This also enhances the chance of anion decomposition, which primarily forms inorganic-rich passivation products[31] that are more stable and robust than the organic-rich decomposition products of solvent molecules in traditional low-concentration electrolytes. However, weakly solvating solvents can cause insufficient salt solubility and cation conductivity, limiting practical cycling performance at current densities $\geq$1 mA cm^{-2}.[32] Additionally, CIP/AGG and inorganic-rich passivation[31] can be achieved by increasing the salt to solvent ratios to form high-concentration electrolytes (HCEs).[1] To improve the rate performance, non-solvating diluents can also be added to form localized HCEs (LHCEs),[31] which not only reduces the viscosity and increases the ionic conductivity of HCEs, but also maintains CIP/AGG.

It can be challenging to balance the salt association degree (CIP/AGG versus SSIP) and solvation ability with just one solvent.[32,33] This becomes even more obvious when the cations are changed from Li^+ to Na^+. For example, *N,N*-dimethyltrifluoromethane sulfonamide (DMTMSA) is a promising weak solvent to dissolve lithium bis(fluorosulfonyl)imide (LiFSI) for stable high-voltage lithium-metal batteries,[33] and the solubility reaches ~1.7 mol kg^{-1}. By contrast, its counterpart NaFSI shows a limited solubility of ~0.2 mol kg^{-1} within DMTMSA and 1 mol kg^{-1} NaFSI forms a turbid suspension as shown in Figure S2. Tuning the solvation ability of electrolyte solvents through molecular design using partial halogenation,[34] methylation,[35] cyanation,[36] and so on[37] to match the association degree of each salt is one way to prepare electrolytes with increased stability, but it can be difficult to optimize such solvents through molecular modifications alone due to limited substituent choices.[32] For example, the solvation ability of a mono-fluorinated solvent can still be too strong, while the tri-fluorinated solvent becomes non-solvating.[32,38]

In this work, we propose hybrid solvating electrolytes (HSEs, Figure 1A), including a mixture of strongly and weakly solvating solvents that can co-coordinate with Na^+ to form the hierarchical solvation structure and achieve fine-tuning of the solvation ability accordingly. Compared with strong-strong solvent pairs in conventional dilute electrolytes and strong-antisolvent solvent pairs in LHCEs (Figure 1A), there is a larger material design space with HSEs, as different strong-weak solvent pairs with varied ratios can be explored (Figure 1B). Besides, most LHCEs choose common ethers as strong solvents, due to the polarity mismatch and immiscibility between fluorinated ether-based diluents and other HCEs, such as fluoroethylene carbonate (FEC)-based HCEs. However, there is no such limitation for HSEs, and different strong solvents, including ethers, carbonates, and sulfones, can be used in a wide molar ratio with weak solvents. Furthermore, the salt concentration of as-prepared HSEs can be as low as ~0.8 mol kg^{-1}, which is lower than common LHCEs used for SMBs and shows potential economic advantages. Fifty HSEs were prepared by mixing various pre-labeled solvent molecules and changing the molar ratio among solvents, revealing the essential selection requirements for each solvent type. The weakly solvating solvents can determine the redox stabilities and cycling polarization, while the strongly solvating solvents enable the gradual tuning of these properties. For strong-weak solvent pairs, we find that the electrochemical performance, including CE and overpotential of sodium-metal plating and stripping, follows a volcano trend, giving an optimal design of HSEs. Spectroscopic analysis and molecular dynamics (MD) simulations reveal the change of cation-dipole interaction and corresponding primary solvation sheath, leading to distinct cycling behavior for sodium metal. Using a model HSE comprising tetrahydrofuran (THF) and DMTMSA with NaFSI, a stable CE of 99.40% can be achieved at 3.0 mA cm^{-2} for Na||Cu cells. This HSE also enables Na||$Na_3V_2(PO_4)_3$ cells with a cycling rate of 5 C (5.0 mA cm^{-2}) over 2,000 cycles and Na||$Na_{0.44}MnO_2$ cells over 1,000 cycles. This design concept can also be extended to prepare HSEs for lithium-metal batteries. Our work presents a guiding principle for electrolyte design to enable practical alkali-metal batteries.

RESULTS

Design concept of HSEs

The solvents are pre-screened based on descriptors including donor number (DN), electrostatic potential (ESP), and polar area ratio relative to the total accessible surface as listed in Table S1, which were found to be effective in distinguishing strongly and weakly solvating solvents and antisolvents[39–41] as plotted in Figure 1C and discussed in Note S1. The strong-weak solvent pairs can optimize the salt solubility and electrolyte viscosity, which improves the cation conductivity without

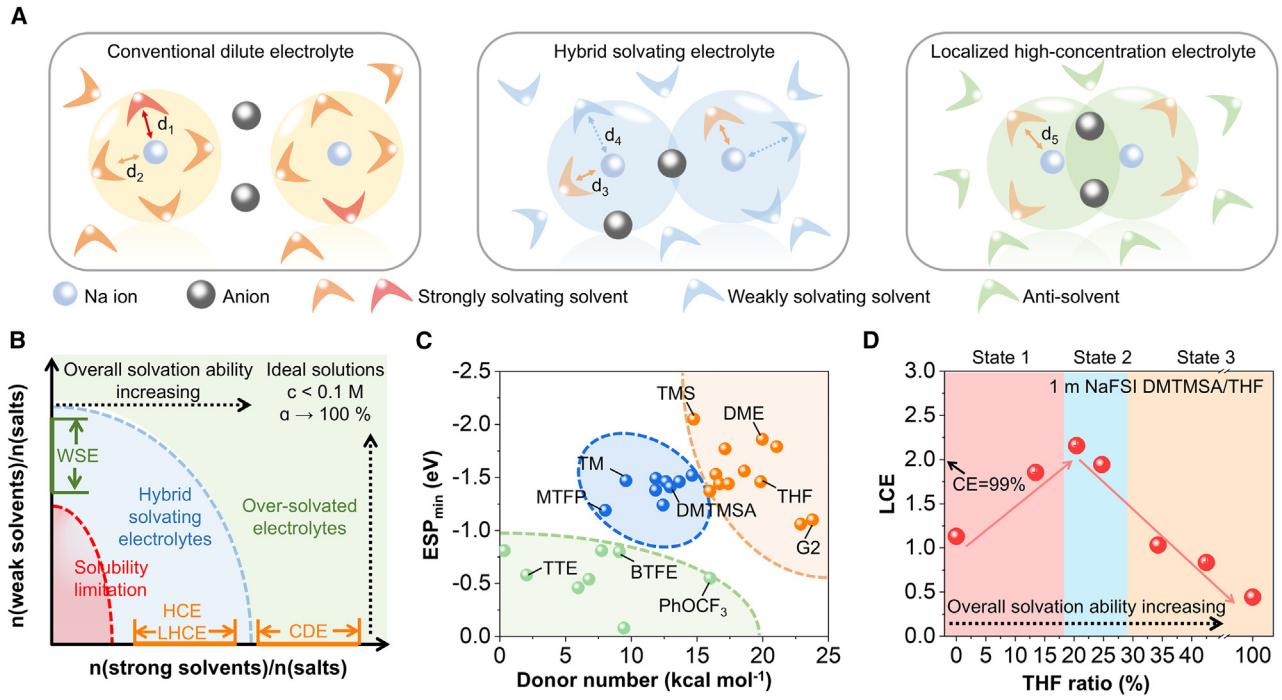

Figure 1. Design concept of hybrid solvating electrolytes

(A) Comparison among conventional dilute electrolytes with strong-strong solvent pairs, localized high-concentration electrolytes with strong-antisolvent pairs, and hybrid solvating electrolytes combined with strongly and weakly solvating solvents.

(B) Scheme about the design space of hybrid solvating electrolytes.

(C) The donor number and electrostatic potential of various solvents. Green, blue and orange regions represent antisolvents, weakly and strongly solvating solvents, respectively.

(D) Components-properties relationships between THF ratio and logarithm CE for hybrid solvating electrolytes.

WSE, weakly solvating electrolytes; CDE, conventional dilute electrolyte; HCE: high-concentration electrolyte; LHCE, localized high-concentration electrolyte; ESP: electrostatic potential; LCE $\equiv -\log_{10}(1 - \mathrm{CE})$. Error bars reflect the standard deviations from at least three individual cells.

causing phase separation or compromising electrochemical stability against sodium-metal anodes and cathodes. Thereupon, the optimization of key electrochemical parameters, such as oxidative voltage, CE, and overpotential can be achieved by fast initial screening and subsequent fine-tuning.

DMTMSA and THF were chosen for a demonstration since DMTMSA is a weakly solvating solvent with favorable decomposition products,[33] and THF can dissolve NaFSI to form a ~7 mol kg^{-1} solution.[1] By changing the molar ratio between DMTMSA and THF, the polarization curves of these electrolytes with 1 mol kg^{-1} NaFSI change correspondingly (Figure S3). The average CEs and cycling overpotentials (Figures S4 and S5) at 1.0 mA cm^{-2} over 100 cycles were calculated to evaluate their electrochemical performance. As the THF ratio increases, the average cycling overpotential first decreases from >600 to ~72 mV, and then increases to ~156 mV (Figure S6A). Moreover, the average CE initially increases from ~92.60% to ~99.30%, followed by a decrease to ~64.02% (Figures 1D and S6B), which is matched with the trend observed by using the Aurbach method at 1.0 mA cm^{-2} with an areal capacity of 1.0 mAh cm^{-2} (Figure S7) and can be explained by the solvation structure evolution as discussed below. The non-monotonic dependence between the average CEs and cycling overpotentials guided our HSE design, where the optimized molar ratio between DMTMSA and THF is 4:1 when NaFSI is used as the salt and is called "1 m NaFSI DMTMSA/THF" afterward.

Electrochemical evaluation of HSEs

To evaluate electrolytes, the Aurbach method was used to compare the Na-metal cycling reversibility at 1.0 mA cm^{-2}. The average CE reaches 99.32% for 1 m NaFSI DMTMSA/THF (Figure 2A), which is the highest Aurbach CE reported so far[42] and is much better than 1 m NaFSI THF (40.42%) and "1 m NaFSI" in DMTMSA (75.61%), both of which suffer from (soft) short circuits. Recent work has shown that formation cycle optimization can facilitate a more stable SEI with a higher average CE,[19] which was applied for 1 m NaFSI DMTMSA/THF. After precycling for a whole Aurbach cycle, the average CE measured by the Aurbach method can reach 99.72% at 1.0 mA cm^{-2} (Figure 2B). Weakly solvated DMTMSA cannot be replaced by the same amount of non-solvating diluent, such as 1,1,2,2-tetrafluoroethyl-2,2,3,3-tetrafluoropropyl ether (TTE), as confirmed by the precipitation of salt and the large polarization curve (Figure S8). Linear sweep voltammetry (LSV) was conducted using Na||stainless steel (SS) cells at a scan rate of 1.0 mV s^{-1}. 1 m NaFSI THF exhibited onset of oxidation at ~4.0 V (Figure 2C),

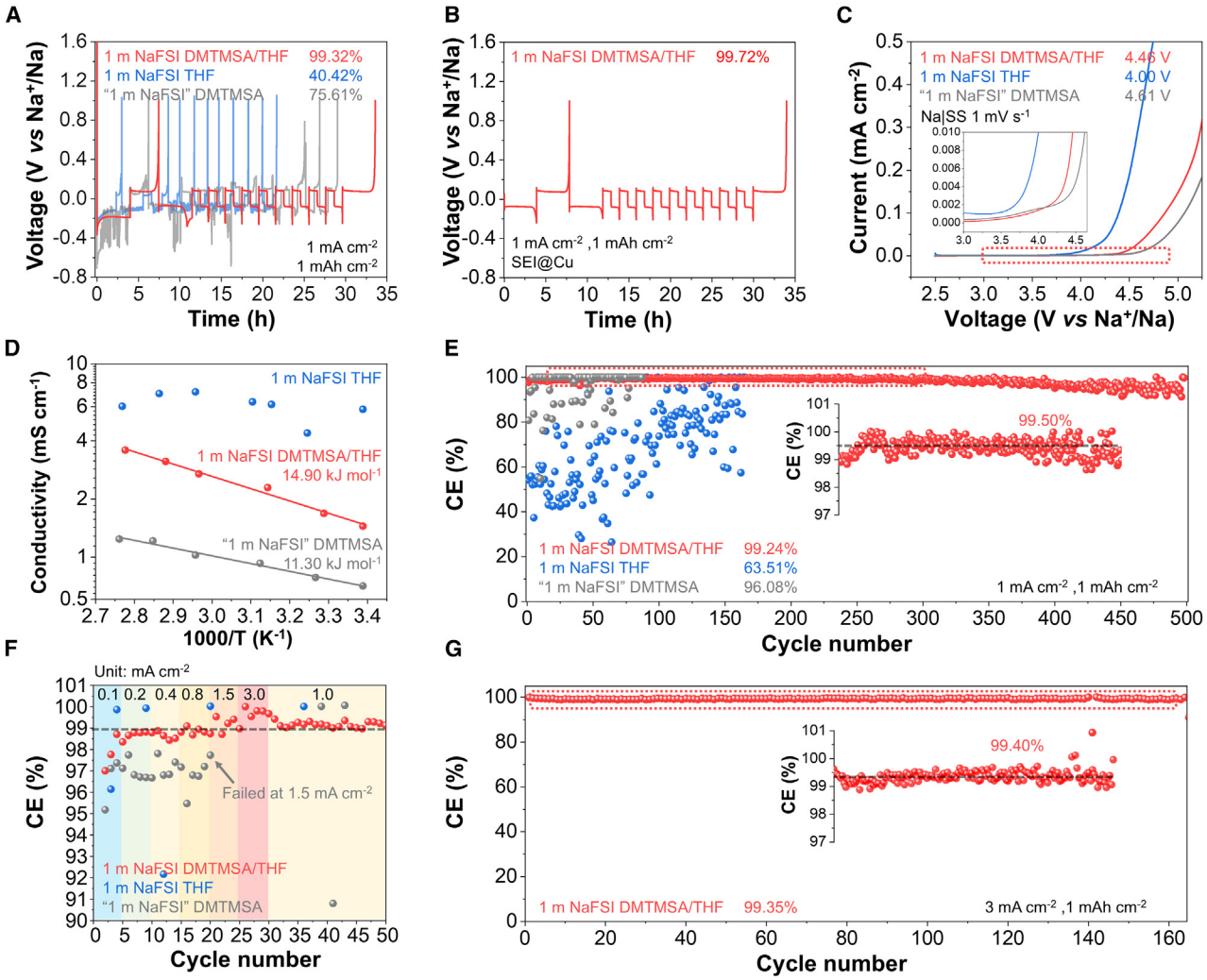

Figure 2. Electrochemical evaluation of hybrid solvating electrolytes

(A) Aurbach method measurement of Na^0 CE in Na||Cu half cells using different electrolytes.

(B) Aurbach method measurement of Na^0 CE using hybrid solvating electrolyte and precycled Cu with stable SEI.

(C) Oxidation stability of various electrolytes in Na||SS half cells. SS, stainless steel.

(D) Ionic conductivity of different electrolytes under various temperatures.

(E) Cycling performance of different electrolytes at 1.0 mA cm^{-2}. The inset shows the CE within the red dash region; the same below.

(F) Rate performance of various electrolytes with a fixed areal capacity of 1.0 mAh cm^{-2}.

(G) Cycling performance of hybrid solvated electrolyte at 3 mA cm^{-2}.

while 1 m NaFSI DMTMSA/THF was stable up to ~4.5 V, which is similar to the oxidative voltage of "1 m NaFSI" in DMTMSA at ~4.6 V. This enhanced stability suggests that THF molecules in our HSE are not "free" solvent molecules, but are coordinated to Na^+, increasing their stability toward oxidation.[1] The ionic conductivity was measured using electrochemical impedance spectroscopy (EIS) (Figure S9). The ionic conductivity of 1 m NaFSI DMTMSA/THF is ~220% greater than the DMTMSA-only electrolyte at room temperature (Figure 2D). The activation energy was calculated using the Arrhenius fit (Note S2). The value of 1 m NaFSI DMTMSA/THF was 14.90 kJ mol^{-1}, which is lower than common HCE and LHCE with only strongly solvating solvents.[42] It is noted that THF polymerization can happen after heat treatment or room-temperature storage in the case of 1 m NaFSI THF lacking DMTMSA, causing the inflection points for the ionic conductivity in Figure 2D, while the addition of DMTMSA prevents THF polymerization (Note S3; Figure S10). The viscosity of 1 m NaFSI DMTMSA/THF is ~5.3 cP at room temperature (Figure S11), which is close to the value of advanced electrolytes with similar salt concentrations,[31,33] and the value remains consistent for more than 25 days. The observed greater ionic conductivity and stability are important factors for achieving fast cycling (≥3.0 mA cm^{-2}) and high charging cut-off voltage (~4.0 V) SMBs.

Complete plating and stripping of sodium metal were used to measure cycling reversibility. 1 m NaFSI THF is unstable as the

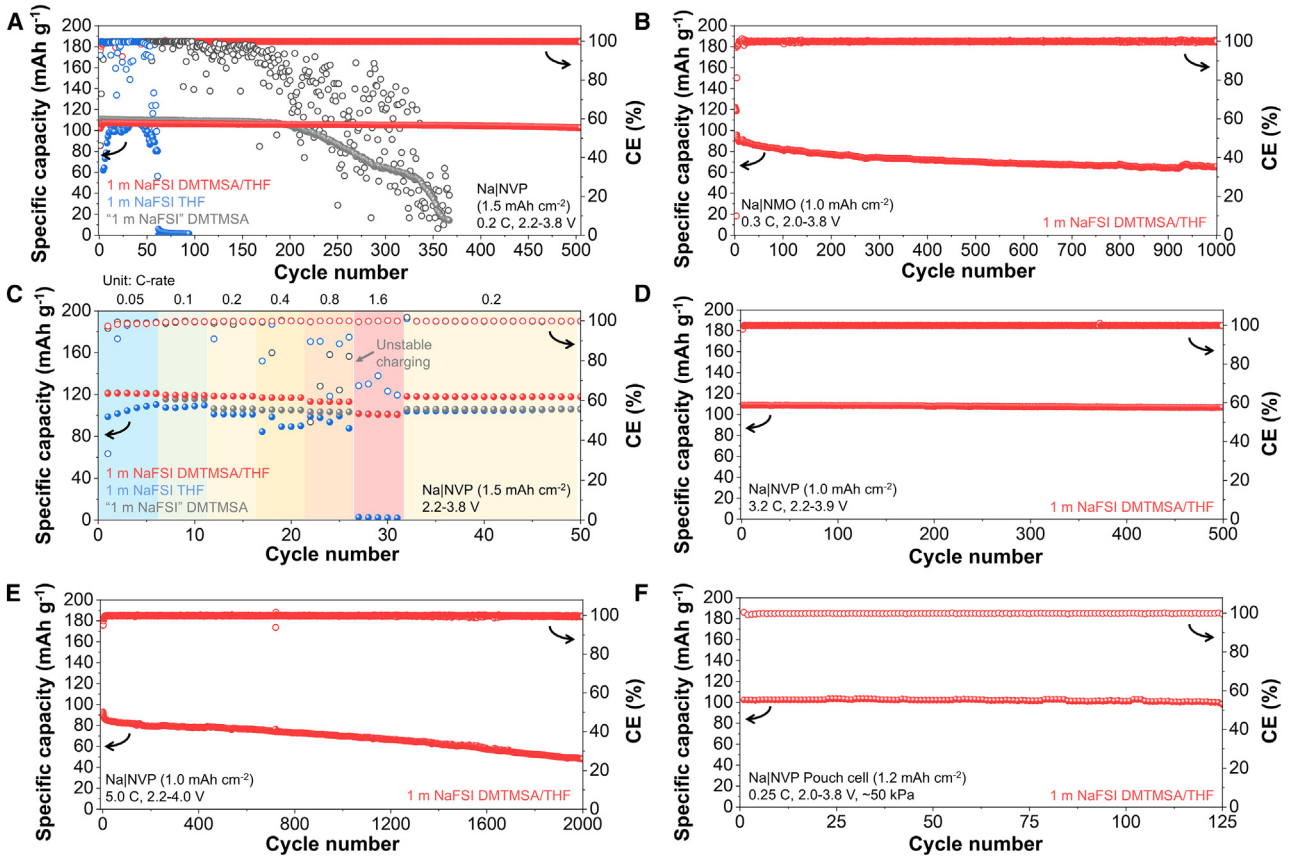

Figure 3. Electrochemical performance of hybrid solvating electrolytes

(A and B) Cycling performance of (A) $Na_3V_2(PO_4)_3$ and (B) $Na_{0.44}MnO_2$ cathode using hybrid solvating electrolyte.

(C) Rate performance of $Na_3V_2(PO_4)_3$ using various electrolytes.

(D and E) Fast cycling evaluation of $Na_3V_2(PO_4)_3$ cathode using hybrid solvating electrolyte.

(F) Cycling performance of $Na_3V_2(PO_4)_3$ cathode using hybrid solvating electrolyte and pouch cell configurations. Uniaxial pressure of ~50 kPa is provided for interfacial contacting.

CE fluctuates during long-term cycling using Na||Cu cells at 1.0 mA cm^{-2} (Figure 2E), while the CE fluctuation is less pronounced for the DMTMSA-only electrolyte, with an average CE of ~96.1% over 100 cycles. Short circuits happen in the subsequent cycles, as indicated by the voltage curves (Figure S12). By contrast, 1 m NaFSI DMTMSA/THF shows a higher initial CE of 95.8% and a rapid CE increase to >99.0% within the first 10 cycles, indicating fast activation for this HSE (Figure S13A). The CE remains at ~99.50% over 250 cycles, and stable cycling over 500 cycles is seen for three nominally identical Na||Cu cells (Figures 2E and S14), showing good reproducibility. The fast activation can be observed when the current density increases to 3.0 mA cm^{-2} and when the areal capacity increases to 3.0 mAh cm^{-2}. After only 5 and 2 cycles, respectively, the cycling CE exceeds 99.0% (Figure S13), which is the fastest activation observed thus far in this work and in the literature (Table S2). The fast activation suggests the rapid formation of a solid passivation layer and minimized gaseous and soluble products,[43] which is one of the important electrolyte design principles. The average CE is ~99.3% over 100 cycles with a stable cycling overpotential of ~80 mV using an areal capacity of 3.0 mAh cm^{-2} (Figure S15). The Cu current collector is characterized after electrochemical cycling tests, and there is no obvious corrosion using a 1 m NaFSI DMTMSA/THF electrolyte, as shown in Figure S16. For the Al current collector, the oxidative current is <0.03 mA cm^{-2} even at 6.0 V (Figure S17), and there was no noticeable morphology change before and after the oxidative test, as shown in scanning electron microscopy (SEM) images, which indicates the negligible corrosion of the Al current collector as well.

Rate performance was also conducted to evaluate this HSE. For 1 m NaFSI THF, poor cycling reversibility was observed at all current densities (Figure 2F); however, there is a relatively high CE of ~97% with a low cycling overpotential of <100 mV using a current density of <0.5 mA cm^{-2} for the DMTMSA-only electrolyte (Figure S18). When the current density reaches 1.5 mA cm^{-2}, a sharp voltage drop with a potential minimum of −2.4 V can be observed during the sodium-metal plating process, and soft short circuiting happens afterward. In contrast, 1 m NaFSI DMTMSA/THF shows stable cycling at 3.0 mA cm^{-2} with no obvious buildup of concentration polarization. As a result, the CE remains at ~99.4% over 165 cycles at 3.0 mA cm^{-2} with stable cycling overpotentials (Figures 2G and S19).

The cycling reversibility and oxidative stability make this HSE promising when paired with common sodium cathodes such as $Na_3V_2(PO_4)_3$ and $Na_{0.44}MnO_2$. As shown in Figures 3A and S20, sudden capacity loss and polarization buildup can be observed after 50 cycles for 1 m NaFSI THF in a Na||$Na_3V_2(PO_4)_3$ cell at 0.2 C rate (1 C ≡ 120 mA g^{-1}) with areal capacity of ~1.5 mAh cm^{-2}. The cycle life can be prolonged to ~200 cycles using the DMTMSA-only electrolyte, due to improved oxidative stability. By contrast, capacity retention is ~95.9 % over 500 cycles with an average CE of ~99.9% using 1 m NaFSI DMTMSA/THF. Similar stability can be achieved using $Na_{0.44}MnO_2$ as the cathode with an areal capacity of ~1.0 mAh cm^{-2} (Figure S21). 1 m NaFSI DMTMSA/THF enables a capacity retention of ~71.5% over 1,000 cycles with an average CE of >99.9% (Figure 3B), which outperforms 1 m NaFSI THF and DMTMSA-only electrolytes about average CE and specific capacity, respectively. Besides, more stable cycling of $NaNi_{0.33}Fe_{0.33}Mn_{0.33}O_2$ can be observed using 1 m NaFSI DMTMSA/THF, which cannot be achieved by a 1 m NaFSI THF or DMTMSA-only electrolyte, due to oxidative instability or large polarization (Figure S22).

The improvement in rate performance can also be observed for 1 m NaFSI DMTMSA/THF, which delivers a specific capacity of ~101.7 mAh g^{-1} for $Na_3V_2(PO_4)_3$ at 1.6 C (~2.4 mA cm^{-2}) (Figure 3C). In contrast, 1 m NaFSI THF and DMTMSA-only electrolytes cannot cycle at this rate due to unstable charging and large polarization (Figure S23). When the current density is increased to ~3.2 mA cm^{-2}, corresponding to 3.2 C with an areal capacity of ~1.0 mAh cm^{-2}, with a higher charging cut-off voltage of 3.9 V, stable cycling is observed using 1 m NaFSI DMTMSA/THF, with an initial specific capacity of ~108.9 mAh g^{-1} (Figure S24). The capacity retention is ~98.1% over 500 cycles with an average CE of >99.9% (Figure 3D). Further increasing the cycling rate to 5.0 C (~5.0 mA cm^{-2}) and the cut-off voltage to 4.0 V can be achieved with an initial specific capacity of ~92.9 mAh g^{-1}. 1 m NaFSI DMTMSA/THF enables capacity retention of ~70% over 1,500 cycles with an average CE of ~99.9% (Figure 3E). A pouch cell with the configuration of Na||$Na_3V_2(PO_4)_3$ was assembled to test 1 m NaFSI DMTMSA/THF. A uniaxial stack pressure of ~50 kPa was applied. After 125 cycles, capacity retention was ~95.8%, and the average CE was ~99.9% (Figures 3F and S25). Compared with the other electrolytes, e.g., ether-based and carbonate-based, and electrolyte additives using the same cathode chemistry (Table S3), 1 m NaFSI DMTMSA/THF shows excellent reversibility under practical current density (≥3.0 mA cm^{-2}) and areal capacity (≥1.0 mAh cm^{-2}).

Microscopic and spectroscopic characterizations of HSEs

Na^0 deposition morphology was studied for these different electrolytes (Figure 4). For the DMTMSA-only electrolyte, metal deposition is compact, while the particle size is small (Figures 4A and S26). The average area and perimeter are 0.43 μm^2 and 3.11 μm, respectively, as calculated from ~1,700 individual microparticles labeled using a computer vision method (Figure S27). The high particle density can be attributed to the high nucleation density, as confirmed by the large nucleation overpotential at 1.0 mA cm^{-2} (Figure S28). The DMTMSA-only electrolyte induces the formation of an inorganic-rich SEI, as shown from elemental analysis in Figure S29, which can stabilize the electrode-electrolyte interface, leading to a compact deposition morphology.

When 1 m NaFSI THF is tested, the Na^0 morphology becomes loose and the grain size is small, with an average grain area of 8.7 μm^2 (Figure 4C). In contrast, the deposition morphology is compact and the particle size is large using 1 m NaFSI DMTMSA/THF (Figure 4B) owing to the stable inorganic-rich SEI and larger ionic conductivity of the HSE. The SEI formation and interfacial evolution during the initial plating and stripping processes are further characterized for 1 m NaFSI DMTMSA/THF. The average recorded capacities are ~0.92 and ~1.85 μAh cm^{-2} when the potential reaches 0 V and the minimum voltage, respectively (Figure S30). The inorganic-rich SEI starts to form in the first cycle, while the other elements are reduced at different processes. Fluorides start to form before the voltage reaches 0 V, and the complete conversion of fluorine species to fluorides can be seen when the voltage reaches the minimum value, where the nucleation of Na^0 starts. But there are negligible nitrides forming when the voltage is >0 V, and the nitrides mainly form during the initial Na^0 nucleation process, accounting for ~70% nitrogen species. For the sulfur species, only ~10% are reduced to form sulfides after the first cycle, as shown in Figure S31. These results indicate that SEI formation is stepwise, and the reduction degrees of different elements show great variation for HSEs.

The ratio between the particle area and perimeter is defined as the structure factor, which is related to the size and shape for electrodeposited Na^0. For example, metal dendrites and small particles have a small value. They are an undesired deposition morphology for metal anodes and are responsible for low reversibility. Most microparticles show larger values as shown in the distribution of the structure factor using 1 m NaFSI DMTMSA/THF (Figure 4D), and the average structure factor value is ~4× and ~15× larger than 1 m NaFSI THF and DMTMSA-only electrolytes, respectively. The morphology results can be supported by kinetic analysis (Figure S32), where the exchange current density of 1 m NaFSI THF is more than 2 orders higher than that of 1 m NaFSI DMTMSA/THF (Figure 4E). Previous work has shown that a higher exchange current density triggers the formation of less smooth metal deposition, which is correlated with a reduction in CE.[44] Even when the current density increases to 3.0 mA cm^{-2}, the metal deposition is compact with large grain sizes using 1 m NaFSI DMTMSA/THF (Figure S33). Compared with the commercial Na with dominant {200} planes, the electrochemically deposited Na using 1 m NaFSI DMTMSA/THF shows the dominant exposure of {110}-oriented faces (Figure S34), which are the closest packed planes and the most thermodynamically stable for body-centered cubic (BCC) Na^0 crystals.[45]

The improved deposition behavior can be explained by the optimized solvation structure of HSEs. As the molar ratio between DMTMSA and THF increases, the cation-dipole interaction becomes weaker. The downshift of the ^{23}Na nuclear magnetic resonance (NMR) peak from −6.8 to −11.0 ppm can be observed (Figure 5A), reflecting the shielding effect induced by the increase of electron density near the cation and suggesting greater anion-cation association. Moreover, the peak width for different HSEs is larger than 1 m NaFSI THF and DMTMSA-only electrolytes, which is consistent with

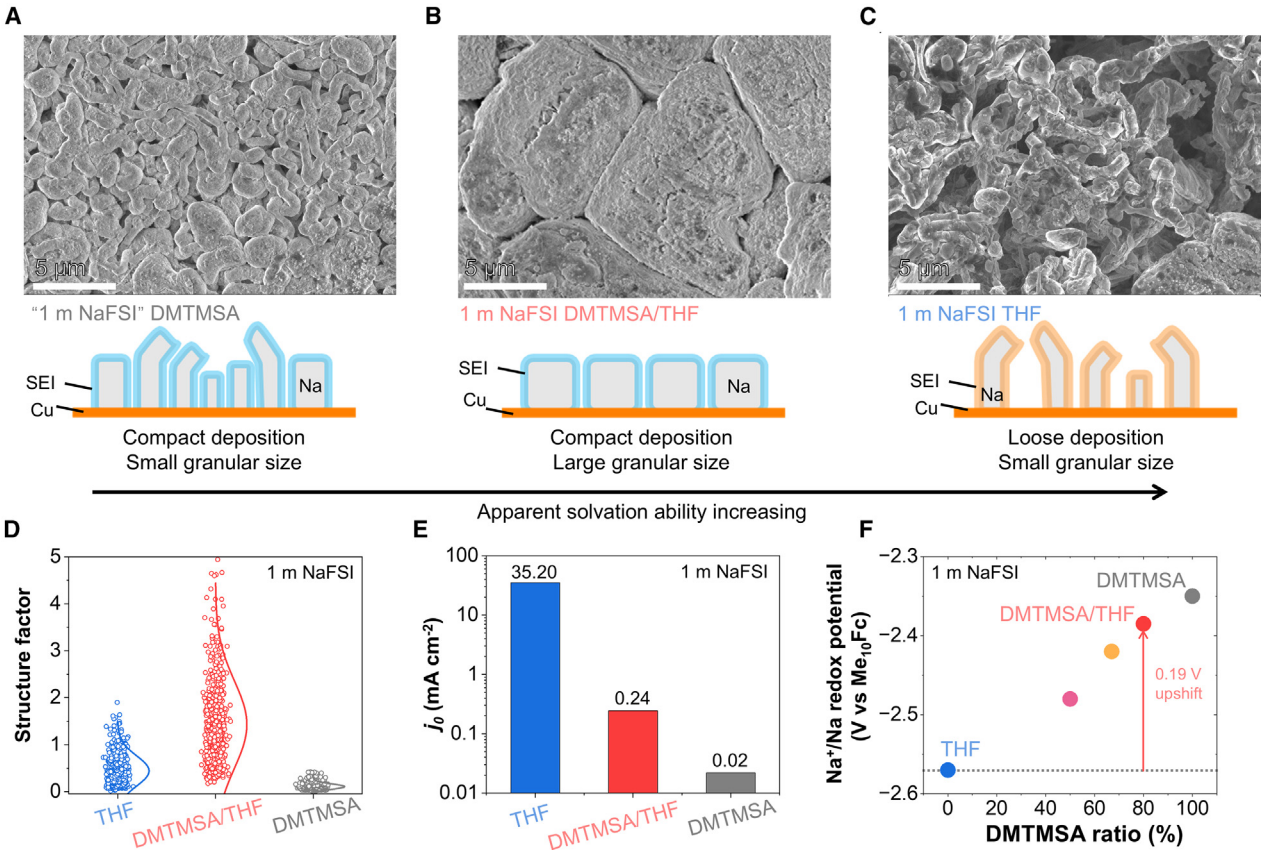

Figure 4. Microscopic and spectroscopic characterization of hybrid solvating electrolytes

(A–C) Top-view SEM images of Cu electrodes after 200 cycles using different electrolytes at the plating stage. The scheme below describes the morphology features of electrochemically deposited Na^0. The scale bars are 5 μm for all the SEM images. (A) "1 m NaFSI" in DMTMSA. (B) 1 m NaFSI in DMTMSA and THF mixture. (C) 1 m NaFSI in THF.

(D) The structure factor of electrodeposited Na metal using different electrolytes. The structure factor is defined as the ratio between the particle area and perimeter.

(E and F) The exchange current densities (E) and electrode potentials (F) of different electrolytes.

a mix of cation solvation environments within the HSEs. The interaction between solvents, induced by the dipole-dipole interaction, can also be distinguished by the proton chemical shift for both THF and DMTMSA (Figure 5B), together with the ^{19}F NMR chemical shift from DMTMSA (Figure S35). Due to the decrease of free THF and coordination with Na^+, the proton chemical shift for THF increases as the DMTMSA/THF ratio increases from 0:1 to 1:1. A slight decrease can be observed when further increasing the DMTMSA ratio, which is caused by the solvent-solvent interaction and an extra shielding effect near these protons from electron-rich O atoms in DMTMSA. Raman spectroscopy was used to show further how the combination of ion-dipole and dipole-dipole interactions in HSEs can tune the solvation structures (Figures S36 and S37). The blue-shift of Raman peaks can be seen when the molar ratio between DMTMSA and THF increases from ~1.4 to ~6.4. Meanwhile, the SSIP decreases from >60% to <10%, and AGG increases from ~14% to ~55%, while the CIP slightly varies from ~25% to ~37%, as calculated using the deconvolution results (Figure 5C). The co-existence of solvated DMTMSA and THF can also be confirmed by Fourier-transform infrared spectroscopy (FTIR) results as shown in Figure S38. The formation of CIP is essential for upshifting the thermodynamic electrode potentials,[46] which in turn weakens the reducing ability of the metal electrode and therefore improves the CE. Compared with the THF-only electrolyte, a large shift of ~0.19 V can be seen for 1 m NaFSI DMTMSA/THF (Figures 4F and S39).

To shed light on the solvation structures and determine the distribution of Na^+ solvates in the HSEs, MD simulations were employed. The radial distribution function (RDF) and coordination structures of anions and different solvents were calculated (Figures 5D–5F and S40–S42). Since the molecular structure of the DMTMSA solvent is similar to the FSI^- anion,[33] both of them participate in Na^+ solvation for the DMTMSA-only electrolyte. The coordination number (CN) of DMTMSA and FSI^- are 2.08 and 2.86, respectively, in the primary solvation sheath, therefore mainly forming the Na^+-anion clusters, which is the typical molecular feature for the weakly solvating electrolytes (WSEs). Since THF shows a stronger interaction with Na^+ than DMTMSA and FSI^-, the partial replacement of DMTMSA

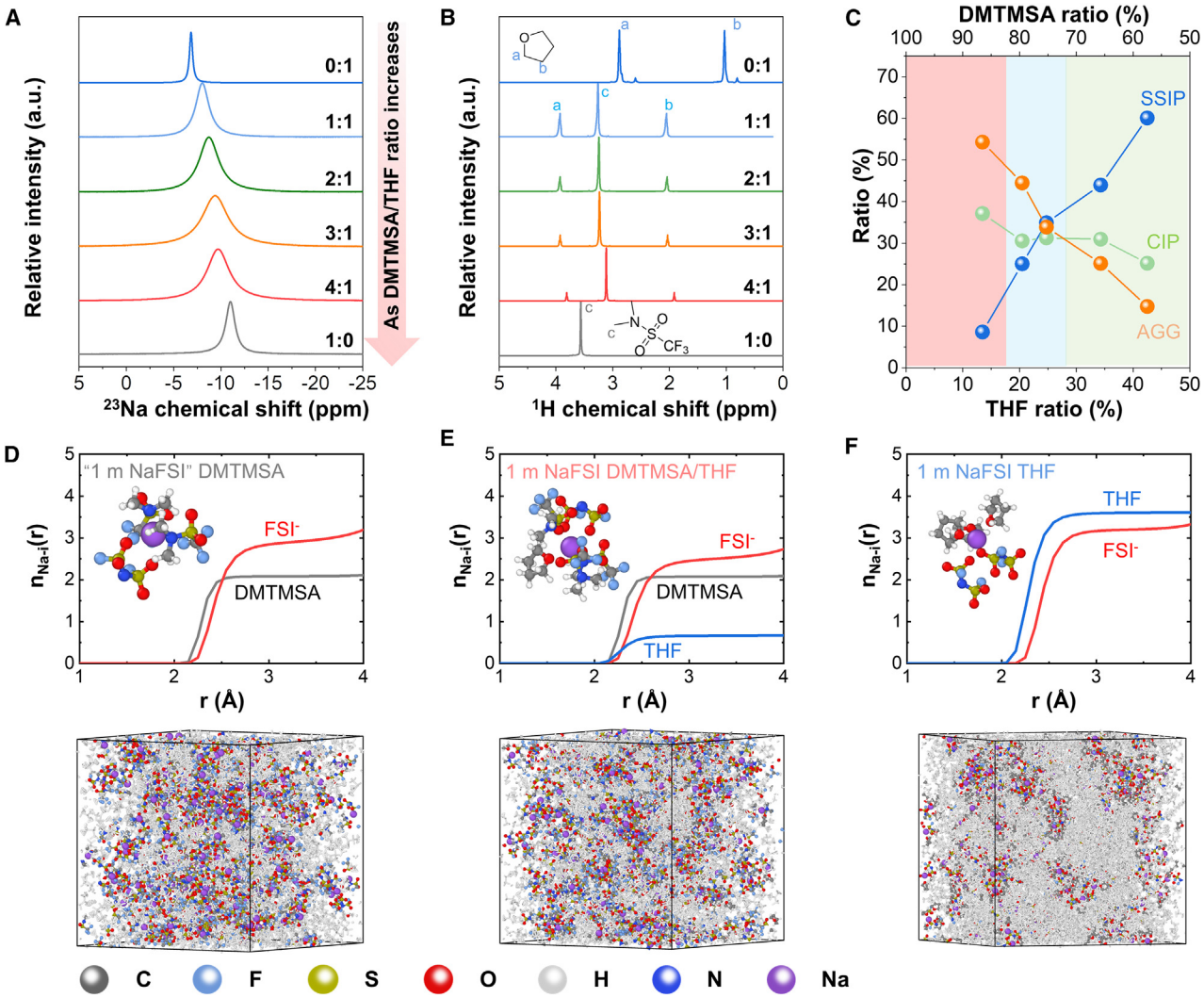

Figure 5. Properties of hybrid solvating electrolytes

(A and B) NMR spectra of (A) ^{23}Na and (B) ^{1}H for hybrid solvating electrolytes with different molar ratios between DMTMSA and THF solvents.

(C) Solvation structure analysis of hybrid solvating electrolytes with different molar ratios between DMTMSA and THF solvents.

(D–F) Coordination structures and corresponding molecular snapshots of different electrolytes. The inset shows the representative solvation structure for the electrolyte. The molar ratios between DMTMSA and THF are 1:0, 4:1, and 0:1, respectively.

and FSI^- can be achieved by controlling the THF amounts. Besides, THF is 0.1 Å closer to Na^+ than DMTMSA within the primary solvation shell, which forms the hierarchical structure and facilitates the step-by-step desolvation pathway near the anode,[47,48] contributing to the lower polarization during the cycling for HSEs. As the THF ratio increases from 0% to 20% (stage 1), the incorporation of THF within the primary solvation shell and the slight decrease of AGG and CIP can be observed, which can maintain the preferred anion decomposition at the metal anode to form stable SEI and increase the ionic conductivity simultaneously. As a result, the cycling overpotential decreased from >620 mV to ~92 mV and CE increased from ~93% to >99% (Figure 1D). For the HSE with the optimal THF ratio, the CN of anions decreases by ~14%, while THF accounts for ~13% in the primary solvation sheath. Further increasing THF ratio can reduce the cycling overpotential to ~72 mV, while keeping a relatively high CE of ~99% (stage 2). At this stage, a balanced solvation structure among SSIP (~35%), CIP (~31%), and AGG (~34%) can be seen, while (AGG + CIP) are still dominant. The slight reduction in CE can be explained by the increase in the SSIP and the decomposition of THF molecules. As the THF ratio continues to increase, the CE decreases back to ~64% and overpotential increases to ~156 mV (stage 3). This is because excessive THF can form over-solvated electrolytes, where uncoordinated solvent molecules become dominant. Due to the unstable decomposition of the THF solvent both at the cathode and anode, CE decay and polarization buildup can be seen. The spectroscopic analysis and MD simulation, along with the electrochemical performance, indicate that a balanced solvation structure can

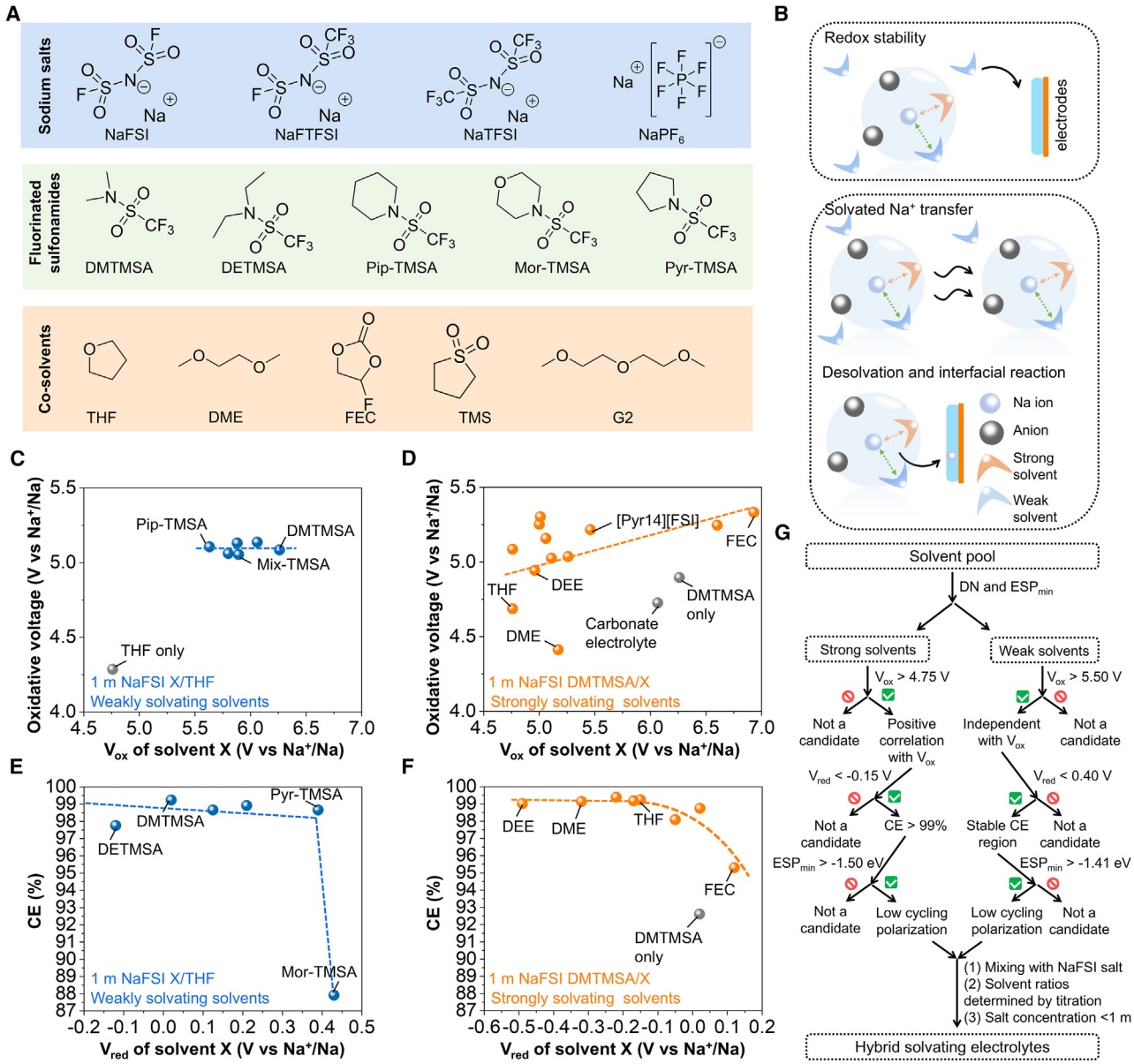

Figure 6. Generalized strategy for hybrid solvating electrolytes

(A) The representative recipes of hybrid solvating electrolytes including various sodium salts (blue region), weak solvents (green region), and strong solvents (orange region).

(B) The scheme about redox stability, solvated Na^+ movement, and desolvation related to strong and weak solvents.

(C and D) The relationship between V_{ox} of (C) weak solvents or (D) strong solvents and the oxidative voltage of the HSEs.

(E and F) The relationship between V_{red} of (E) weak solvents or (F) strong solvents and the CE of the HSEs.

(G) The general workflow to screen strong-weak solvent pairs and to design HSEs with high redox stability and low cycling polarization.

be a better choice for electrolyte design to achieve fast cycling, while still maintaining good stability against the anode and cathode.

General strategy for designing HSEs

To explore the effects of different sodium salts and solvents toward redox stability, solvated Na^+ movement and desolvation near the electrodes (Figures 6A and 6B), 50 HSEs were prepared as listed in Table S4. Their oxidative tolerance (Figure S43), cycling stability against sodium-metal anode (Figures S44–S46), and ionic conductivity (Figure S47) were tested. It was found that sodium salt can affect the oxidative stability and metal reversibility based on oxidative potential (V_{ox}) and reductive potential (V_{red}), respectively, while contributing less to the cycling overpotentials as the change of the most negative ESP (ESP_{min}) (Figure S48). As the V_{ox} of sodium salts increases, the oxidative

stability of electrolytes can be improved. But the V_{red} is negatively correlated with the average cycling CE of HSEs. Therefore, to reach a high average CE with a low cycling overpotential for HSEs, NaFSI can be a more suitable choice compared with the other sodium salts, such as sodium (fluorosulfonyl)(trifluoromethanesulfonyl)imide (NaFTFSI) and sodium bis(trifluoromethanesulfonyl)imide (NaTFSI). Therefore, NaFSI was used as the sodium salt for the subsequent HSEs design by changing different solvents.

As shown in Figure 6C, the introduction of *N*,*N*-Pip trifluoromethane sulfonamide (Pip-TMSA) boosts the oxidative voltage of HSEs by ~0.8 V, while replacing Pip-TMSA with other weak solvents involving up to ~0.6 V higher V_{ox} makes no further improvement. However, strong solvent replacement can increase the oxidative voltage to ~5.3 V when using FEC to substitute for THF (Figure 6D). A similar tendency can be found for CE and overpotential when considering the V_{red} and ESP_{min} of strong and weak solvents, respectively (Figures 6E, 6F, and S48). Even though weak solvents have a low solvation ability, they can determine the redox stabilities and cycling polarization of HSEs, while the strong solvents enable further fine-tuning of these properties. Therefore, there are different criteria for selecting solvents for HSEs depending on the solvent types, which can be pre-labeled using solvent descriptors such as DN and ESP_{min}. The ideal weak solvents should have a high V_{ox} > 5.50 V and a low V_{red} < 0.40 V, while ideal strong solvents should have a high V_{ox} > 4.75 V and a low V_{red} < –0.15 V to achieve a high CE > 99% and high oxidative voltage > 5.0 V (Figure 6G). To further reduce the cycling overpotential, the strong solvent with ESP_{min} > –1.50 eV and weak solvent with ESP_{min} > –1.41 eV are recommended. For the solvent ratio between strong and weak solvents, it is determined by the titration method as discussed in the methods section. As a result, the final salt concentration of HSEs is 0.8–1.0 mol kg^{-1}, and the strong solvents account for 10%~30%.

Besides, the combination of various weak and strong solvents can be used to further optimize the electrochemical performance for HSEs. For example, the HSE using ionic liquid N-methyl-N-butyl pyrrolidinium bis(fluorosulfonyl)imide ([Pyr14][FSI]), DMTMSA, and THF can increase the oxidative stability to ~4.6 V (Figure S43E), which is higher than 1 m NaFSI DMTMSA/THF (~4.5 V), and the ionic conductivity reaches ~2.52 mS cm^{-1} at room temperature (Figure S47), which outperforms 1 m NaFSI DMTMSA/THF by ~75%.

1 mol L^{-1} $NaPF_6$ diglyme electrolyte, which has been reported with superior electrochemical performance, including high CE in half cells and self-modulated continuous deposits,[49] can also be modified to prepare HSEs. By replacing 50 vol % of diglyme with DMTMSA, a 1 mol L^{-1} $NaPF_6$ DMTMSA/diglyme electrolyte can be prepared, which shows a ~0.44 V higher onset oxidative potentials with a similar ionic conductivity, compared with a diglyme-only electrolyte (Figure S49). Anode-free SMBs without excess sodium metal can improve energy density by more than 50% and reduce the production costs from handling sodium-metal anodes. Their practical application requires fast activation, high metal reversibility, and cathode compatibility. Therefore, future work to design HSEs with a higher average CE of >99.8% and oxidative stability to pair with high-voltage cathodes can be important for anode-free SMBs to achieve a high-capacity retention of >80% after 100 cycles.

The design principles of HSEs can also be used for other rechargeable ion batteries[50] and metal batteries, such as lithium-metal batteries. By mixing THF and DMTMSA with the molar ratio of 1.0:3.5, there is a higher Aurbach CE of ~99.23% for 1 mol kg^{-1} LiFSI DMTMSA/THF using the current density of 3.0 mA cm^{-2}, compared to 1 mol kg^{-1} LiFSI DMTMSA (~98.93%) and 1 mol kg^{-1} LiFSI THF (~97.12%). The cycling performance can be further improved by tuning the salt concentrations and solvent ratios. The average Aurbach CE can reach ~99.36% after the formation of stable SEI atop the Cu current collector (Figure S50).

Conclusions

To conclude, we showed that HSEs can achieve the fastest activation, maintain low overpotentials and high reversibility even when cycled with a practical current density (~3.0 mA cm^{-2}), compared with the advanced electrolytes proposed in recent work for SMBs[1,7,8,13,25,31,51–54] (Table S2). This performance cannot be realized by individual solvents, owing to the absence of favored solvation structures contributing from the fine-tuning between strongly and weakly solvating solvents. The solvent selection principles for both strong and weak solvents, and their distinct effects on redox stabilities and cycling polarization were uncovered based on 50 HSEs. As high-entropy electrolytes[55] could boost the electrochemical performance, the development of HSEs with multiple salts and co-solvents can be a promising direction. Besides, the design principle of HSEs can be applied to the other rechargeable batteries, flow cells, and electrochemical cells using liquid electrolytes.

METHODS

Materials

NaFSI (99.9% purity), NaTFSI (99.5% purity), and [Pyr14][FSI] (99.9% purity) were purchased from Solvionic. NaFTFSI (98.0% purity) was purchased from Provisco CS. $NaPF_6$ (98.0% purity), THF (99.9% purity), diethylene glycol dimethyl ether (diglyme, 99.5% purity), 1,2-dimethoxyethane (DME, 99.5% purity), 1,2-diethoxyethane (DEE, 98.0% purity), triethylene glycol dimethyl ether (TGDE, 99.0% purity), and tetraethylene glycol dimethyl ether (TEGDME, 99.0% purity) were purchased from Millipore Sigma. FEC(98.0% purity) and 2,2,2-trifluoroethyl methanesulfonate (TM, 98.0% purity) were purchased from TCI. DMTMSA and its derivatives, including other trifluoromethanesulfonamide solvents derived from water-miscible secondary amines: diethylamine, pyrrolidine, piperidine, and morpholine, corresponding to DETMSA, Pyr-TMSA, Pip-TMSA and Mor-TMSA, were synthesized based on our previous work.[56] Sodium-metal chips (15.6 mm diameter and 0.5 mm thickness) were purchased from Xiamen AOT Electronics Technology. Copper foil (annealed, uncoated, 99.8% purity) was purchased from Fisher Scientific. The separator used was quartz fiber filters (QR100) from Sterlitech. To characterize the electrode surface after cycling, one-layer Celgard 2320 was added between QR100 separator and the electrode. NVP cathode powder was purchased from MSE supplies. $NaNi_{1/3}Fe_{1/3}Mn_{1/3}O_2$ cathode powder was purchased

from MTI Corporation. Sodium manganese oxide cathode ($Na_{0.44}MnO_2$ [NMO], 8.28 mg cm^{-2}) was purchased from NEI Corporation.

For the solvent degassing procedure, all fluorinated sulfonamide solvents were distilled under vacuum before use. Activated 5 Å molecular sieves were added to an oven-dried Schlenk storage flask/tube, and the flask was purged with dry nitrogen as it cooled to room temperature. After cooling to room temperature, the vacuum-distilled fluorinated sulfonamide solvent was added to the flask (no more than half-filled). The stopcock was closed, and then the flask was cooled to 0°C with an ice bath. Vacuum was applied to the sidearm of the flask, and the stopcock was opened to begin vacuum-degassing the contents of the flask. The flask was occasionally agitated over 30 min, during which time the initial vigorous bubbling slowed. After 30 min, the stopcock was closed while the flask was still evacuated, and the flask was brought into an argon-filled glovebox for electrochemical studies. Any suspended molecular sieve particles were either allowed to settle overnight or were removed by syringe filtering.

Characterization

The electrodes after electrochemical cycling were characterized through SEM using Zeiss Merlin High-resolution SEM at 3 kV with a working distance of 6 mm. X-ray photoelectron spectroscopy (XPS) data were collected with a PHI Quantera SXM scanning X-ray microprobe with a base pressure of 5×10^{-9} torr. Survey spectra were recorded using 0.5-eV step sizes with a pass energy of 140 eV. Elemental spectra were recorded using 0.1-eV step sizes with a pass energy of 26 eV. All the XPS spectra were corrected using the C 1s peaks (284.8 eV) as reference. To avoid sample oxidation, the air-tight transfer container was used to directly transfer the electrodes from the glovebox to the SEM or XPS transfer chamber. XRD measurements were done by with filtered Cu Kα radiation (λ = 1.5406 Å). NMR was used to characterize the electrolytes using a Neo402 three-channel Bruker Avance Neo spectrometer operating at 400.17 MHz. The quick pressure valve (QPV) NMR sample tubes (Wilmad-LabGlass SP Scienceware, 5 mm OD) were used to prevent air exposure and evaporation of the electrolytes. Deuterated chloroform ($CDCl_3$) was used as the external reference for the test. Renishaw Invia Reflex Micro Raman with a laser wavelength of 532 nm was used to characterize the liquid electrolytes within the liquid cells to prevent air exposure. FTIR measurements were taken on a Tensor II (Bruker) FTIR with deuterated triglycine sulfate (DTGS) detector inside an argon-filled glovebox. The scan velocity was 1.6 kHz and the spectral resolution was 4 cm^{-1}. Absorbance spectra were collected using a hemispherical 20 mm diameter Ge crystal together with attenuated total reflection accessory (Pike Vee-Max II, Pike Technologies) at an incidence angle of 50°. 10–25 μL of electrolyte was dropped onto the crystal and 32 scans were superimposed for each measurement. All absorbance spectra were collected in the form of $\log(I_0/I_1)$, where I_0 is the background spectrum and I_1 is the sample spectrum.

Electrochemical tests

The electrolytes used in this work were prepared inside the glovebox (O_2 content < 0.2 ppm, H_2O content < 0.01 ppm) before use, and the detailed molar ratios among different salts and solvents are shown in Table S4. To demonstrate the generality of HSEs, electrolytes 13–50 (except 20, 37, 44 and 47) were prepared using the dropwise titration method. Specifically, ~1.0 mmol sodium salt was first mixed with ~1.0 g weak solvent or solvent mixture to form the suspension electrolyte. Then, the other strong solvents were added dropwise until the electrolyte became clear. Therefore, the final concentration of the electrolyte can be controlled to be around 0.8–1.0 mol kg^{-1}, which was close to the commercial sodium electrolytes and was within the suitable range to reach good electrochemical properties. The final solvent ratio was determined based on the added strong solvent(s) and the weak solvent(s) as mentioned above. Since 1 mol kg^{-1} NaFSI DMTMSA forms a suspension electrolyte, both the supernatant and whole suspension are used to evaluate its electrochemical performance. The voltage curve can be seen in Figure S51, where supernatant outperforms the whole suspension. Therefore, the supernatant is used as "1 m NaFSI" in DMTMSA for this work.

To test the electrochemical performance against the Na-metal anode of different electrolytes, a half-cell with the configuration of Na||Cu was used. The coin cells were charged and discharged on a battery working station (LANHE corporation, China) in air at 25°C. For the normal cycle protocol, two precycles with a current density of 0.4 mA cm^{-2} and an areal capacity of 2.0 mAh cm^{-2} were used. The cycling current density was 1.0 mA cm^{-2} with an areal capacity of 1.0 mAh cm^{-2} unless otherwise specified.

For the modified Aurbach method, initially 4.0 mAh cm^{-2} of Na metal was deposited on the Cu electrode with the current density of 1.0 mA cm^{-2} and stripped until the voltage reached 1.0 V. After the formation cycle, 4.0 mAh cm^{-2} of Na metal was deposited again, to act as a Na reservoir. Then, Na was repeatedly stripped and plated with the areal capacity of 1.0 mAh cm^{-2} for nine cycles. The remaining Na on Cu was then stripped until the voltage reached 1.0 V, and the average CE was calculated by dividing the total stripping capacity by the total plating capacity after the formation cycle. For the optimized cycling protocol to measure CE as shown in Figure 2B, before testing the average CE using the modified Aurbach method, a precycle using Aurbach cycle, which included the same protocol as the modified Aurbach method above was applied to form the stable passivation layer atop the Cu collector.

For NVP cathode preparation, the NVP powder was mixed with PVDF and acetylene black at a mass ratio of 8:1:1 in NMP. The slurry was spread on carbon-coated Al foil (active mass loading of ~12 mg cm^{-2}) and dried in the oven overnight. The 2032-type coin cell was assembled using Na-metal foil as the anode and NVP as the cathode inside an Ar-filled glovebox. The separator used here was QR100. The test range of NVP cathode is 2.2 to 3.8 V versus Na^+/Na unless otherwise specified. After the initial two formation cycles at 0.05 cycling rate (C, 1 C ≡ 120 mAh g^{-1}), the battery was tested at 0.2 C. The constant current mode was used for the test. For the fast-cycling test, the cell was charged until 3.9 and 4.0 V at 3.2 and 5.0 C, respectively. For the single-layer pouch cell, the NVP cathode (~8 mg cm^{-2}) was paired with thin Na-metal foil and tested with a uniaxial pressure of ~50 kPa. Both the length and width were 10 mm for the cathode and 12 mm for the anode. The ratio between electrolyte and capacity (E/C) was ~20 g Ah^{-1}. After the initial two formation cycles at

0.05 cycling rate (C, 1 C ≡ 120 mAh g^{-1}), the battery was tested at 0.25 C. The constant current mode was used for the test. For the NMO cathode (~8.28 mg cm^{-2}), The test range of NMO cathode is 2.0 to 3.8 V versus Na^+/Na. After the initial two formation cycles at 0.05 cycling rate (C, 1 C ≡ 120 mAh g^{-1}), the battery was tested at 0.3 C. The constant current mode was used for the test.

For the EIS tests, symmetric Al||Al cell was used with QP100 as the separator. The measurements were conducted by applying an alternating voltage of 5 mV in the frequency range from 0.1 Hz to 1 MHz. At different temperatures, the cell was stabilized in the oven for 30 min before the measurement. The ionic conductivity and de-solvation activation energy can be calculated as described in Note S2.

For oxidative tolerance tests, Na||stainless steel cell was used. The voltage was scanned from 2.5 to 6.0 V versus Na^+/Na with a scanning rate of 1 mV s^{-1}. The onset oxidation potential was recorded when the current density reached 0.01 mA cm^{-2}.

For electrode potentials, cyclic voltammetry was conducted using a VMP3 potentiostat (BioLogic) to evaluate the Na/Na^+ redox potential (E_{Na}) in a three-electrode cell consisting of a glassy carbon working electrode and Na-metal counter and reference electrodes with various electrolytes containing 2 mM decamethylferrocene ($Me_{10}Fc$, Alfa Aesar). The redox potential of $Me_{10}Fc/Me_{10}Fc^+$ was measured with reference to Na/Na^+, and E_{Na} of various electrolytes was quantified assuming that the potential of $Me_{10}Fc/Me_{10}Fc^+$ is constant according to IUPAC recommendations.[57] The scanning rate was 10 mV s^{-1}.

For the kinetic analysis, a method similar to that of Hobolt et al.[58] was adopted. Specifically, CV in two-electrode coin cells was measured with a Biologic VMP-300 potentiostat at a scan rate of 1 mV s^{-1}. Pristine Cu was the working electrode, while Na metal was the counter electrode. The CV potential window was from −0.2 to 1 V versus Na/Na^+. To extract the redox kinetics, we focused on the 4th voltammetry cycle to ensure proper SEI formation and interface stabilization. The CV data underwent several processing steps: initially, impedance measurements for each cell were used to compensate for the *iR* drop before cycling. The cell potential was then adjusted so that the potential at zero current was zero. For further analysis, data from the low-overpotential region, where the current response is linear with overpotential, was utilized to estimate the exchange current density by fitting the Butler-Volmer kinetic model to our experimental data.[59]

Computer vision method

The extensively image-trained Segment Anything model[60] is adopted to extract features of metal microparticles distribution. The model can conduct a blanket search across the sample by automatically inputting grid point prompts into SEM images. To ensure coverage of the entire sample under zero-shot conditions, the thresholds for intersection over union (IoU) and stability score were incrementally adjusted. Additionally, test-time augmentation (TTA) techniques, enhancing the accuracy and precision of segmented images through horizontal and vertical flipping, were utilized. Subsequently, geometric parameters, such as the perimeter and area of pixels segmented from each metal microparticle, were utilized. All processes were performed on an RTX 4090 to ensure computational efficiency and speed.

Molecular descriptors simulation

The provided ESP result was derived from density functional theory (DFT) calculations. These calculations were performed using the PSI4[61] framework with B3LYP and 6–311G(d,p) basis sets for structure optimization and simulation. We extracted the most positive and the most negative potential as features. The solvent-accessible surface area was calculated using the FreeSASA[62] framework, employing the Lee and Richards algorithm.

For estimating the DN, we utilized the pre-trained molecular representation framework MolCLR[63] for fine-tuning. The fine-tuning data consisted of 223 entries from the Gutmann acceptor and DN dataset,[64] and we employed gradient boosting regressor for classification. This process used 5-fold validation, resulting in a mean absolute error of 0.38 kcal/mol.

MD simulation

MD simulations were performed to elucidate the solvation structure of Na^+ depending on the electrolyte component and composition, using the large-scale atomistic/molecular massively parallel simulator (LAMMPS).[65] We constructed four different model systems corresponding to 1 m NaFSI DMTMSA, 1 m NaFSI DMTMSA/THF, 1 m NaFSI DMTMSA/THF42, and 1 m NaFSI THF electrolytes. The model systems contained ratios of DMTMSA: NaFSI: THF as 113:20:0, 113:20:28, 113:20:84, and 0:20:278, respectively. The interatomic potential of optimized potentials for liquid simulation all atom (OPLS-aa)[66] used in the simulations was generated by the LigParGen server.[67] The NPT ensemble with a timestep of 1 fs was applied to obtain equilibrium structures lasting more than 5 ns. The RDF was obtained by averaging snapshots taken every 1 ps during the last 4 ns. The edge lengths of model systems were 5.8, 6.1, 6.6, and 6.9 nm, respectively for 1 m NaFSI DMTMSA, 1 m NaFSI DMTMSA/THF, 1 m NaFSI DMTMSA/THF42, and 1 m NaFSI THF electrolytes.

RESOURCE AVAILABILITY

Lead contact

Further information and requests for resources and materials should be directed to and will be fulfilled by the lead contact, Ju Li (liju@mit.edu).

Materials availability

All unique reagents generated in this study will be made available upon reasonable request.

Data and code availability

The datasets supporting the findings of the study are available in the paper and its supplemental information. The code for solvent descriptors calculation and computer vision method can be accessed at https://zenodo.org/records/14454309.

ACKNOWLEDGMENTS

W.C. and J.L. acknowledge the support by Honda R&D. D.W. acknowledges the financial support of the Assistant Secretary for Energy Efficiency and Renewable Energy, Vehicle Technologies Office, under the Advanced Battery Materials Research (BMR) Program, of the US Department of Energy under contract no. DE-AC02-06CH11357, subcontract no. 9F-60231. J.K.P. acknowledges the support from the National Science Foundation (NSF) Graduate Research Fellowship under grant no. 2141064. C.O.P.-R. acknowledges

the support from MIT Energy Initiative. The characterization equipment used in this project is partly from MIT.nano Characterization Facilities at Massachusetts Institute of Technology.

AUTHOR CONTRIBUTIONS

W.C. conceived the HSEs for sodium-metal batteries under the direction of J.L. W.C. and J.-S.P. prepared the electrolytes and assembled the coin cells. The pouch cell was assembled by W.C. with the help of G.Z. C.K. performed the molecular dynamics simulation. C.O.P.-R. conducted the kinetic and viscosity measurements, Raman tests, some CE, conductivity, and activation energy measurements. C.-W.H. conducted the computer vision analysis and molecular descriptor calculation. L.J.K. synthesized all the fluorinated sulfonates. D.W. performed the FTIR. J.K.P. and C.O.P.-R. measured the electrode redox potentials and kinetics. J.K.P. characterized electrolyte polymerization. T.D. and S.Y.K. helped to calculate the activation energy. Z.R. and Z.Z. prepared the mold for coin cell preparation. S.Y.K. helped with XRD characterization. Y.G. helped with the XPS analysis. H.L. helped with pouch cells preparation. All aspects of the research were overseen by J.L., J.A.J. and Y.S.-H. All authors discussed the results and commented on the manuscript.

DECLARATION OF INTERESTS

Massachusetts Institute of Technology owns intellectual property on the hybrid solvating electrolytes for sodium-metal batteries disclosed here. That intellectual property is currently licensed.

SUPPLEMENTAL INFORMATION

Supplemental information can be found online at https://doi.org/10.1016/j.joule.2024.101811.

Received: September 1, 2024
Revised: November 6, 2024
Accepted: December 19, 2024
Published: January 24, 2025

REFERENCES

1. Cao, R., Mishra, K., Li, X., Qian, J., Engelhard, M.H., Bowden, M.E., Han, K.S., Mueller, K.T., Henderson, W.A., and Zhang, J.-G. (2016). Enabling room temperature sodium metal batteries. Nano Energy *30*, 825–830. https://doi.org/10.1016/j.nanoen.2016.09.013.
2. Li, Y., Zhou, Q., Weng, S., Ding, F., Qi, X., Lu, J., Li, Y., Zhang, X., Rong, X., Lu, Y., et al. (2022). Interfacial engineering to achieve an energy density of over 200 Wh kg^{-1} in sodium batteries. Nat. Energy *7*, 511–519. https://doi.org/10.1038/s41560-022-01033-6.
3. Tian, Z., Zou, Y., Liu, G., Wang, Y., Yin, J., Ming, J., and Alshareef, H.N. (2022). Electrolyte solvation structure design for sodium ion batteries. Adv. Sci. *9*, e2201207. https://doi.org/10.1002/advs.202201207.
4. Zhu, Y.G., Leverick, G., Accogli, A., Gordiz, K., Zhang, Y., and Shao-Horn, Y. (2022). A high rate and high-efficiency molten-salt sodium–oxygen battery. Energy Environ. Sci. *15*, 4636–4646. https://doi.org/10.1039/D2EE01774A.
5. Sayahpour, B., Li, W., Bai, S., Lu, B., Han, B., Chen, Y.-T., Deysher, G., Parab, S., Ridley, P., Raghavendran, G., et al. (2024). Quantitative analysis of sodium metal deposition and interphase in Na metal batteries. Energy Environ. Sci. *17*, 1216–1228. https://doi.org/10.1039/D3EE03141A.
6. Schmuch, R., Wagner, R., Hörpel, G., Placke, T., and Winter, M. (2018). Performance and cost of materials for lithium-based rechargeable automotive batteries. Nat. Energy *3*, 267–278. https://doi.org/10.1038/s41560-018-0107-2.
7. Seh, Z.W., Sun, J., Sun, Y., and Cui, Y. (2015). A highly reversible room-temperature sodium metal anode. ACS Cent. Sci. *1*, 449–455. https://doi.org/10.1021/acscentsci.5b00328.
8. Deng, Y., Zheng, J., Zhao, Q., Yin, J., Biswal, P., Hibi, Y., Jin, S., and Archer, L.A. (2022). Highly reversible sodium metal battery anodes via alloying heterointerfaces. Small *18*, e2203409. https://doi.org/10.1002/smll.202203409.
9. Ji, Y., Qiu, J., Zhao, W., Liu, T., Dong, Z., Yang, K., Zheng, G., Qian, G., Yang, M., Chen, Q., et al. (2023). In situ probing the origin of interfacial instability of Na metal anode. Chem *9*, 2943–2955. https://doi.org/10.1016/j.chempr.2023.06.002.
10. Dai, T., Wu, S., Lu, Y., Yang, Y., Liu, Y., Chang, C., Rong, X., Xiao, R., Zhao, J., Liu, Y., et al. (2023). Inorganic glass electrolytes with polymer-like viscoelasticity. Nat. Energy *8*, 1221–1228. https://doi.org/10.1038/s41560-023-01356-y.
11. Liu, Q., Zhang, L., Sun, H., Geng, L., Li, Y., Tang, Y., Jia, P., Wang, Z., Dai, Q., Shen, T., et al. (2020). In situ observation of sodium dendrite growth and concurrent mechanical property measurements using an environmental transmission electron microscopy–atomic force microscopy (ETEM-AFM) platform. ACS Energy Lett. *5*, 2546–2559. https://doi.org/10.1021/acsenergylett.0c01214.
12. Niu, Y., Hu, Z., Zhang, B., Xiao, D., Mao, H., Zhou, L., Ding, F., Liu, Y., Yang, Y., Xu, J., et al. (2023). Earth-abundant Na-Mg-Fe-Mn-O cathode with reversible hybrid anionic and cationic redox. Adv. Energy Mater. *13*, 2300746. https://doi.org/10.1002/aenm.202300746.
13. He, J., Bhargav, A., Su, L., Lamb, J., Okasinski, J., Shin, W., and Manthiram, A. (2024). Tuning the solvation structure with salts for stable sodium-metal batteries. Nat. Energy *9*, 446–456. https://doi.org/10.1038/s41560-024-01469-y.
14. Liu, X., Zhao, J., Dong, H., Zhang, L., Zhang, H., Gao, Y., Zhou, X., Zhang, L., Li, L., Liu, Y., et al. (2024). Sodium difluoro(oxalato)borate additive-induced robust SEI and CEI layers enable dendrite-free and long-cycling sodium-ion batteries. Adv. Funct. Mater. *34*, 2402310. https://doi.org/10.1002/adfm.202402310.
15. Bao, C., Wang, B., Liu, P., Wu, H., Zhou, Y., Wang, D., Liu, H., and Dou, S. (2020). Solid electrolyte interphases on sodium metal anodes. Adv. Funct. Mater. *30*, 2004891. https://doi.org/10.1002/adfm.202004891.
16. Chen, W., Salvatierra, R.V., Li, J.T., Luong, D.X., Beckham, J.L., Li, V.D., La, N., Xu, J., and Tour, J.M. (2022). Brushed metals for rechargeable metal batteries. Adv. Mater. *34*, e2202668. https://doi.org/10.1002/adma.202202668.
17. Jiang, K., Xu, S., Guo, S., Zhang, X., Zhang, X., Qiao, Y., Fang, T., Wang, P., He, P., and Zhou, H. (2018). A phase-transition-free cathode for sodium-ion batteries with ultralong cycle life. Nano Energy *52*, 88–94. https://doi.org/10.1016/j.nanoen.2018.07.042.
18. Wang, P.-F., You, Y., Yin, Y.-X., and Guo, Y.-G. (2018). Layered oxide cathodes for sodium-ion batteries: phase transition, air stability, and performance. Adv. Energy Mater. *8*, 1701912. https://doi.org/10.1002/aenm.201701912.
19. Han, B., Li, X., Wang, Q., Zou, Y., Xu, G., Cheng, Y., Zhang, Z., Zhao, Y., Deng, Y., Li, J., et al. (2022). Cryo-electron tomography of highly deformable and adherent solid-electrolyte interphase exoskeleton in Li-metal batteries with ether-based electrolyte. Adv. Mater. *34*, e2108252. https://doi.org/10.1002/adma.202108252.
20. Hu, J., Wang, H., Yuan, F., Wang, J., Zhang, H., Zhao, R., Wu, Y., Kang, F., and Zhai, D. (2024). Deciphering the formation and accumulation of solid-electrolyte interphases in Na and K carbonate-based batteries. Nano Lett. *24*, 1673–1678. https://doi.org/10.1021/acs.nanolett.3c04401.
21. Gao, L., Chen, J., Chen, Q., and Kong, X. (2022). The chemical evolution of solid electrolyte interface in sodium metal batteries. Sci. Adv. *8*, eabm4606. https://doi.org/10.1126/sciadv.abm4606.
22. Li, X., Zhao, L., Li, P., Zhang, Q., and Wang, M.-S. (2017). In-situ electron microscopy observation of electrochemical sodium plating and stripping dynamics on carbon nanofiber current collectors. Nano Energy *42*, 122–128. https://doi.org/10.1016/j.nanoen.2017.10.050.

23. Zeng, Z., Barai, P., Lee, S.-Y., Yang, J., Zhang, X., Zheng, W., Liu, Y.-S., Bustillo, K.C., Ercius, P., Guo, J., et al. (2020). Electrode roughness dependent electrodeposition of sodium at the nanoscale. Nano Energy *72*, 104721. https://doi.org/10.1016/j.nanoen.2020.104721.

24. Yang, H., He, F., Li, M., Huang, F., Chen, Z., Shi, P., Liu, F., Jiang, Y., He, L., Gu, M., et al. (2021). Design principles of sodium/potassium protection layer for high-power high-energy sodium/potassium-metal batteries in carbonate electrolytes: a case study of Na_2Te/K_2Te. Adv. Mater. *33*, 2106353. https://doi.org/10.1002/adma.202106353.

25. Zhuang, R., Zhang, X., Qu, C., Xu, X., Yang, J., Ye, Q., Liu, Z., Kaskel, S., Xu, F., and Wang, H. (2023). Fluorinated porous frameworks enable robust anode-less sodium metal batteries. Sci. Adv. *9*, eadh8060. https://doi.org/10.1126/sciadv.adh8060.

26. Yuan, X., Liu, B., Mecklenburg, M., and Li, Y. (2023). Ultrafast deposition of faceted lithium polyhedra by outpacing SEI formation. Nature *620*, 86–91. https://doi.org/10.1038/s41586-023-06235-w.

27. Chen, X., Li, Z., Zhao, H., Li, J., Li, W., Han, C., Zhang, Y., Lu, L., Li, J., and Qiu, X. (2024). Dominant solvent-separated ion pairs in electrolytes enable superhigh conductivity for fast-charging and low-temperature lithium ion batteries. ACS Nano *18*, 8350–8359. https://doi.org/10.1021/acsnano.3c12877.

28. Zhong, S., Yu, Y., Yang, Y., Yao, Y., Wang, L., He, S., Yang, Y., Liu, L., Sun, W., Feng, Y., et al. (2023). Molecular engineering on solvation structure of carbonate electrolyte toward durable sodium metal battery at -40 °C. Angew. Chem. Int. Ed. *62*, e202301169. https://doi.org/10.1002/anie.202301169.

29. Fang, H., Huang, Y., Hu, W., Song, Z., Wei, X., Geng, J., Jiang, Z., Qu, H., Chen, J., and Li, F. (2024). Regulating ion-dipole interactions in weakly solvating electrolyte towards ultra-low temperature sodium-ion batteries. Angew. Chem. Int. Ed. Engl. *63*, e202400539. https://doi.org/10.1002/anie.202400539.

30. Wang, S., Zhang, X.-G., Gu, Y., Tang, S., and Fu, Y. (2024). An ultrastable low-temperature Na metal battery enabled by synergy between weakly solvating solvents. J. Am. Chem. Soc. *146*, 3854–3860. https://doi.org/10.1021/jacs.3c11134.

31. Zheng, J., Chen, S., Zhao, W., Song, J., Engelhard, M.H., and Zhang, J.-G. (2018). Extremely stable sodium metal batteries enabled by localized high-concentration electrolytes. ACS Energy Lett. *3*, 315–321. https://doi.org/10.1021/acsenergylett.7b01213.

32. Lin, Y., Yu, Z., Yu, W., Liao, S.-L., Zhang, E., Guo, X., Huang, Z., Chen, Y., Qin, J., Cui, Y., et al. (2024). Impact of the fluorination degree of ether-based electrolyte solvents on Li-metal battery performance. J. Mater. Chem. A *12*, 2986–2993. https://doi.org/10.1039/D3TA05535C.

33. Xue, W., Huang, M., Li, Y., Zhu, Y.G., Gao, R., Xiao, X., Zhang, W., Li, S., Xu, G., Yu, Y., et al. (2021). Ultra-high-voltage Ni-rich layered cathodes in practical Li metal batteries enabled by a sulfonamide-based electrolyte. Nat. Energy *6*, 495–505. https://doi.org/10.1038/s41560-021-00792-y.

34. Yu, Z., Wang, H., Kong, X., Huang, W., Tsao, Y., Mackanic, D.G., Wang, K., Wang, X., Huang, W., Choudhury, S., et al. (2020). Molecular design for electrolyte solvents enabling energy-dense and long-cycling lithium metal batteries. Nat. Energy *5*, 526–533. https://doi.org/10.1038/s41560-020-0634-5.

35. Li, A.-M., Borodin, O., Pollard, T.P., Zhang, W., Zhang, N., Tan, S., Chen, F., Jayawardana, C., Lucht, B.L., Hu, E., et al. (2024). Methylation enables the use of fluorine-free ether electrolytes in high-voltage lithium metal batteries. Nat. Chem. *16*, 922–929. https://doi.org/10.1038/s41557-024-01497-x.

36. Mao, M., Gong, L., Wang, X., Wang, Q., Zhang, G., Wang, H., Xie, W., Suo, L., and Wang, C. (2024). Electrolyte design combining fluoro- with cyano-substitution solvents for anode-free Li metal batteries. Proc. Natl. Acad. Sci. USA *121*, e2316212121. https://doi.org/10.1073/pnas.2316212121.

37. Li, G.-X., Koverga, V., Nguyen, A., Kou, R., Ncube, M., Jiang, H., Wang, K., Liao, M., Guo, H., Chen, J., et al. (2024). Enhancing lithium-metal battery longevity through minimized coordinating diluent. Nat. Energy *9*, 817–827. https://doi.org/10.1038/s41560-024-01519-5.

38. Zhang, J., Zhang, H., Weng, S., Li, R., Lu, D., Deng, T., Zhang, S., Lv, L., Qi, J., Xiao, X., et al. (2023). Multifunctional solvent molecule design enables high-voltage Li-ion batteries. Nat. Commun. *14*, 2211. https://doi.org/10.1038/s41467-023-37999-4.

39. Chen, J., Zhang, H., Fang, M., Ke, C., Liu, S., and Wang, J. (2023). Design of localized high-concentration electrolytes via donor number. ACS Energy Lett. *8*, 1723–1734. https://doi.org/10.1021/acsenergylett.3c00004.

40. Wu, Y., Hu, Q., Liang, H., Wang, A., Xu, H., Wang, L., and He, X. (2023). Electrostatic potential as solvent descriptor to enable rational electrolyte design for lithium batteries. Adv. Energy Mater. *13*, 2300259. https://doi.org/10.1002/aenm.202300259.

41. Zhao, Y., Zhou, T., Jeurgens, L.P.H., Kong, X., Choi, J.W., and Coskun, A. (2023). Electrolyte engineering for highly inorganic solid electrolyte interphase in high-performance lithium metal batteries. Chem *9*, 682–697. https://doi.org/10.1016/j.chempr.2022.12.005.

42. Li, J., Sui, S., Zhou, X., Lei, K., Yang, Q., Chu, S., Li, L., Zhao, Y., Gu, M., Chou, S., et al. (2024). Weakly coordinating diluent modulated solvation chemistry for high-performance sodium metal batteries. Angew. Chem. Int. Ed. *63*, e202400406. https://doi.org/10.1002/anie.202400406.

43. Jin, Y., Le, P.M.L., Gao, P., Xu, Y., Xiao, B., Engelhard, M.H., Cao, X., Vo, T.D., Hu, J., Zhong, L., et al. (2022). Low-solvation electrolytes for high-voltage sodium-ion batteries. Nat. Energy *7*, 718–725. https://doi.org/10.1038/s41560-022-01055-0.

44. Hobold, G.M., Lopez, J., Guo, R., Minafra, N., Banerjee, A., Shirley Meng, Y.S., Shao-Horn, Y., and Gallant, B.M. (2021). Moving beyond 99.9% Coulombic efficiency for lithium anodes in liquid electrolytes. Nat. Energy *6*, 951–960. https://doi.org/10.1038/s41560-021-00910-w.

45. Boyle, D.T., Li, Y., Pei, A., Vilá, R.A., Zhang, Z., Sayavong, P., Kim, M.S., Huang, W., Wang, H., Liu, Y., et al. (2022). Resolving current-dependent regimes of electroplating mechanisms for fast charging lithium metal anodes. Nano Lett. *22*, 8224–8232. https://doi.org/10.1021/acs.nanolett.2c02792.

46. Ko, S., Obukata, T., Shimada, T., Takenaka, N., Nakayama, M., Yamada, A., and Yamada, Y. (2022). Electrode potential influences the reversibility of lithium-metal anodes. Nat. Energy *7*, 1217–1224. https://doi.org/10.1038/s41560-022-01144-0.

47. Lu, Z., Geng, C., Yang, H., He, P., Wu, S., Yang, Q.-H., and Zhou, H. (2022). Step-by-step desolvation enables high rate and ultra-stable sodium storage in hard carbon anodes. Proc. Natl. Acad. Sci. USA *119*, e2210203119. https://doi.org/10.1073/pnas.2210203119.

48. Kim, S., Lee, J.-A., Lee, T.K., Baek, K., Kim, J., Kim, B., Byun, J.H., Lee, H.-W., Kang, S.J., Choi, J.-A., et al. (2023). Wide-temperature-range operation of lithium-metal batteries using partially and weakly solvating liquid electrolytes. Energy Environ. Sci. *16*, 5108–5122. https://doi.org/10.1039/D3EE02106H.

49. Ma, B., Lee, Y., and Bai, P. (2021). Dynamic interfacial stability confirmed by microscopic optical operando experiments enables high-retention-rate anode-free Na metal full cells. Adv. Sci. *8*, 2005006. https://doi.org/10.1002/advs.202005006.

50. Xie, H., Cheng, H., Kumar, P., Wang, Y., Liang, H., Cai, T., Zhao, F., Cao, Z., Cavallo, L., Ma, Z., et al. (2024). Thermodynamic and kinetic behaviors of electrolytes mediated by intermolecular interactions enabling high-performance lithium-ion batteries. ACS Nano *18*, 22503–22517. https://doi.org/10.1021/acsnano.4c07986.

51. Wang, C., Zheng, Y., Chen, Z.N., Zhang, R., He, W., Li, K., Yan, S., Cui, J., Fang, X., Yan, J., et al. (2023). Robust anode-free sodium metal batteries enabled by artificial sodium formate interface. Adv. Energy Mater. *13*, 2204125. https://doi.org/10.1002/aenm.202204125.

52. Yu, Q., Xiao, Y., Zhao, S., Miao, Y., Wan, S., Zhou, L., Rong, J., Hou, G., and Chen, S. (2024). All-fluorinated low-solvation electrolytes for

high-voltage sodium metal batteries with appealing stability. Adv. Funct. Mater. *34*, 2401868. https://doi.org/10.1002/adfm.202401868.

53. Ren, Y., Lai, T., and Manthiram, A. (2023). Reversible sodium−sulfur batteries enabled by a synergistic dual-additive design. ACS Energy Lett. *8*, 2746–2752. https://doi.org/10.1021/acsenergylett.3c00833.
54. Vaidyula, R.R., Nguyen, M.H., Weeks, J.A., Wang, Y., Wang, Z., Kawashima, K., Paul-Orecchio, A.G., Celio, H., Dolocan, A., Henkelman, G., et al. (2024). Binary solvent induced stable interphase layer for ultra-long life sodium metal batteries. Adv. Mater. *36*, e2312508. https://doi.org/10.1002/adma.202312508.
55. Kim, S.C., Wang, J., Xu, R., Zhang, P., Chen, Y., Huang, Z., Yang, Y., Yu, Z., Oyakhire, S.T., Zhang, W., et al. (2023). High-entropy electrolytes for practical lithium metal batteries. Nat. Energy *8*, 814–826. https://doi.org/10.1038/s41560-023-01280-1.
56. Kilgallon, L.J., Shao-Horn, Y., and Johnson, J.A. (2023). Safe and scalable syntheses of N,N-dimethyltrifluoromethanesulfonamide (DMTMSA) and Other trifluoromethanesulfonamide solvents for high energy density battery applications. J. Org. Chem. *88*, 16644–16648. https://doi.org/10.1021/acs.joc.3c01745.
57. Noviandri, I., Brown, K.N., Fleming, D.S., Gulyas, P.T., Lay, P.A., Masters, A.F., and Phillips, L. (1999). The decamethylferrocenium/decamethylferrocene redox couple: A superior redox standard to the ferrocenium/ferrocene redox couple for studying solvent effects on the thermodynamics of electron transfer. J. Phys. Chem. B *103*, 6713–6722.
58. Hobold, G.M., Kim, K.-H., and Gallant, B.M. (2023). Beneficial vs. inhibiting passivation by the native lithium solid electrolyte interphase revealed by electrochemical Li^+ exchange. Energy Environ. Sci. *16*, 2247–2261. https://doi.org/10.1039/D2EE04203G.
59. Zeng, Y., Smith, R.B., Bai, P., and Bazant, M.Z. (2014). Simple formula for Marcus–Hush–Chidsey kinetics. J. Electroanal. Chem. *735*, 77–83. https://doi.org/10.1016/j.jelechem.2014.09.038.
60. Kirilov, A., Mintun, E., Ravi, N., Mao, H., Rolland, C., Gustafson, L., Xiao, T., Whitehead, S., Berg, A.C., Lo, W.Y., et al. (2023). Segment anything. In Proceedings of the IEEE/CVF International Conference on Computer Vision, pp. 4015–4026.
61. Parrish, R.M., Burns, L.A., Smith, D.G.A., Simmonett, A.C., DePrince, A.E., Hohenstein, E.G., Bozkaya, U., Sokolov, A.Y., Di Remigio, R., Richard, R.M., et al. (2017). Psi4 1.1: An open-source electronic structure program emphasizing automation, advanced libraries, and interoperability. J. Chem. Theor. Comput. *13*, 3185–3197. https://doi.org/10.1021/acs.jctc.7b00174.
62. Mitternacht, S. (2016). FreeSASA: an open source C library for solvent accessible surface area calculations. F1000Res *5*, 189. https://doi.org/10.12688/f1000research.7931.1.
63. Wang, Y., Wang, J., Cao, Z., and Barati Farimani, A.B. (2022). Molecular contrastive learning of representations via graph neural networks. Nat. Mach. Intell. *4*, 279–287. https://doi.org/10.1038/s42256-022-00447-x.
64. Stenutz, R. Gutmann acceptor and donor number. (retrieved July 27, 2024) https://www.stenutz.eu/chem/solv21.php?sort=6.
65. Plimpton, S. (1995). Fast parallel algorithms for short-range molecular dynamics. J. Comput. Phys. *117*, 1–19. https://doi.org/10.1006/jcph.1995.1039.
66. Jorgensen, W.L., Maxwell, D.S., and Tirado-Rives, J. (1996). Development and testing of the OPLS all-atom force field on conformational energetics and properties of organic liquids. J. Am. Chem. Soc. *118*, 11225–11236. https://doi.org/10.1021/ja9621760.
67. Dodda, L.S., Vilseck, J.Z., Tirado-Rives, J., and Jorgensen, W.L. (2017). 1.14*CM1A-LBCC: Localized bond-charge corrected CM1A charges for condensed-phase simulations. J. Phys. Chem. B *121*, 3864–3870. https://doi.org/10.1021/acs.jpcb.7b00272.

Joule, Volume *9*

Supplemental information

Hybrid solvating electrolytes for practical sodium-metal batteries

Weiyin Chen, Jin-Sung Park, Choah Kwon, Christian O. Plaza-Rivera, Chia-Wei Hsu, Jason Khoi Phong, Landon James Kilgallon, Daniel Wang, Tao Dai, So Yeon Kim, Guanzhou Zhu, Yifan Gao, Zhichu Ren, Zhen Zhang, Hyojun Lim, Yang Shao-Horn, Jeremiah A. Johnson, and Ju Li

Supplemental Information

Hybrid solvating electrolytes for practical sodium metal batteries

Weiyin Chen[1,2], Jin-Sung Park[1,2,5,6], Choah Kwon[1,2], Christian O. Plaza-Rivera[2], Chia-Wei Hsu[2], Jason Khoi Phong[2], Landon James Kilgallon[3], Daniel Wang[4], Tao Dai[1,2], So Yeon Kim[1,2], Guanzhou Zhu[1,2], Yifan Gao[1,2], Zhichu Ren[2], Zhen Zhang[2], Hyojun Lim[1,2], Yang Shao-Horn[2,4], Jeremiah Johnson[3], Ju Li[1,2,*]

[1]Department of Nuclear Science and Engineering, Massachusetts Institute of Technology, Cambridge, MA, 02139, USA

[2]Department of Materials Science and Engineering, Massachusetts Institute of Technology, Cambridge, MA, 02139, USA

[3]Department of Mechanical Engineering, Massachusetts Institute of Technology, Cambridge, MA, 02139, USA

[4]Department of Chemistry, Massachusetts Institute of Technology, Cambridge, MA, 02139, USA

[5]Department of Materials Science and Engineering, Ajou University, Suwon 16499, Republic of Korea

[6]Department of Energy Systems Research, Ajou University, Suwon 16499, Republic of Korea

*Email: liju@mit.edu

Abbreviations

AGG	Aggregate
BCC	Body-centered cubic
BTFE	Bis(2,2,2-trifluoroethyl) ether
CDE	Conventional dilute electrolyte
CE	Coulombic efficiency
CIP	Contact-ion pair
Cl-DEE	1,2-bis(2-chloroethoxy)-ethyl ether
CN	Coordination number
DEE	1,2-diethoxyethane
DETMSA	N,N-diethyltrifluoromethane sulfonamide
DMC	Dimethyl carbonate
DME	1,2-dimethoxyethane
DMTMSA	N,N-dimethyltrifluoromethane sulfonamide
DMTP	1,1,1,2,2,3,4,5,5,5-decafluoro-3-methoxy-4-(trifluoromethyl)-pentane
DN	Donor number
DTD	1,3,2-dioxathiolane 2,2-dioxide
ESP	Electrostatic potential
FEC	Fluoroethylene carbonate
FEMC	Methyl (2,2,2-trifluoroethyl) carbonate
G2	Diglyme (Diethylene glycol dimethyl ether)
HCE	High-concentration electrolyte
HFME	Hexafluoroisopropyl methyl ether

43	HSE	Hybrid solvating electrolyte
44	LHCE	Localized high-concentration electrolyte
45	LiFSI	Lithium bis(fluorosulfonyl)imide
46	Mor-TMSA	N,N-Mor trifluoromethane sulfonamide
47	NaFSI	Sodium bis(fluorosulfonyl)imide
48	NaFTFSI	Sodium (fluorosulfonyl)(trifluoromethanesulfonyl)imide
49	NaTFSI	Sodium bis(trifluoromethanesulfonyl)imide
50	NaOTf	Sodium trifluoromethanesulfonate
51	PC	Propylene carbonate
52	Pip-TMSA	N,N-Pip trifluoromethane sulfonamide
53	Pyr-TMSA	N,N-Pyr trifluoromethane sulfonamide
54	[Pyr14][FSI]	N-methyl-N-butyl pyrrolidinium bis(fluorosulfonyl)imide
55	SEI	Solid electrolyte interphase
56	SMB	Sodium-metal battery
57	SS	Stainless steel
58	SSIP	Solvent-separated ion pair
59	TEGDME	Tetraethylene glycol dimethyl ether
60	TGDE	Triethylene glycol dimethyl ether
61	THF	Tetrahydrofuran
62	TM	2,2,2-trifluoroethyl methanesulfonate
63	TMP	Trimethyl phosphate
64	TMS	Tetramethylene sulfone
65	TTE	1,1,2,2-tetrafluoroethyl-2,2,3,3-tetrafluoropropyl ether

V_{ox}	Oxidative potential
V_{red}	Reductive potential
WSE	Weakly solvating electrolyte

Note S1. Solvents labeling for HSEs.

The solvents are pre-screened into three groups based on their feature descriptors listed in Table S1, including donor number (DN), and electrostatic potential (ESP). DN describes the Lewis-type donor properties of a solvent[40]. ESP is induced in the space surrounding a molecule by its nuclei and electrons and reflects an unbalanced distribution of charge[41,42]. ESP_{min} and ESP_{max} mean the most negative and the most positive surface potentials, respectively.

1) In the green region, the solvents are diluents or anti-solvents. They generally show a high ESP_{min} $\geq$ -1.0 eV, and most of the solvents have a DN value $\leq$ 10 kcal mol^{-1}. Some diluents, such as (Trifluoromethoxy)benzene, show a large DN value of 15 kcal mol^{-1}.

2) In the orange region, the solvents are strongly solvating solvents, They generally show a high DN $\geq$ 15 kcal mol^{-1} and the ESP_{min} $\leq$ -1.4 eV. Some tridentate solvents, such as diglyme (G2) shows a lower ESP_{min} ~-1.1 eV.

3) In the blue region, the solvents are weakly solvating solvents. They generally shows a middle ESP_{min} between -1.0 and -1.4 eV, and their DN values are in the range of 10 ~ 15 kcal mol^{-1}.

Note S2. Calculation of de-solvation activation energy.

The ionic conductivity (σ) of different hybrid solvating electrolytes was calculated based on electrochemical impedance spectroscopy (EIS) results using a symmetric coin cell with Al electrodes.

$$\sigma = L/(R \times A) \quad \text{(S1)}$$

L is the distance between the electrodes. A is the area of the electrodes. And R is the resistance measured from X intercept based on EIS results.

The Nernst-Einstein equation describes the relationship between the molar limiting conductivity (Λ_{lim}) and D/T.

$$\Lambda_{lim} = z^2 \times (\frac{F^2}{R}) \times (\frac{D}{T}) \quad \text{(S2)}$$

Z is the charge of ion. F is Faraday's constant. R is the gas constant. T is the absolute temperature. And D is the diffusion coefficient, which follows the Arrhenius form.

$$D \propto exp\ (E_a/(RT)) \quad \text{(S3)}$$

E_a is the de-solvation activation energy. The molar limiting conductivity is the molar conductivity (Λ) of a solution at infinite dilution. Here, the same electrolyte was measured at different temperatures. Therefore, molar conductivity Λ is proportional to Λ_{lim}. Therefore, the graph between (σT) and $1000/T$ were plotted, and the slope (k) was used to calculate the activation energy (Ea).

$$E_a = 1000 \times R \times k \quad \text{(S4)}$$

Note S3. THF polymerization related discussion.

For 1 m NaFSI THF electrolyte, the gel formed after room temperature storage for ~1 week, which was related to the open-ring reaction between the cyclic ether THF and cation Na^+, followed by the subsequent polymerization. It was noted that the polymerized THF accounted for only ~1% for 1 m NaFSI THF. The heat treatment could accelerate the THF polymerization and ~33% THF was converted after 1 m NaFSI THF was stirred at 60 °C for 6 days as shown in **Figure S10**. However, polymerized THF was not observed for 1 m NaFSI DMTMSA/THF after the same heat treatment, indicating that HSEs are more stable. HSEs with optimized solvation structure utilized THF solvent molecules to coordinate Na^+ and there was no "free" THF molecules, which could be the important reason for this difference mentioned above.

Design concept of hybrid solvating electrolytes

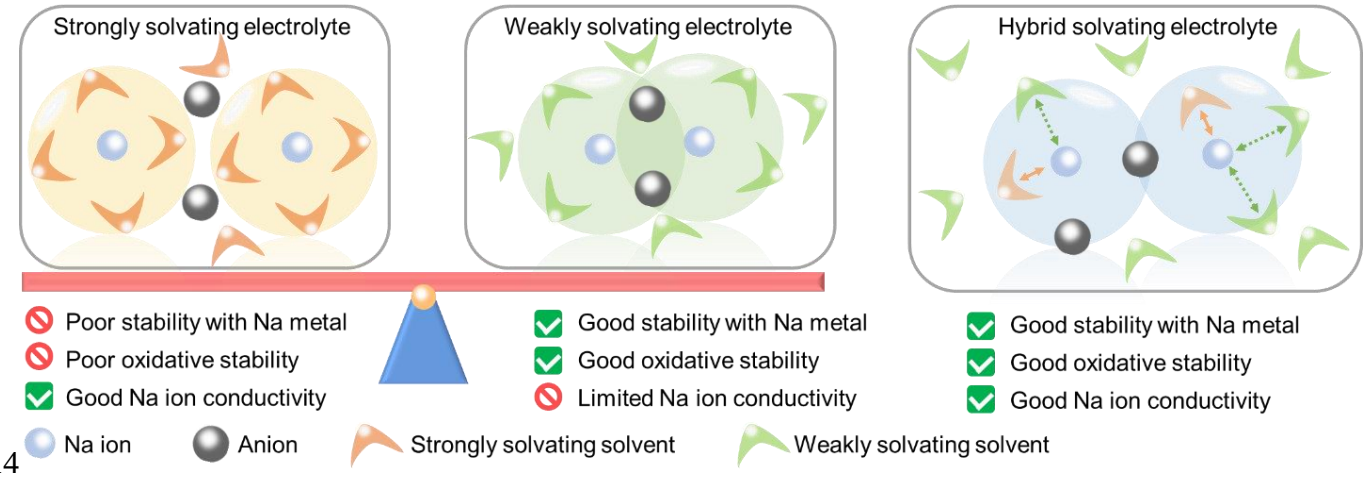

Figure S1. Scheme about single-salt-single-solvent systems and hybrid solvating electrolytes. Comparison between strongly and weakly solvating electrolytes, and design of hybrid solvating electrolytes combined with strongly and weakly solvating solvents.

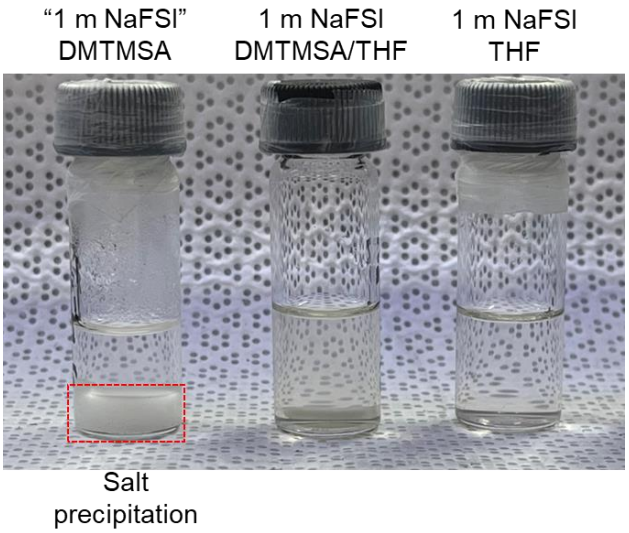

Figure S2. The photos of different electrolytes.

"1 m NaFSI" DMTMSA, 1 m NaFSI DMTMSA/THF and 1 m NaFSI THF.

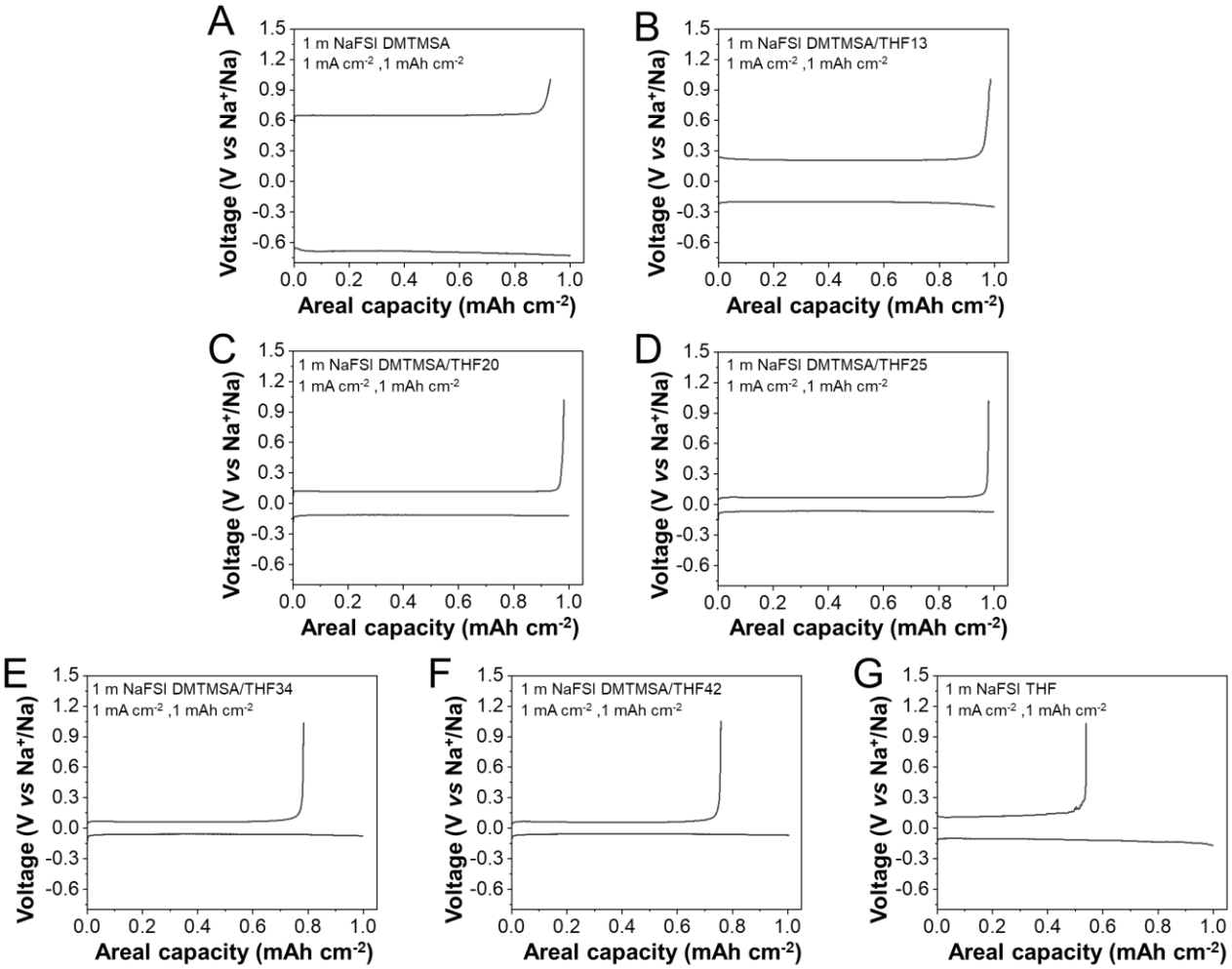

Figure S3. Polarization curves of various hybrid solvating electrolytes.

(A-G) The hybrid solvating electrolytes use different molar ratios between DMTMSA and THF solvents in this example. The number followed by THF indicates the molar ratio of THF solvent. The same nomenclature is used below. For example, "DMTMSA/THF13" means the molar ratio of THF is 13% and therefore, DMTMSA accounts for 87%. The tests are carried out using Na||Cu half-cell at 1 mA cm^{-2} with the areal capacity of 1 mAh cm^{-2} for all the hybrid solvating electrolytes.

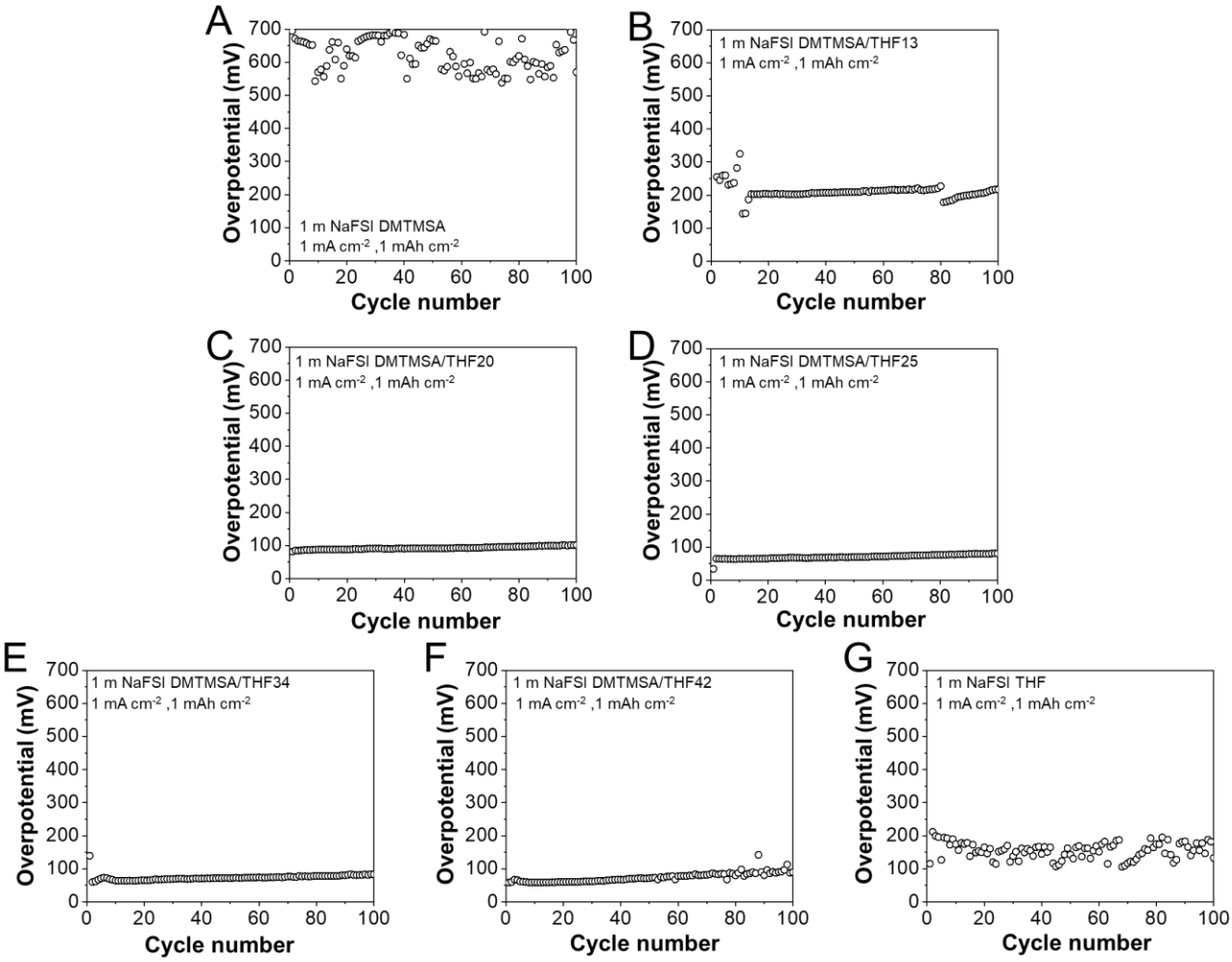

Figure S4. Cycling overpotential of various hybrid solvating electrolytes.

(A-G) The hybrid solvating electrolytes use different molar ratios between DMTMSA and THF solvents in this example. The tests are carried out using Na||Cu half-cell at 1 mA cm^{-2} with the areal capacity of 1 mAh cm^{-2}.

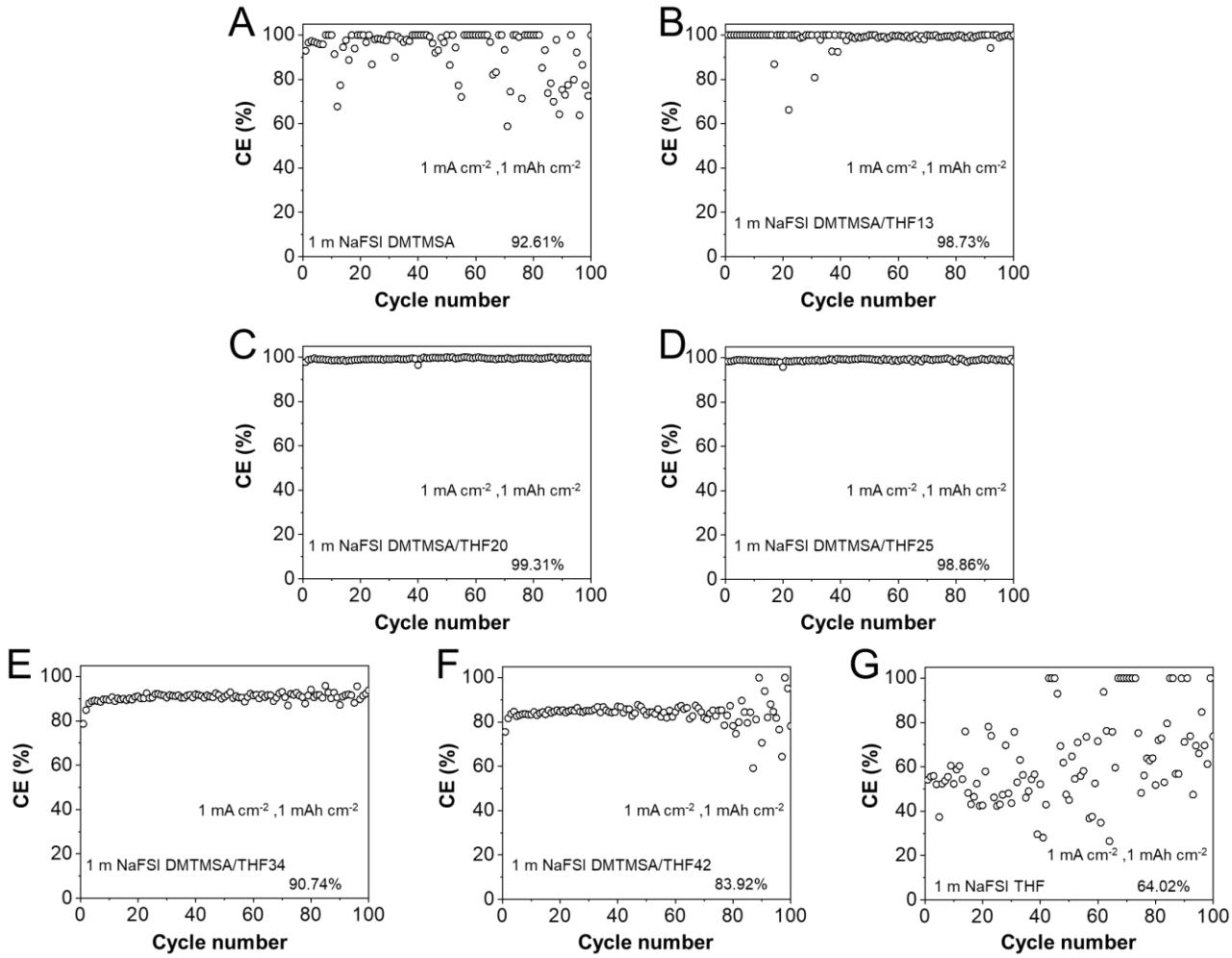

Figure S5. Electrochemical cycling performance of various hybrid solvating electrolytes. (A-G) The hybrid solvating electrolytes use different molar ratios between DMTMSA and THF solvents in this example. The calculated CE reflects the average value during the first 100 cycles using Na||Cu half-cell at 1 mA cm^{-2} with the areal capacity of 1 mAh cm^{-2}.

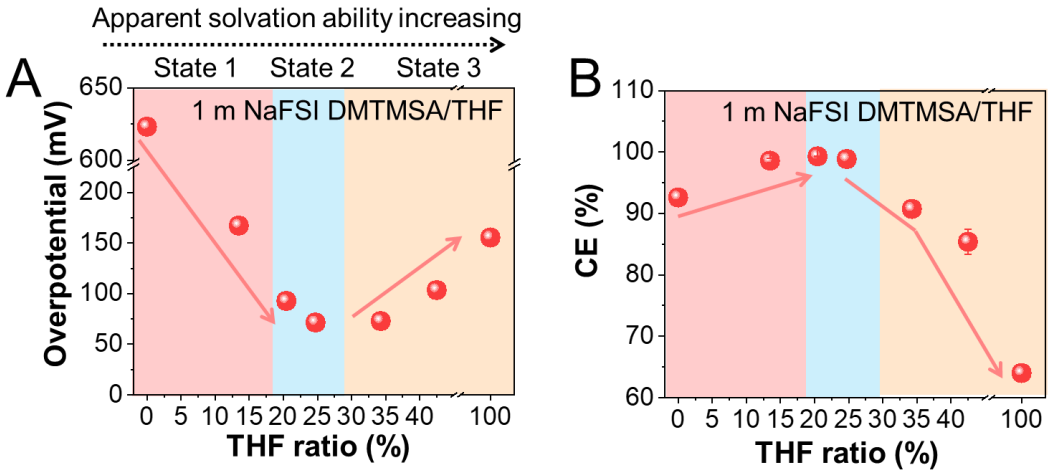

Figure S6. Components-properties relationships of various hybrid solvating electrolytes. (A) The relationship between THF ratio and cycling overpotential. (B) The relationship between THF ratio and CE**.** The calculated overpotential and CE reflect the average values during the first 100 cycles using Na||Cu half-cell at 1 mA cm^{-2} with the areal capacity of 1 mAh cm^{-2}.

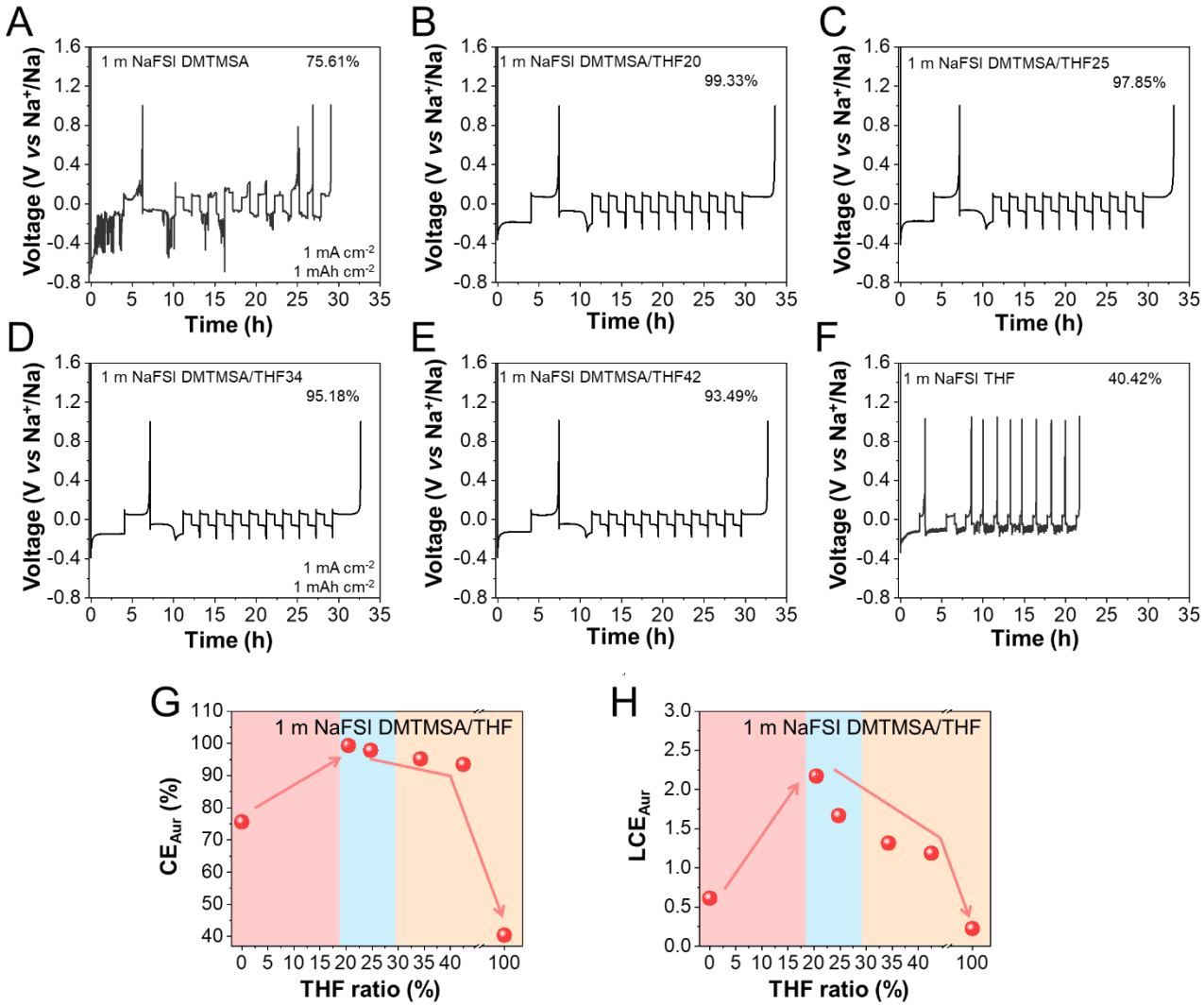

Figure S7. Components-properties relationships between THF ratio and CE_{Aur}.

(A-F) Aurbach method measurement of Na^0 coulombic efficiency in Na||Cu half cells using different electrolytes.

(G) The relationship between THF ratio and CE_{Aur}. The CE_{Aur} reflects the value evaluated by modified Aurbach method using Na||Cu half-cell at 1 mA cm^{-2} with the areal capacity of 1 mAh cm^{-2}.

(H) The relationship between THF ratio and LCE_{Aur}. $LCE_{Aur} = -\log_{10}(1-CE_{Aur})$.

Electrochemical evaluation of hybrid solvating electrolytes

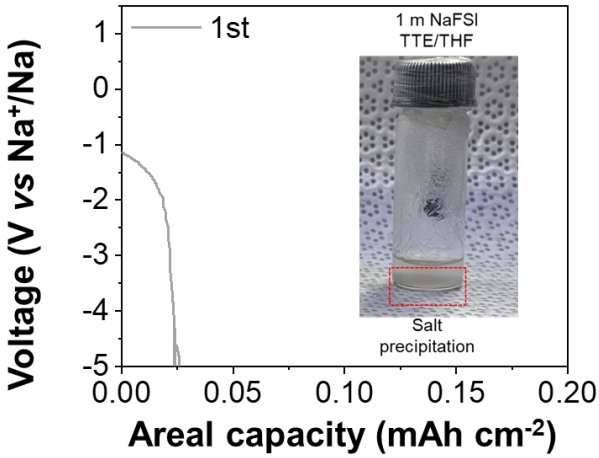

Figure S8. The role of weakly solvating electrolyte.

The voltage profile of the 1 m NaFSI THF/TTE at 0.4 mA cm^{-2}. DMTMSA is replaced by the same molar ratio of TTE, which is the common diluent used in the LHCE. The molar ratio between TTE and THF is 3:1. There is still white suspension within the electrolyte after overnight stirring and the supernatant is used for the electrochemical tests.

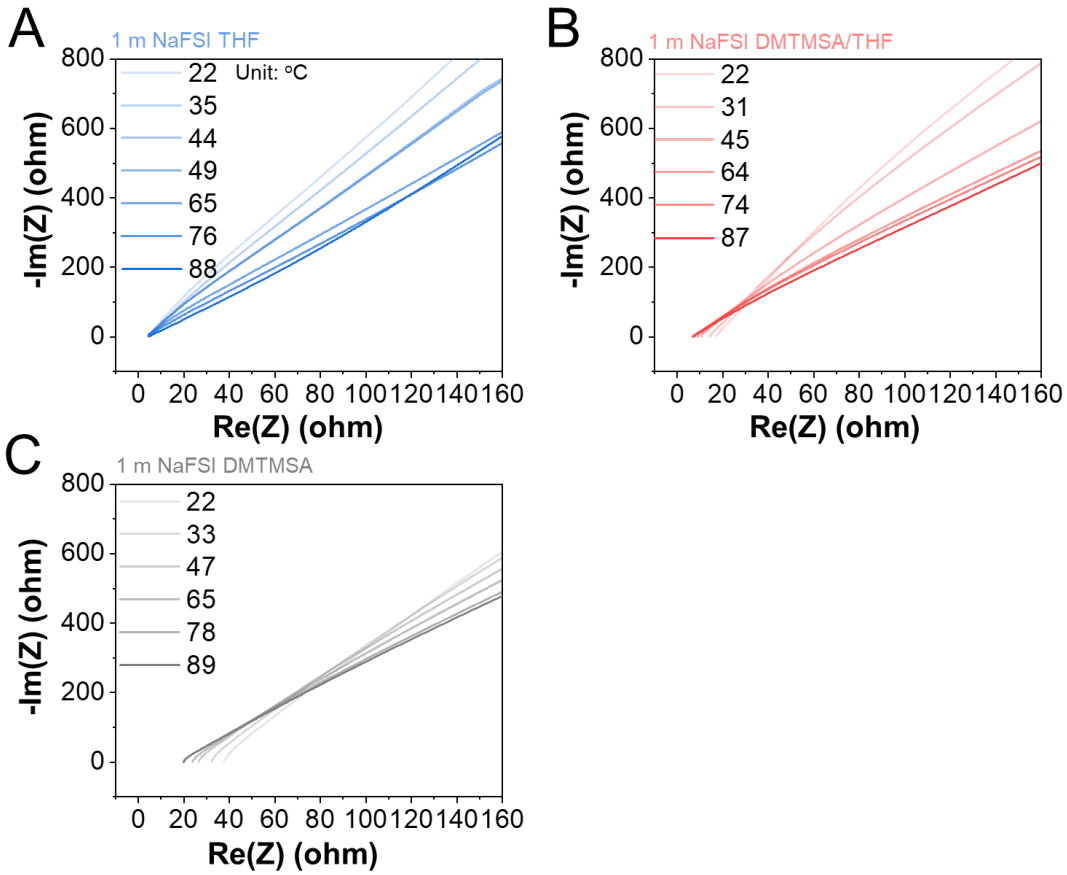

Figure S9. Electrochemical impedance spectroscopy results of hybrid solvating electrolytes at different temperatures.

(A) Optimized hybrid solvating electrolyte.

(B) Strongly solvating electrolyte.

(C) Weakly solvating electrolyte.

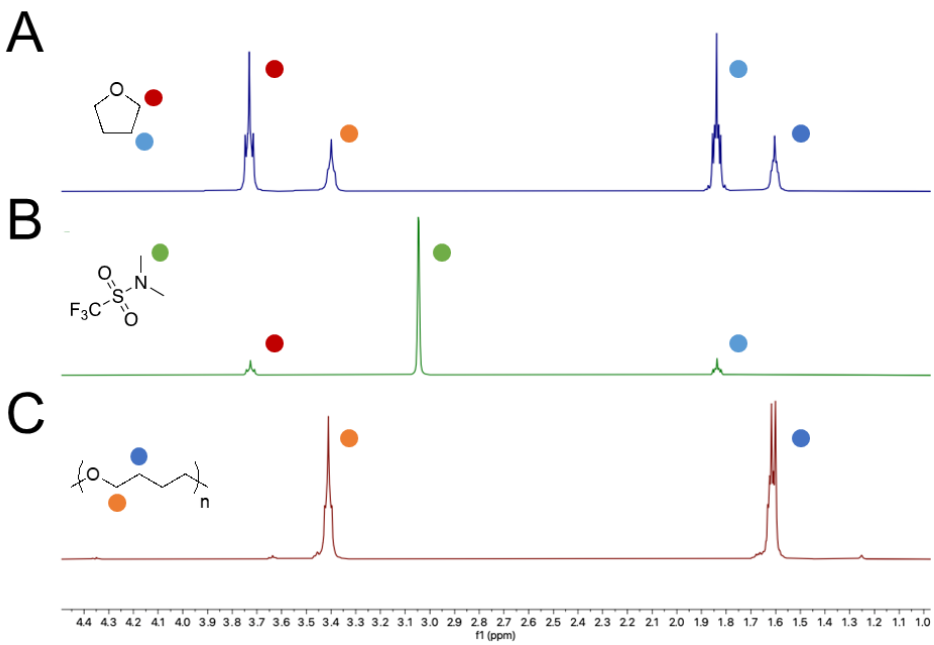

Figure S10. NMR results for various samples.

(A) 1 m NaFSI THF after heat treatment at 60 °C for 6 days. ~33% THF is polymerized.

(B) 1 m NaFSI DMTMSA/THF after heat treatment at 60 °C for 6 days.

(C) Polymerized THF (~2.9k).

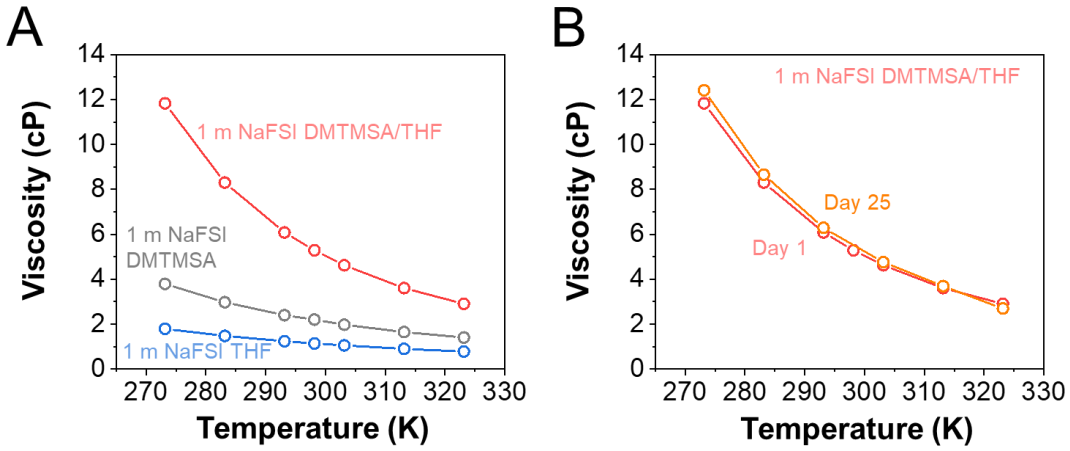

Figure S11. Viscosity of hybrid solvating electrolytes at different temperatures.

(A) Viscosity of different electrolytes under various temperatures. The tests are carried out one day after the electrolyte preparation.

(B) The viscosity of hybrid solvating electrolyte on Day 1 and Day 25.

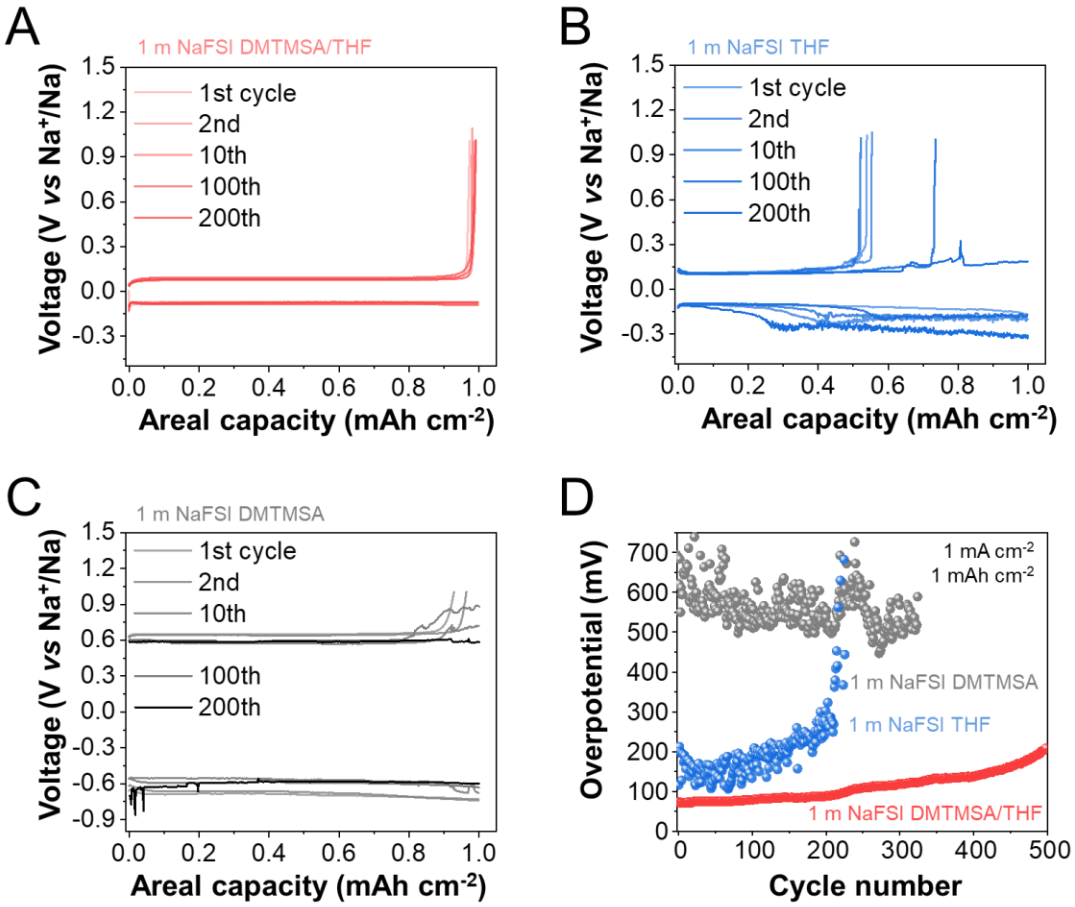

Figure S12. Comparison of electrochemical cycling performance using different electrolytes. (A-C) The voltage profile of different electrolytes at 1.0 mA cm^{-2} during 1st, 2nd, 10th, 100th and 200th cycle, respectively. (A) Optimized hybrid solvating electrolyte. (B) Strongly solvating electrolyte. (C) Weakly solvating electrolyte.

(D) The evolution of cycling overpotentials for different electrolytes.

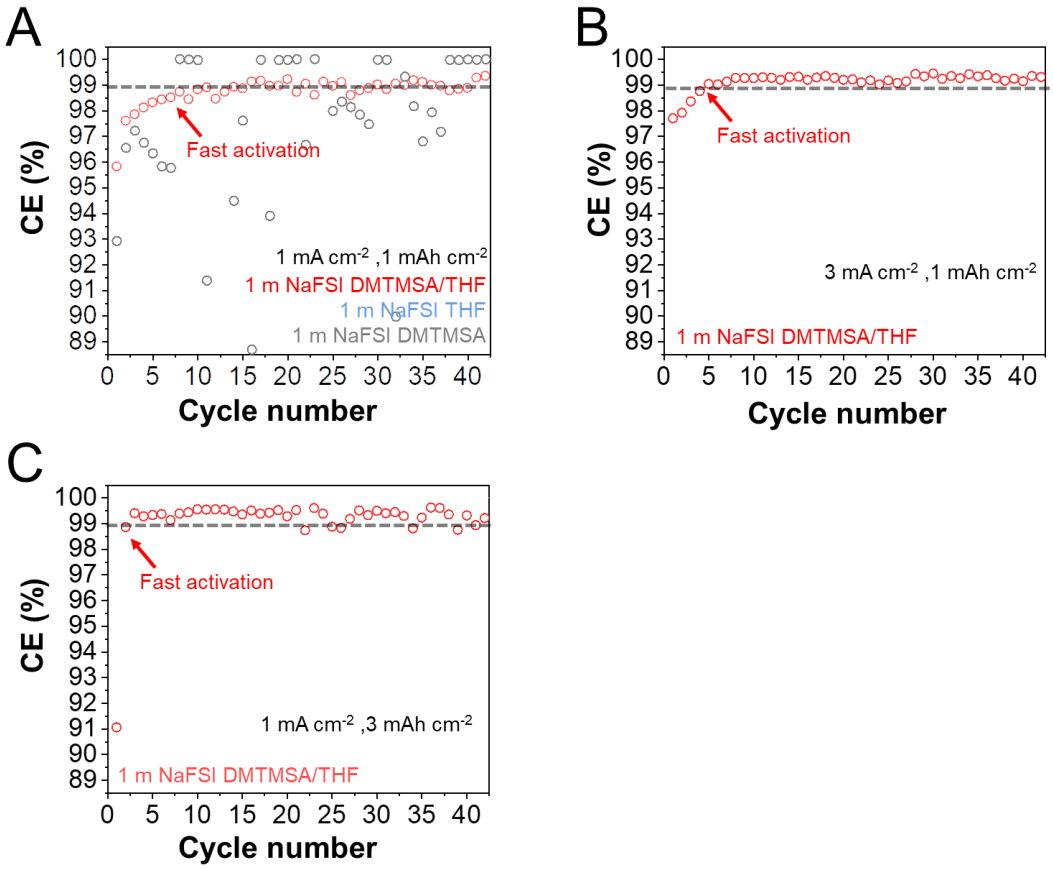

Figure S13. Electrochemical activation performance of hybrid solvating electrolytes.

(A) Cycling performance of hybrid solvated electrolyte and other electrolytes at 1.0 mA cm^{-2} with the areal capacity of 1 mAh cm^{-2}.

(B) Cycling performance of hybrid solvated electrolyte at 3.0 mA cm^{-2}.

(C) Cycling performance of hybrid solvated electrolyte with the areal capacity of 3.0 mAh cm^{-2}. The graph highlights the fast activation properties of hybrid solvated electrolyte. Activation cycle means the cycle number of the cells required for CE reaching 99.0% during complete Na^0 plating and stripping.

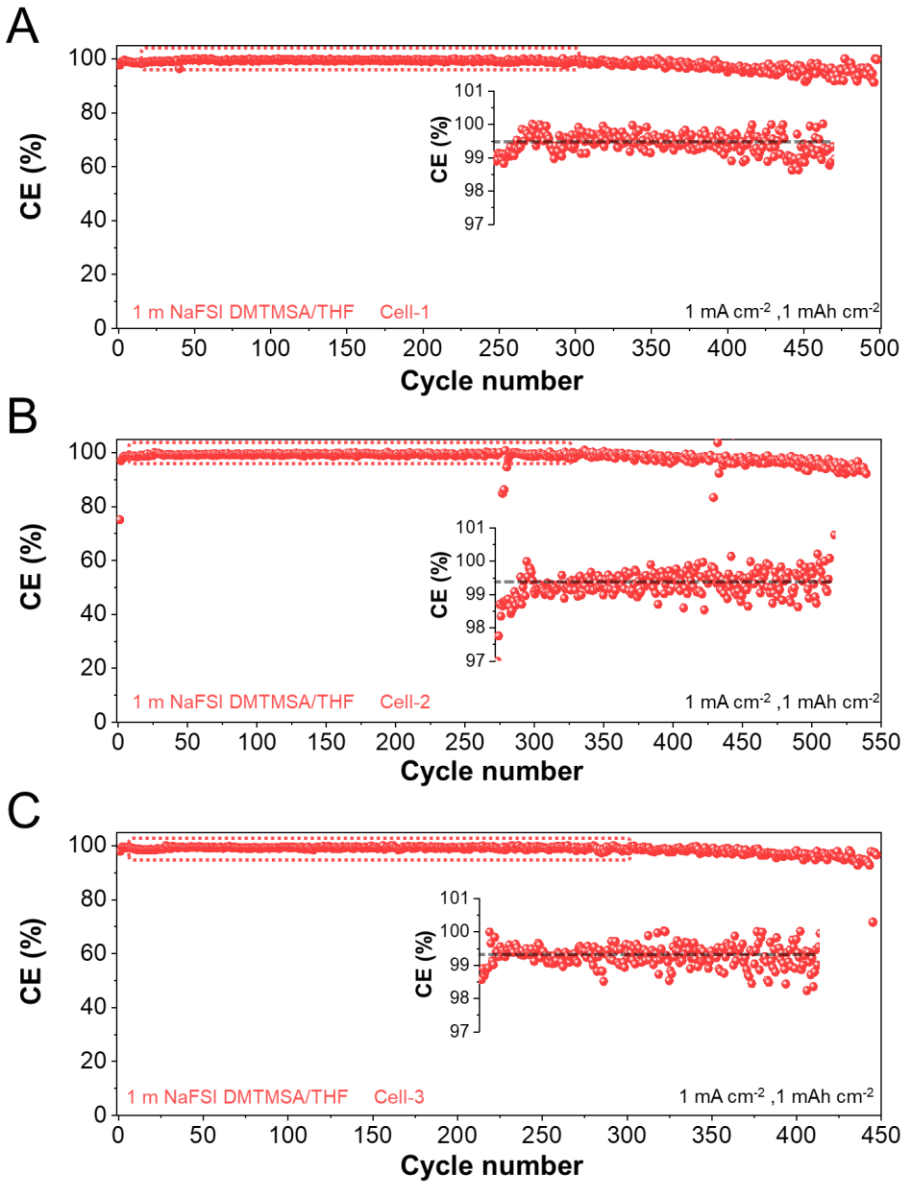

Figure S14. Electrochemical cycling performance of hybrid solvating electrolytes. (A-C) Cycling performance of three parallel Na||Cu half cells at 1.0 mA cm^{-2} with the areal capacity of 1 mAh cm^{-2} using hybrid solvating electrolytes.

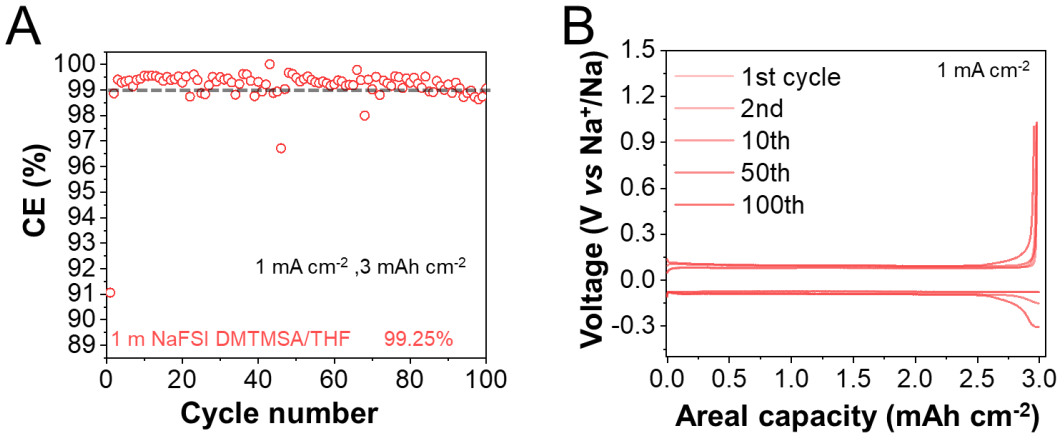

Figure S15. Electrochemical cycling performance using hybrid solvating electrolytes.

(A) Cycling performance of hybrid solvated electrolyte at 1.0 mA cm^{-2} with the areal capacity of 3.0 mAh cm^{-2}.

(B) The voltage profile of hybrid solvating electrolyte at 1.0 mA cm^{-2} with the areal capacity of 3.0 mAh cm^{-2} during 1st, 2nd, 10th, 50th, and 100th cycle, respectively.

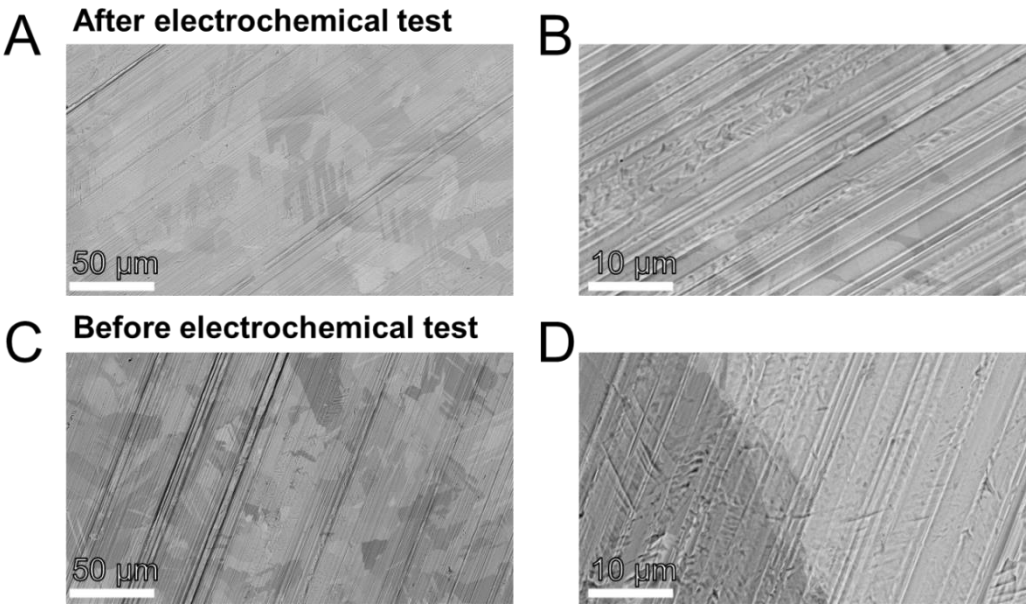

Figure S16. Corrosion behavior of hybrid solvating electrolytes towards Cu current collector.

(A-B) SEM images of Cu current collector after the electrochemical test.

(C-D) SEM images of Cu current collector before the electrochemical test.

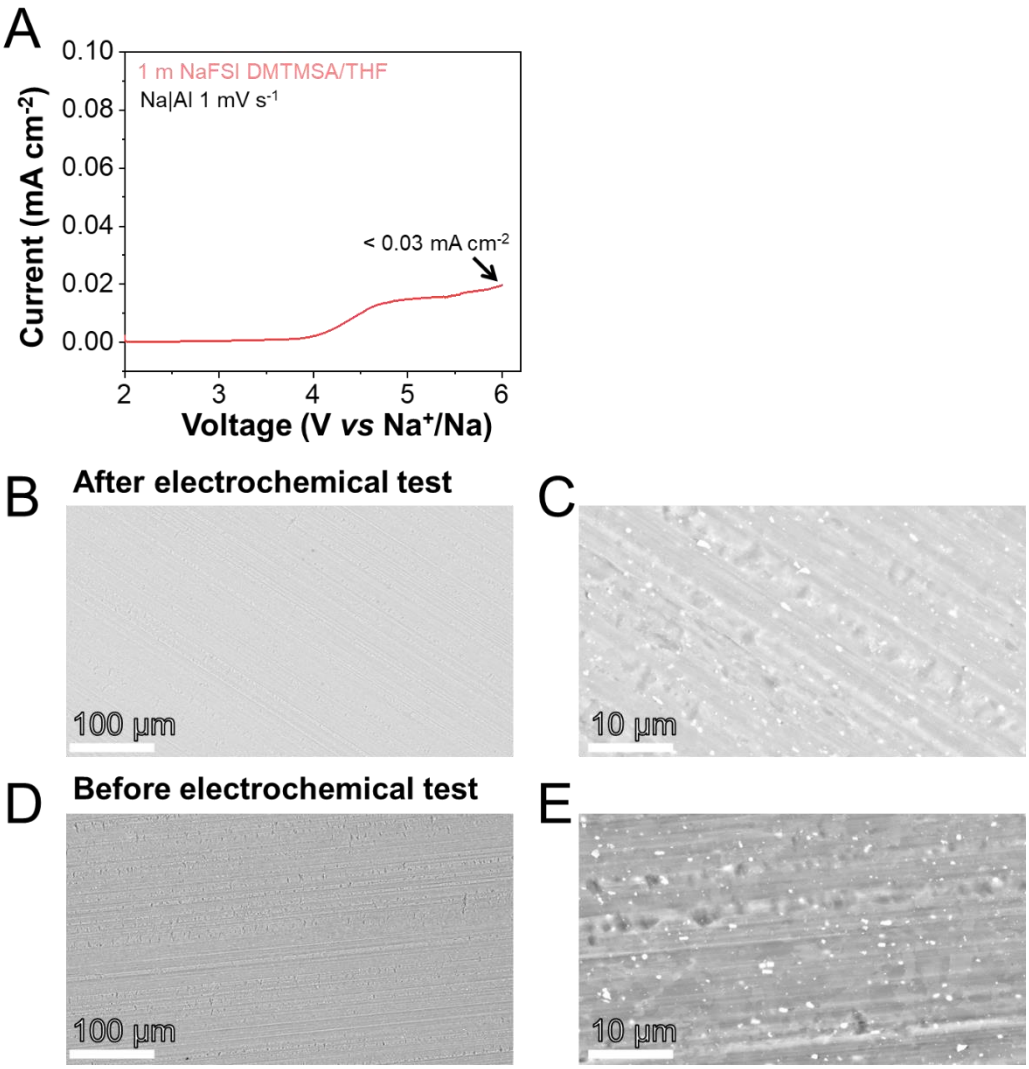

Figure S17. Corrosion behavior of HSEs towards Al current collector.

(A) Oxidative stability of 1 m NaFSI DMTMSA/THF in Na||Al half cell.

(B-C) SEM images of Al current collector after the electrochemical test.

(D-E) SEM images of Al current collector before the electrochemical test.

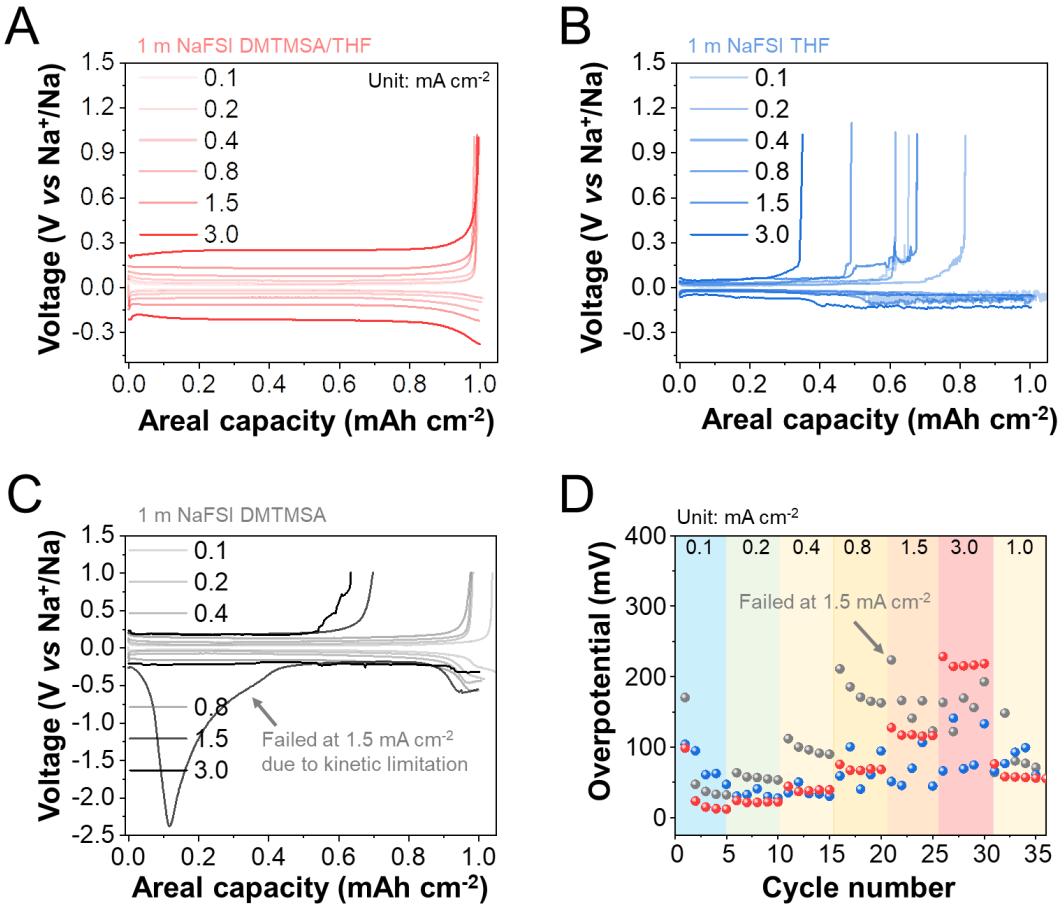

Figure S18. Comparison of electrochemical rate performance using different electrolytes. (A-C) The voltage profile of different electrolytes at different current densities, including 0.1, 0.2, 0.4, 0.8, 1.5, and 3.0 mA cm^{-2} respectively. (A) Optimized hybrid solvating electrolytes. (B) Strongly solvating electrolyte. (C) Weakly solvating electrolyte.

(D) The cycling overpotential for different electrolytes during the electrochemical rate tests.

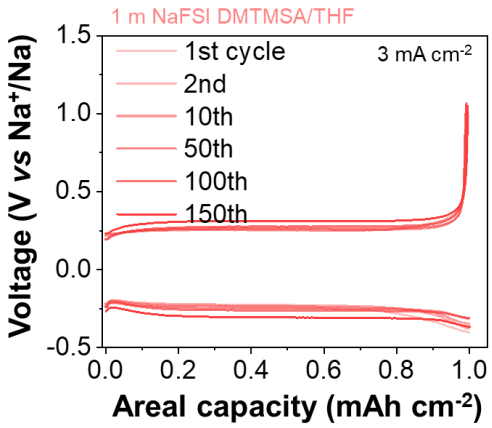

Figure S19. Fast electrochemical cycling performance using hybrid solvating electrolyte. The voltage profile of hybrid solvating electrolyte at 3.0 mA cm^{-2} with the areal capacity of 1 mAh cm^{-2} during 1st, 2nd, 10th, 50th, 100th and 150th cycle, respectively.

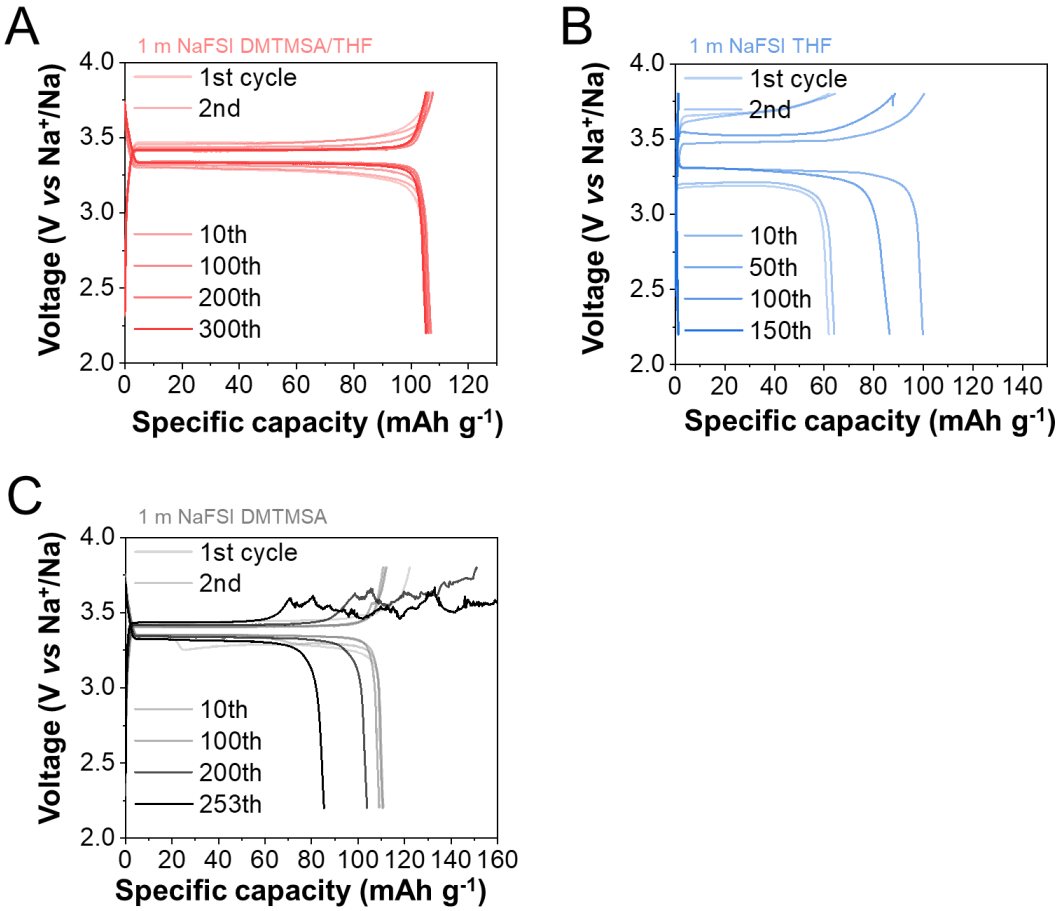

Figure S20. Comparison of electrochemical cycling performance using $Na_3V_2(PO_4)_3$ cathode. (A-C) The voltage profile of different electrolytes using 0.2 C rate (1 C = 120 mA g^{-1}) at different cycles, including 1st, 10th, 100th, 200th and 300th cycle, respectively, respectively. (A) Optimized hybrid solvating electrolyte. (B) Strongly solvating electrolyte. (C) Weakly solvating electrolyte.

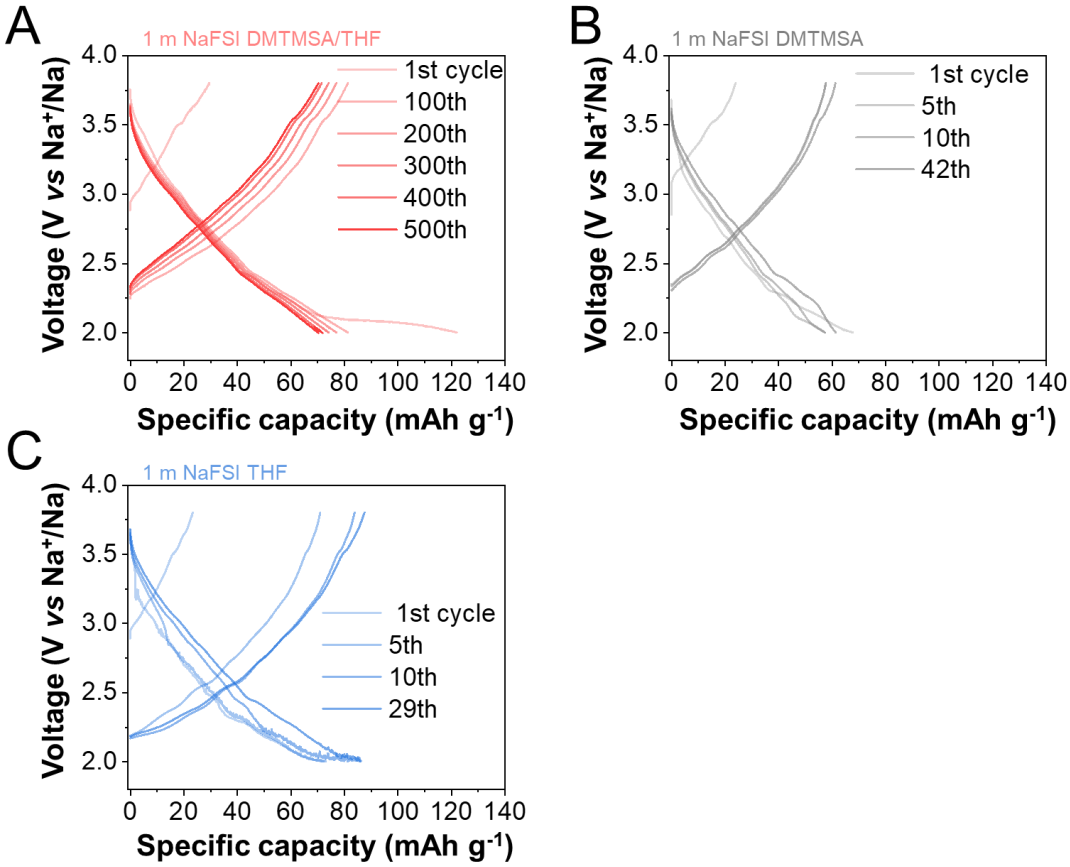

Figure S21. Electrochemical cycling performance using $Na_{0.44}MnO_2$ cathode.

(A-C) The voltage profiles of different electrolytes using 0.3 C rate (1 C ≡ 105 mA g^{-1}) at different cycles. (A) hybrid solvating electrolyte. (B) Weakly solvating electrolyte. (C) Strongly solvating electrolyte.

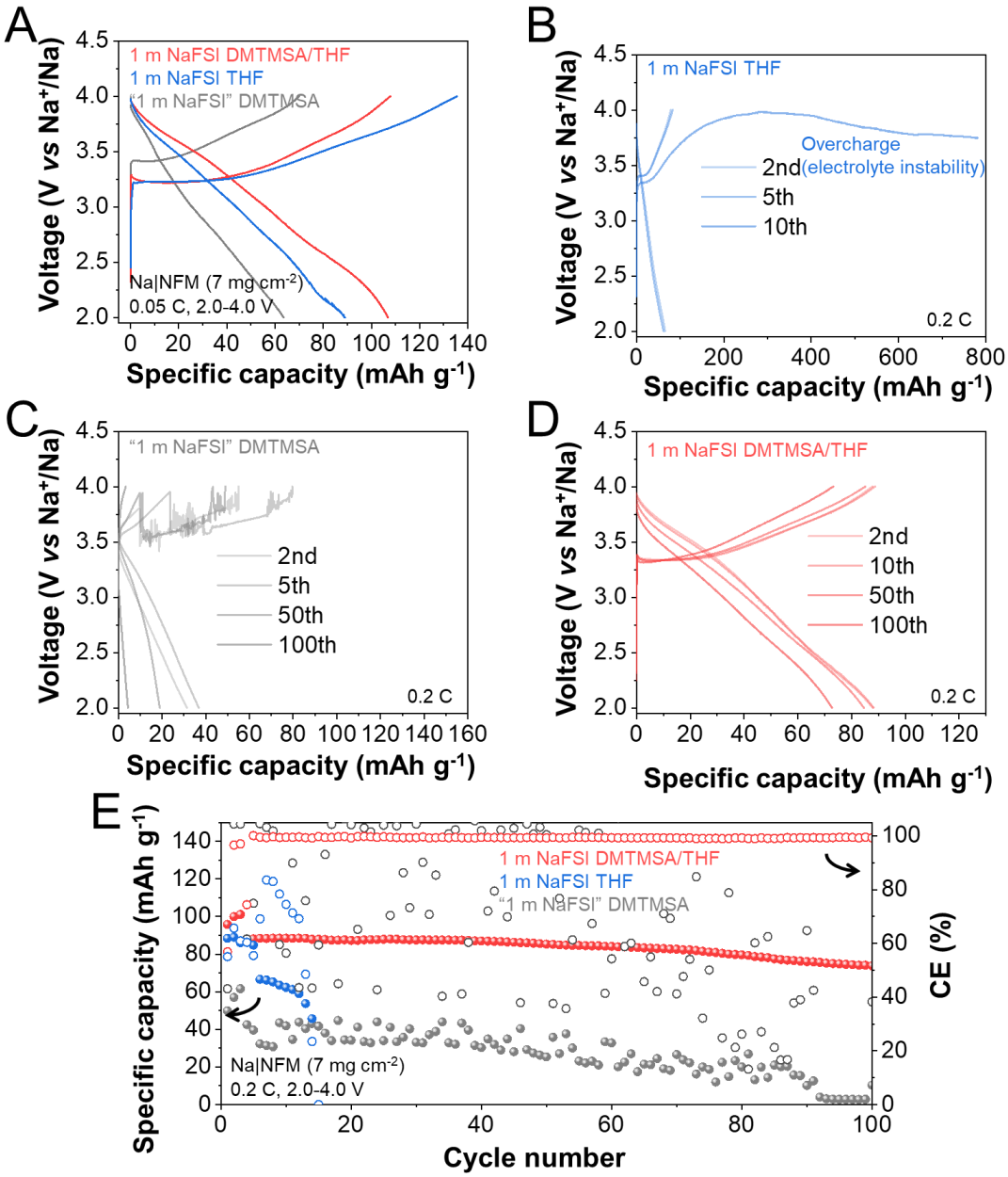

Figure S22. Electrochemical cycling performance using $NaNi_{0.33}Fe_{0.33}Mn_{0.33}O_2$ cathode. (A) The voltage profiles of different electrolytes at 0.05 C (1 C ≡ 127 mA g^{-1}). (B-D) The voltage profiles of different electrolytes using 0.2 C rate at different cycles. (B) Strongly solvating electrolyte. (C) Weakly solvating electrolyte. (D) Optimized hybrid solvating electrolyte. (E) Cycling performance using different electrolytes.

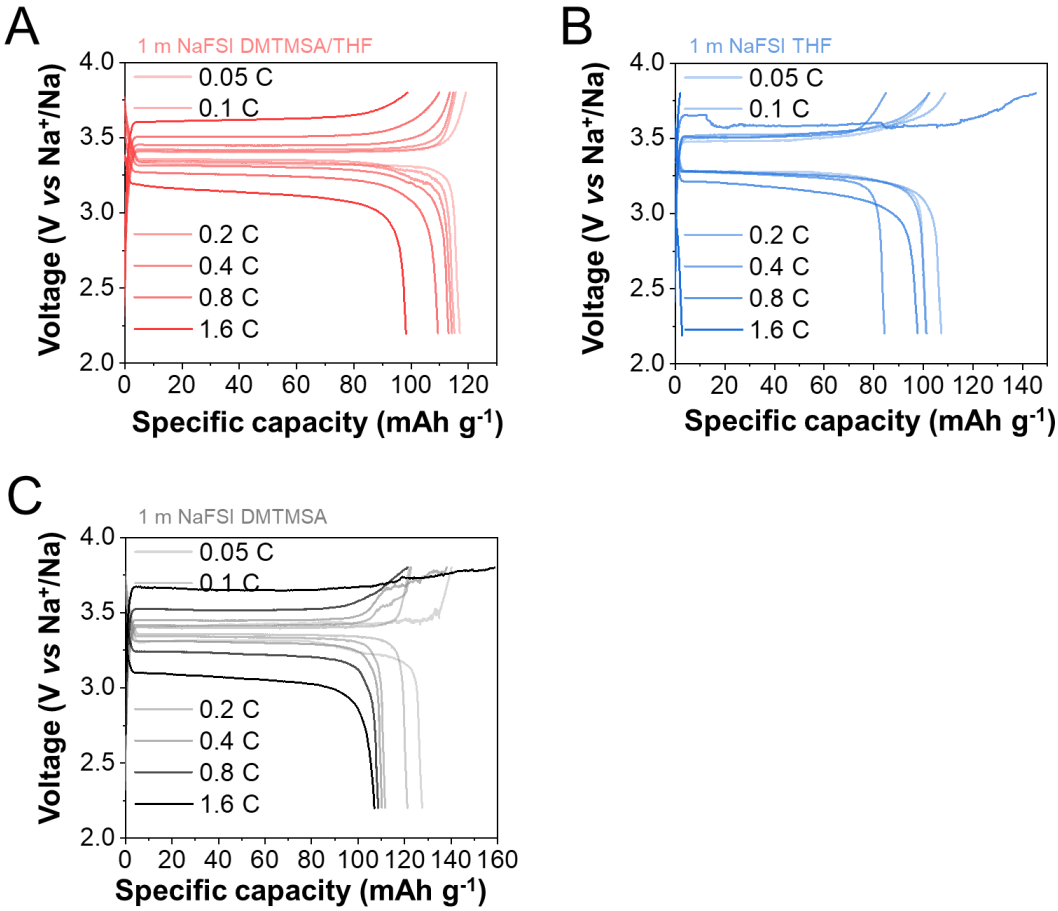

Figure S23. Comparison of electrochemical rate performance using $Na_3V_2(PO_4)_3$ cathode. (A-C) The voltage profile of different electrolytes at different C-rate (1 C ≡ 120 mA g^{-1}), including 0.05, 0.1, 0.2, 0.4, 0.8, and 1.6 C, respectively. (A) Optimized hybrid solvating electrolyte. (B) Strongly solvating electrolyte. (C) Weakly solvating electrolyte.

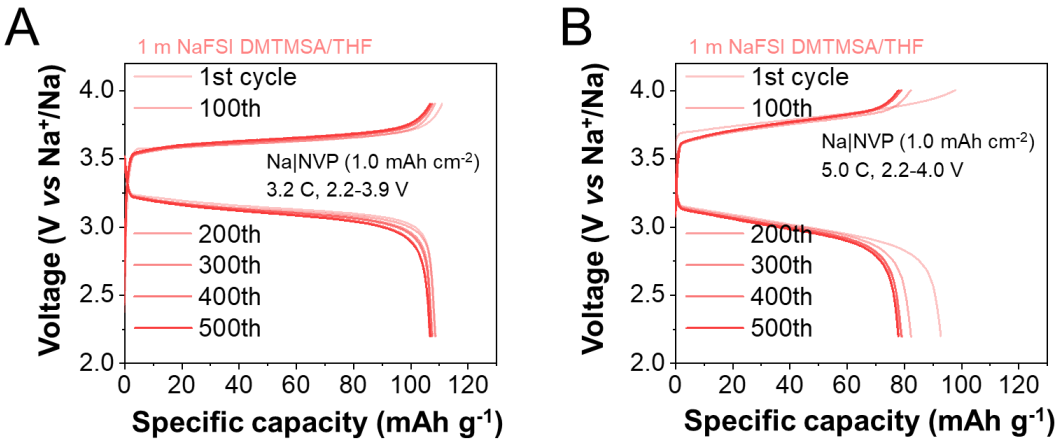

Figure S24. Electrochemical fast cycling performance using $Na_3V_2(PO_4)_3$ cathode. (A-B) The voltage profile of optimized hybrid solvating electrolytes using (A) 3.2 C and (B) 5.0 C rate (1 C ≡ 120 mA g^{-1}) at different cycles, including 1st, 100th, 200th, 300th, 400th and 500th cycle, respectively.

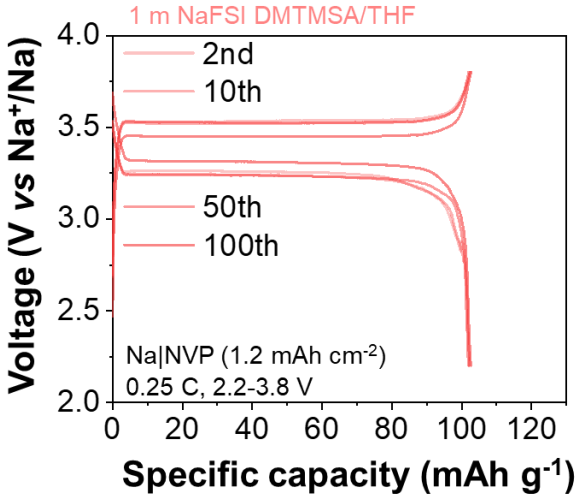

Figure S25. Electrochemical cycling performance using Na||$Na_3V_2(PO_4)_3$ pouch cell. The voltage profile of optimized hybrid solvating electrolyte using 0.25 C rate (1 C ≡ 120 mA g^{-1}) at different cycles, including 2nd, 10th, 50th, 100th cycle, respectively.

Microscopic and spectroscopic characterization of hybrid solvating electrolytes

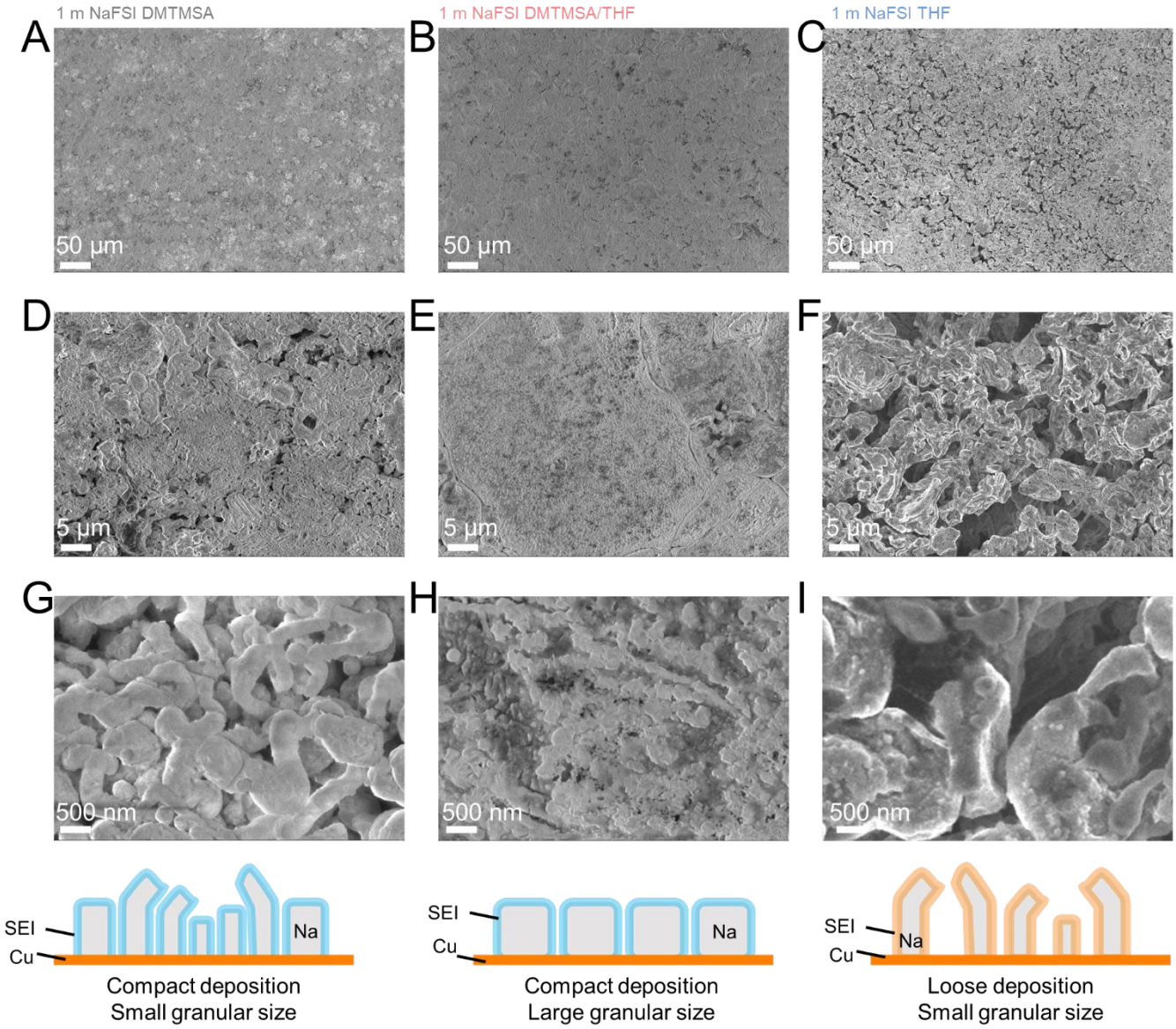

Figure S26. Top-view SEM images of Cu electrodes at plating stage after 200 cycles using different electrolytes.

(A, D, G) Weakly solvating electrolyte.

(B, E, H) Hybrid solvating electrolyte.

(C, F, I) Strongly solvating electrolyte. Same scale bars are used for each row for direct comparison.

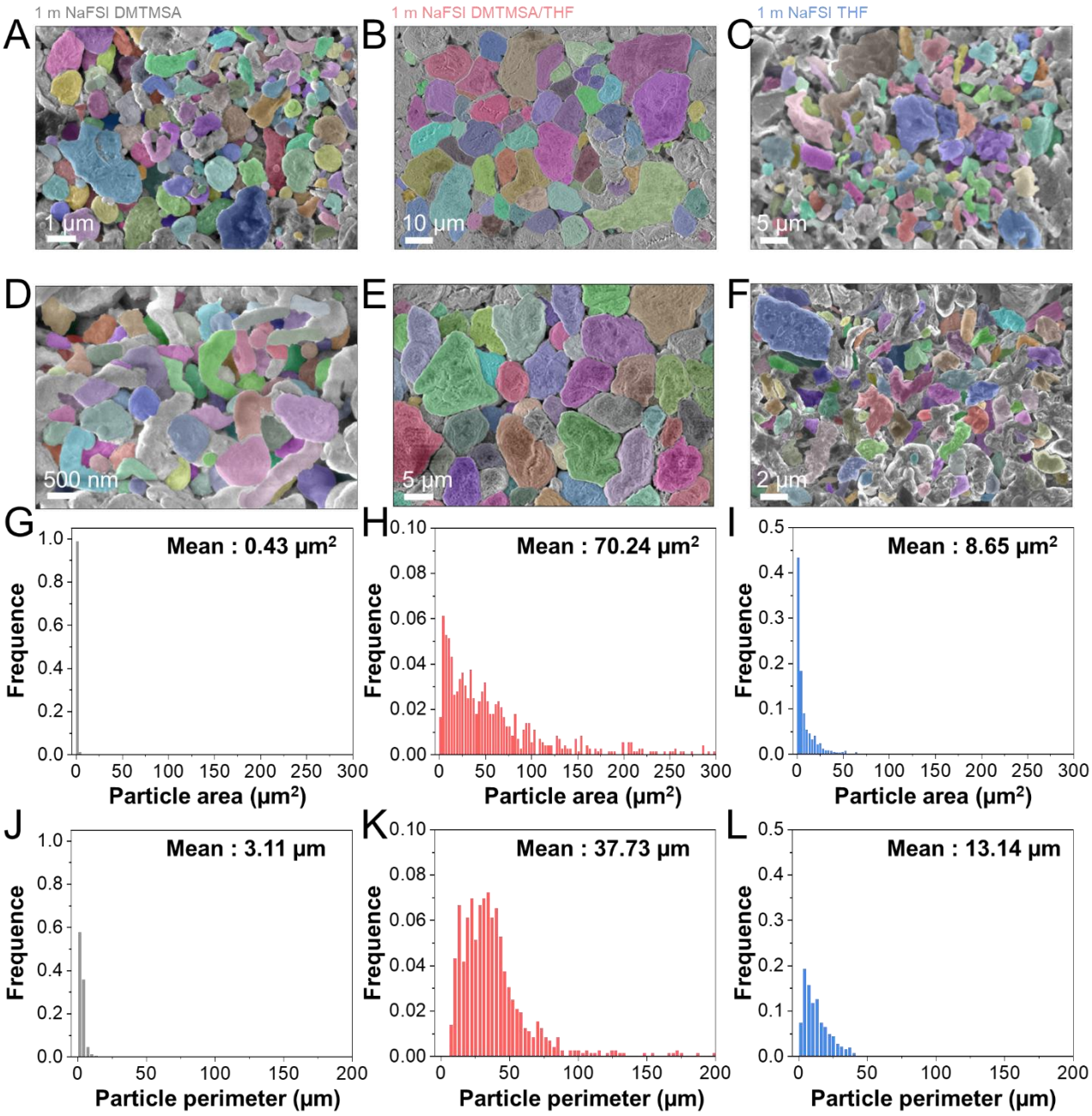

Figure S27. Electrochemically deposited Na^0 microparticles labeled using computer vision method.

(A, D) Weakly solvating electrolyte.

(B, E) hybrid solvating electrolyte.

(C, F) Strongly solvating electrolyte. Distinct color area is used to label and distinguish different Na metal microparticles electrochemically deposited on the Cu current collectors.

(G-L) Statistically results about the particle area and perimeter of labeled electrochemically deposited Na^0 microparticles.

(G, J) Weakly solvating electrolyte.

(H, K) hybrid solvating electrolyte.

(I, L) Strongly solvating electrolyte.

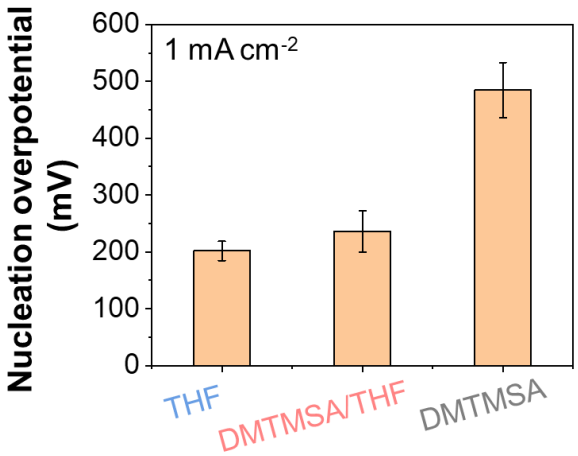

Figure S28. Nucleation overpotential using different electrolytes at 1.0 mA cm^{-2}.

"1 m NaFSI" DMTMSA, 1 m NaFSI DMTMSA/THF and 1 m NaFSI THF.

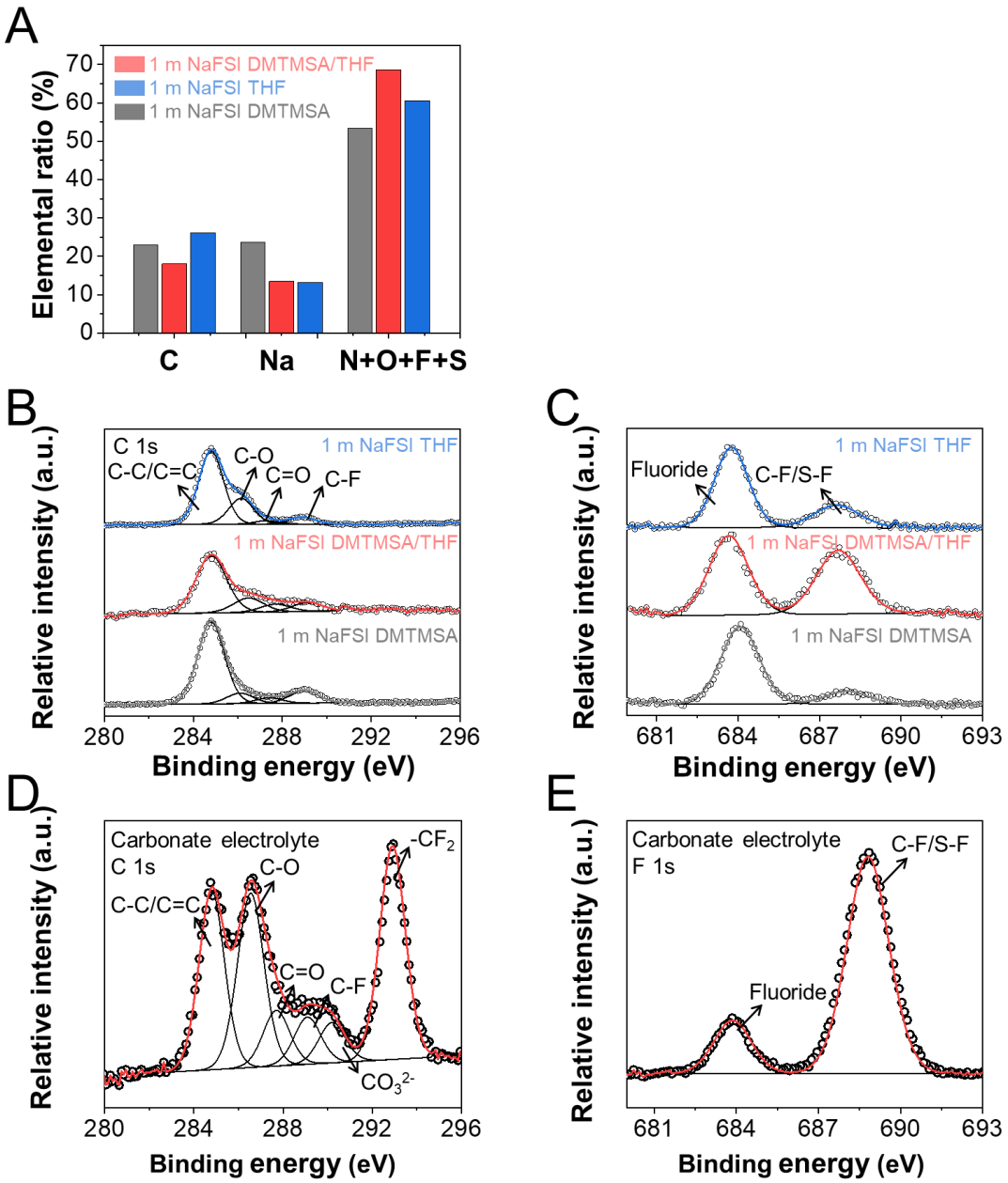

Figure S29. XPS analysis of Cu electrodes at plating stage after 200 cycles.

(A) The atomic ratios of various elements for Cu electrodes after 200 cycles using different electrolytes at plating stage.

(B-C) High resolution elemental analysis for Cu electrodes after 200 cycles using different electrolytes at plating stage. (B) C 1s. (C) F 1s.

(D-E) The analysis for Cu electrode after 200 cycles using commercial carbonate electrolytes.

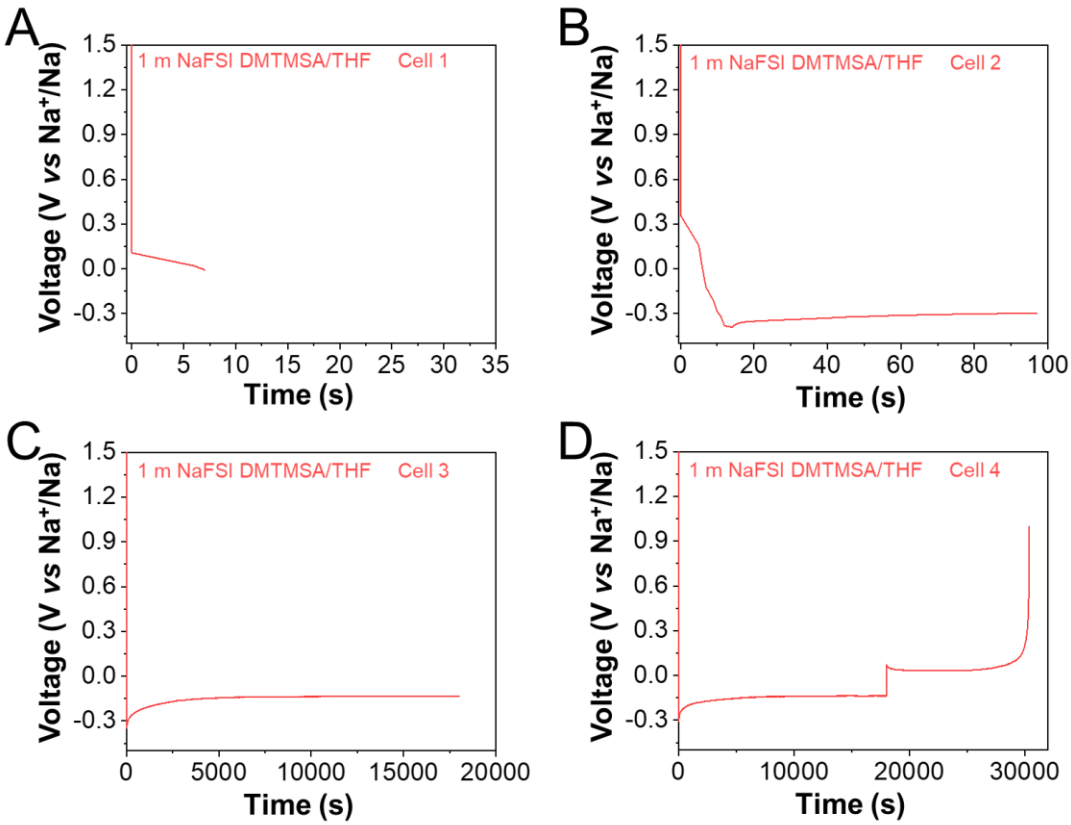

Figure S30. Voltage profiles using hybrid solvating electrolytes.

(A) Cell 1 was discharged until the voltage reached 0 V.

(B) Cell 2 was discharged until the voltage reached the minimal voltage.

(C) Cell 3 was discharged until 2.0 mAh cm^{-2} sodium metal was deposited.

(D) Cell 4 was discharged until 2.0 mAh cm^{-2} sodium metal was deposited and then charged until the voltage reached 1 V. The current densities 0.4 mA cm^{-2} for all of these 4 cells, which was the same as the current densities used for precycle in the normal cycle protocol.

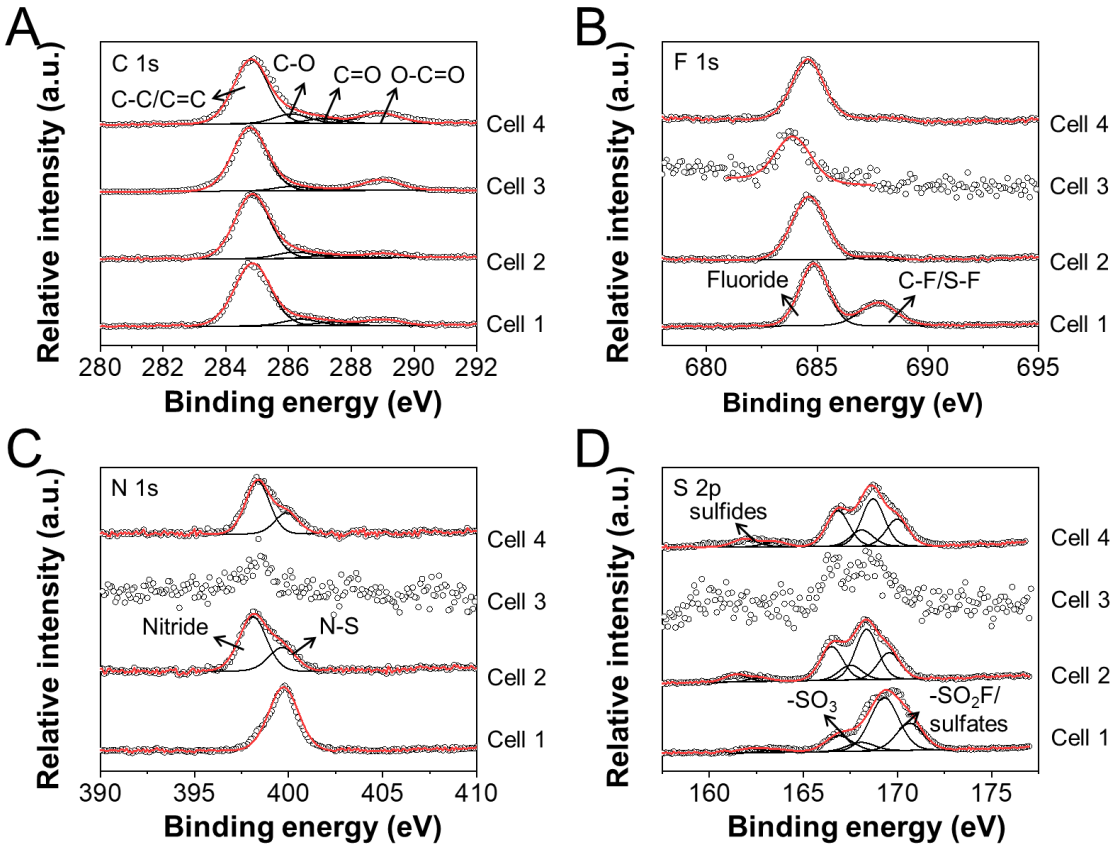

Figure S31. XPS analysis of Cu electrodes using hybrid solvating electrolytes.

(A) C 1s. (B) F 1s. (C) N 1s. (D) S 2p. Cell 1 was discharged until the voltage reached 0 V. Cell 2 was discharged until the voltage reached the minimal voltage. Cell 3 was discharged until 2.0 mAh cm^{-2} sodium metal was deposited. Cell 4 was first discharged with the areal capacity of 2.0 mAh cm^{-2} and then charged until the voltage reached 1 V.

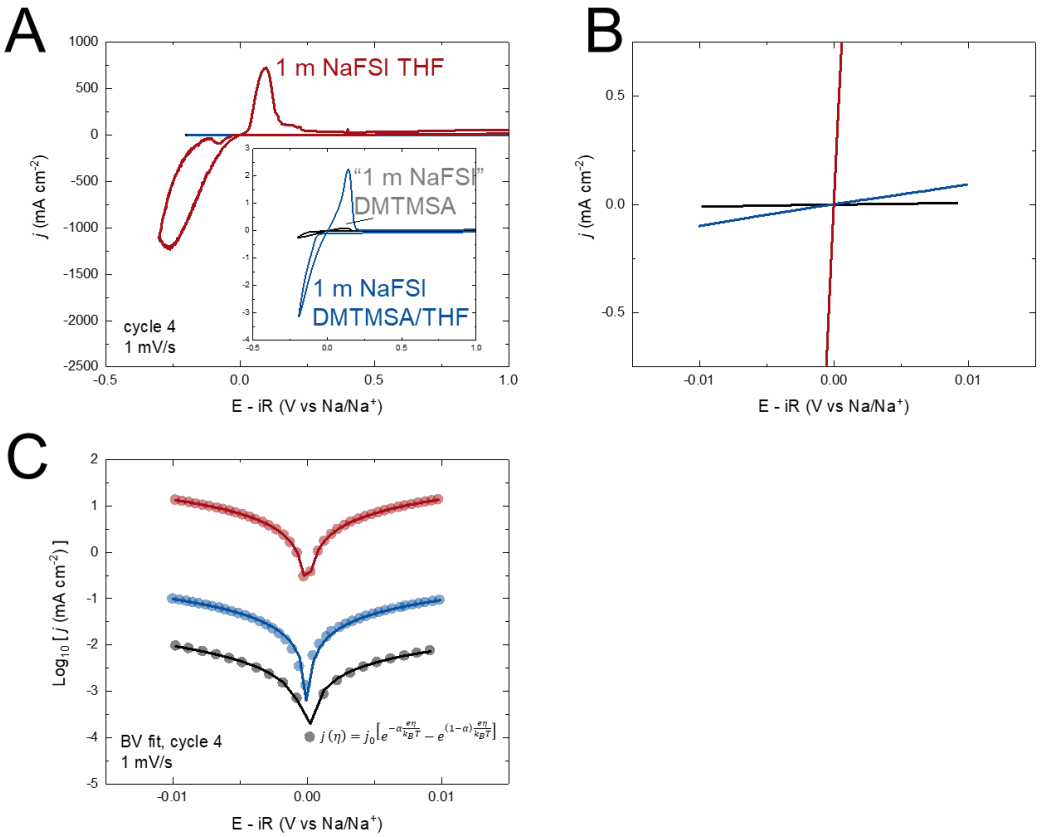

Figure S32. Kinetic analysis of hybrid solvating electrolytes.

(A) CV curves of different electrolytes scanned using 1 mV s^{-1}.

(B) The I-V response near the equilibrium potential.

(C) The Tafel plots of different electrolytes scanned using 1 mV s^{-1}.

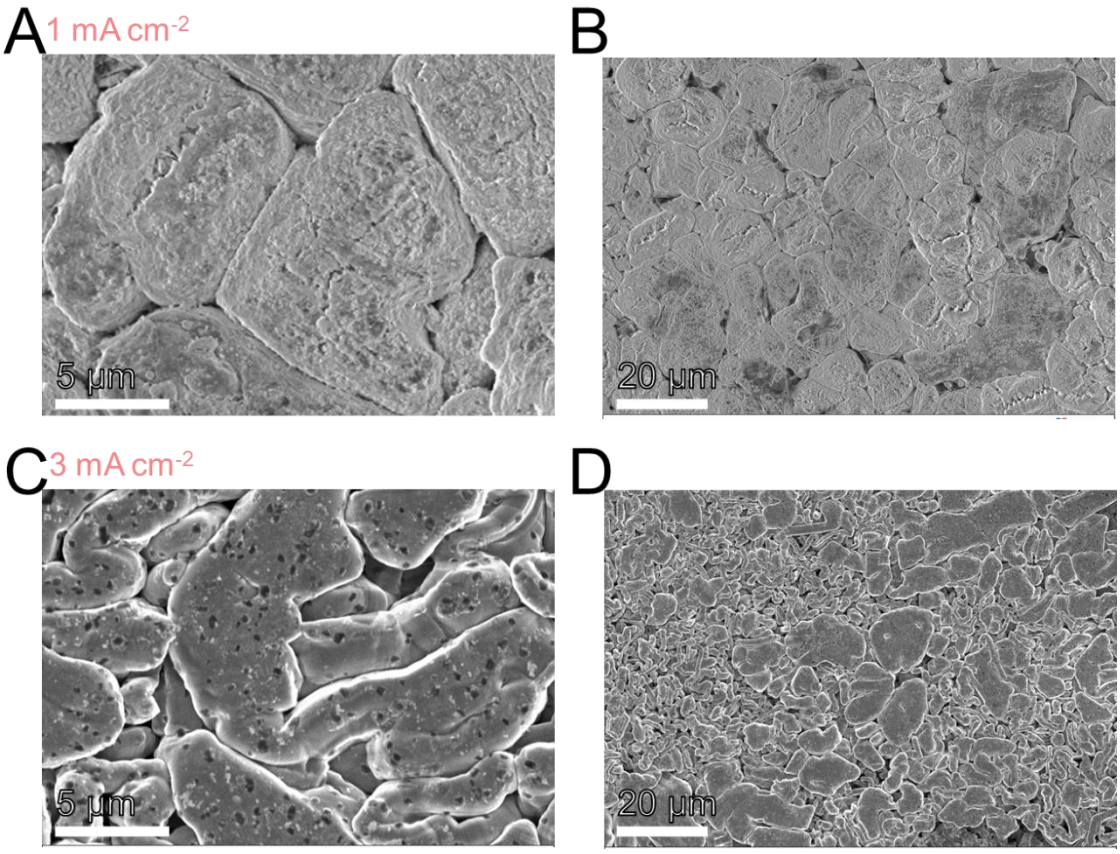

Figure S33. Top-view SEM images of Cu electrodes at plating stage using hybrid solvating electrolyte 1 m NaFSI DMTMSA/THF at different current densities.

(A-B) 1 mA cm^{-2}. (C-D) 3 mA cm^{-2}.

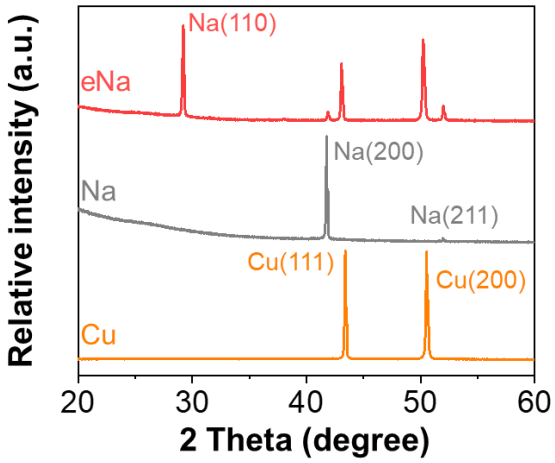

Figure S34. The XRD results.

Na electrochemically deposited on Cu using 1 m NaFSI DMTMSA/THF (eNa, red line), pristine Na (Na, gray line) and Cu (orange line).

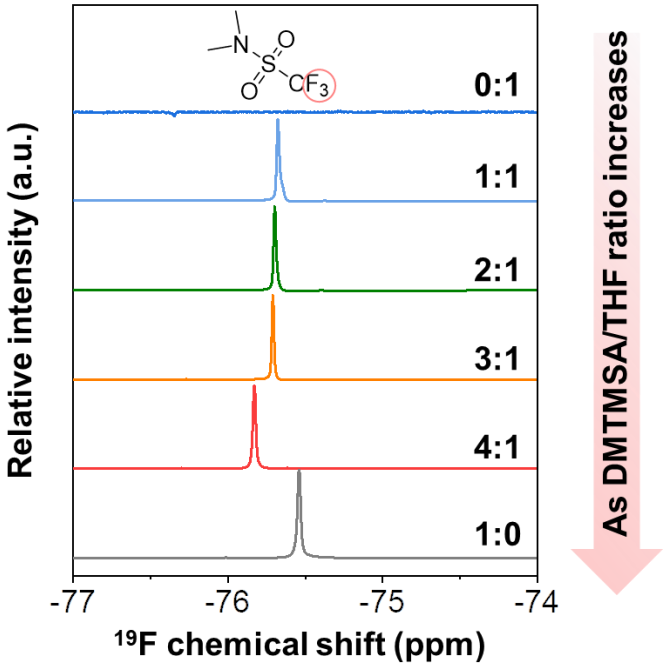

Figure S35. ^{19}F NMR results of different hybrid solvating electrolytes.

The ratio indicates the molar ratio between DMTMSA and THF.

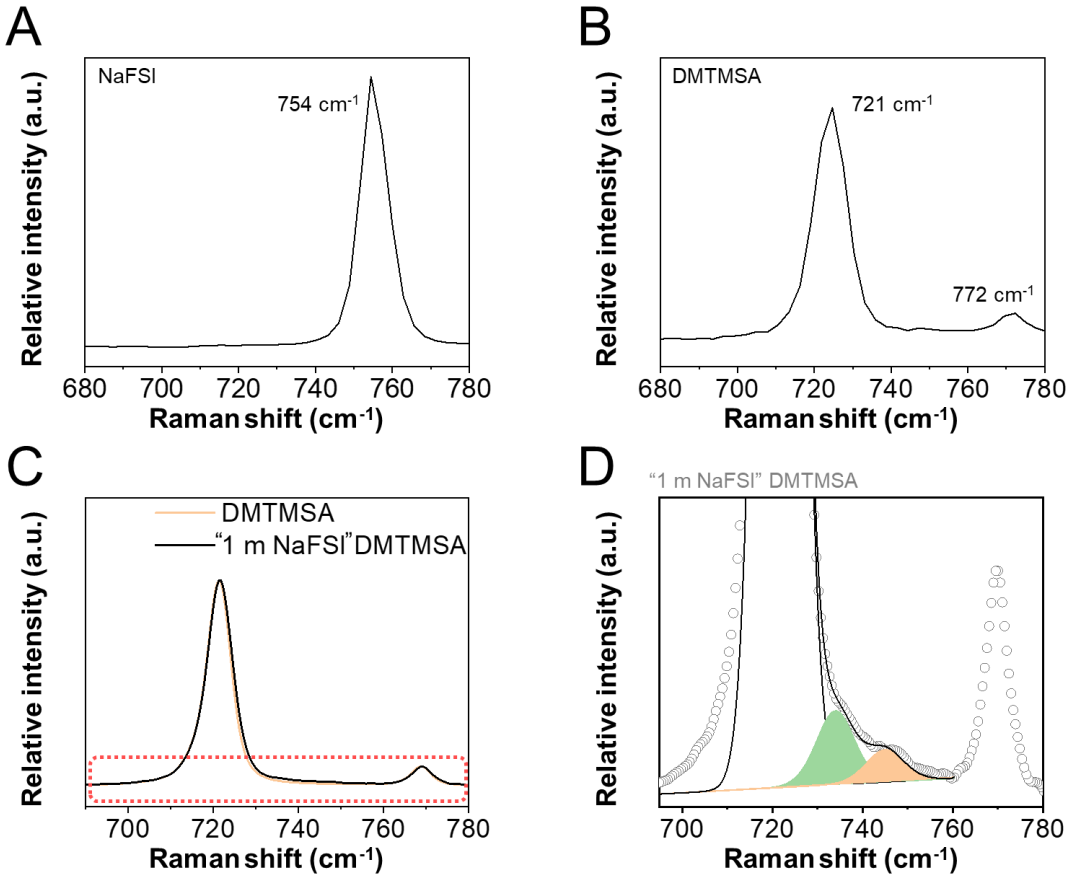

Figure S36. Raman results.

(A) NaFSI salts. (B) Pure DMTMSA solvent. (C-D) weakly solvating electrolyte 1 m NaFSI using DMTMSA as the only solvent. There are two Raman peaks for DMTMSA at ~721 and ~772 cm^{-1}, respectively. The characterization above is carried out using the clear supernatant of the electrolyte. the same for FTIR characterization below. The solubility limitation of NaFSI salt within DMTMSA is measured as ~0.19 m. Therefore, there is a very low signal for CIP and AGG.

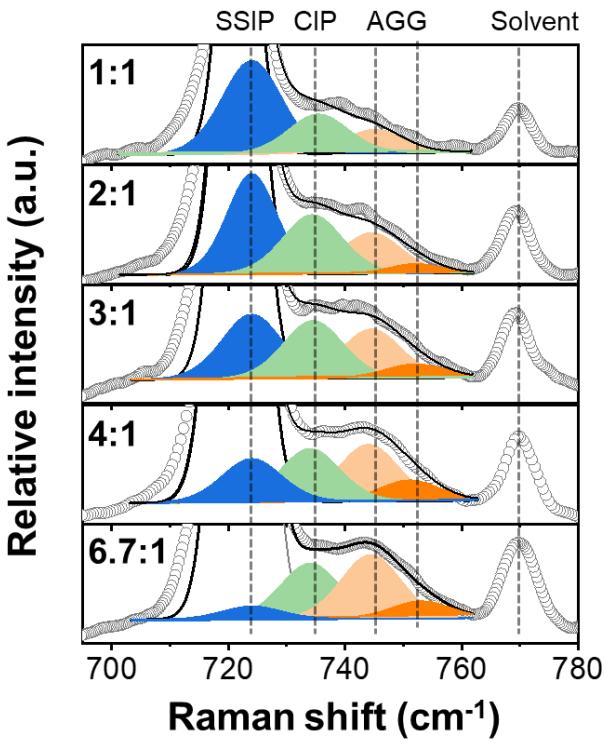

Figure S37. Raman results of different hybrid solvating electrolytes.

The values are the molar ratios between DMTMSA and THF solvents for different hybrid solvating electrolytes. The salt is NaFSI.

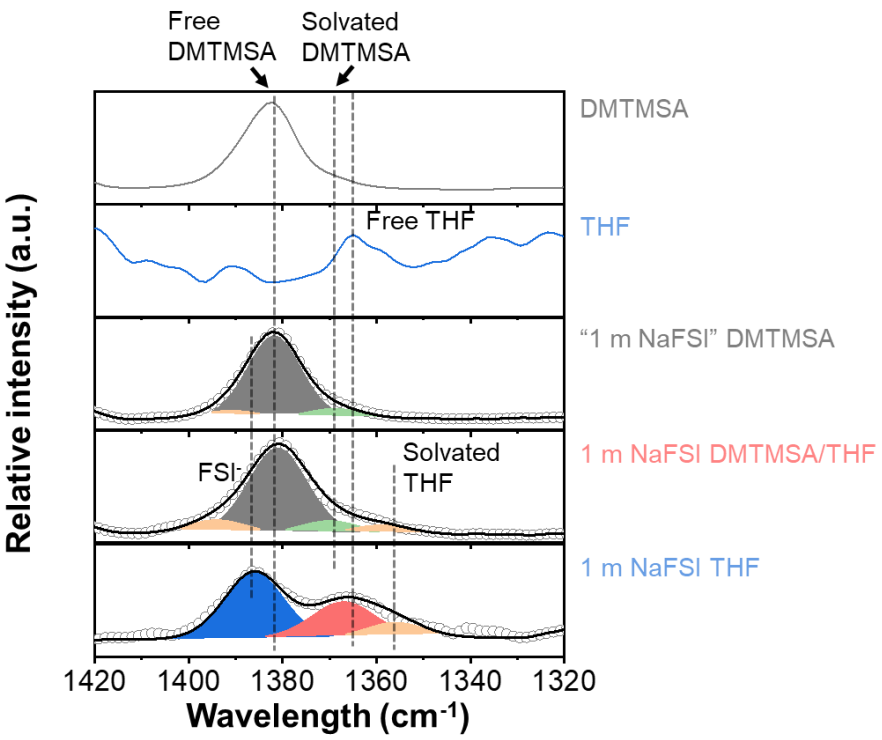

Figure S38. FTIR results of various electrolytes and solvents.

DMTMSA, THF, "1 m NaFSI" DMTMSA, 1 m NaFSI DMTMSA/THF and 1 m NaFSI THF.

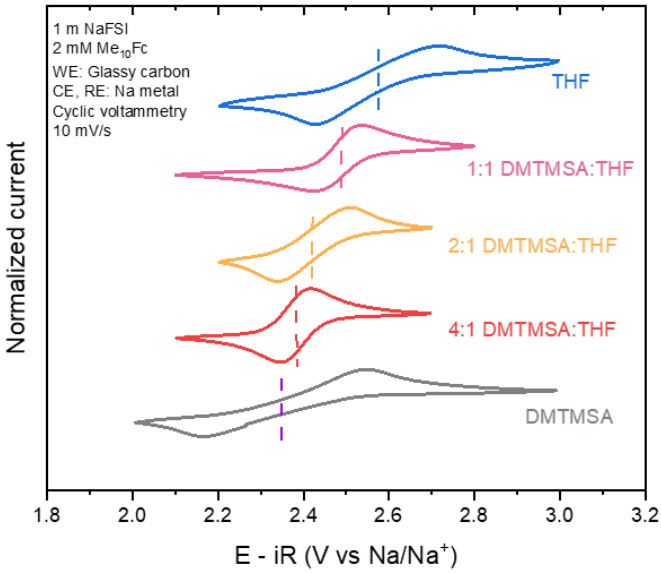

Figure S39. Redox potentials of different hybrid solvating electrolytes.

Cyclic voltammograms of $Me_{10}Fc$ in the given electrolytes The values are the molar ratios between DMTMSA and THF solvents for different hybrid solvating electrolytes. The salt is NaFSI.

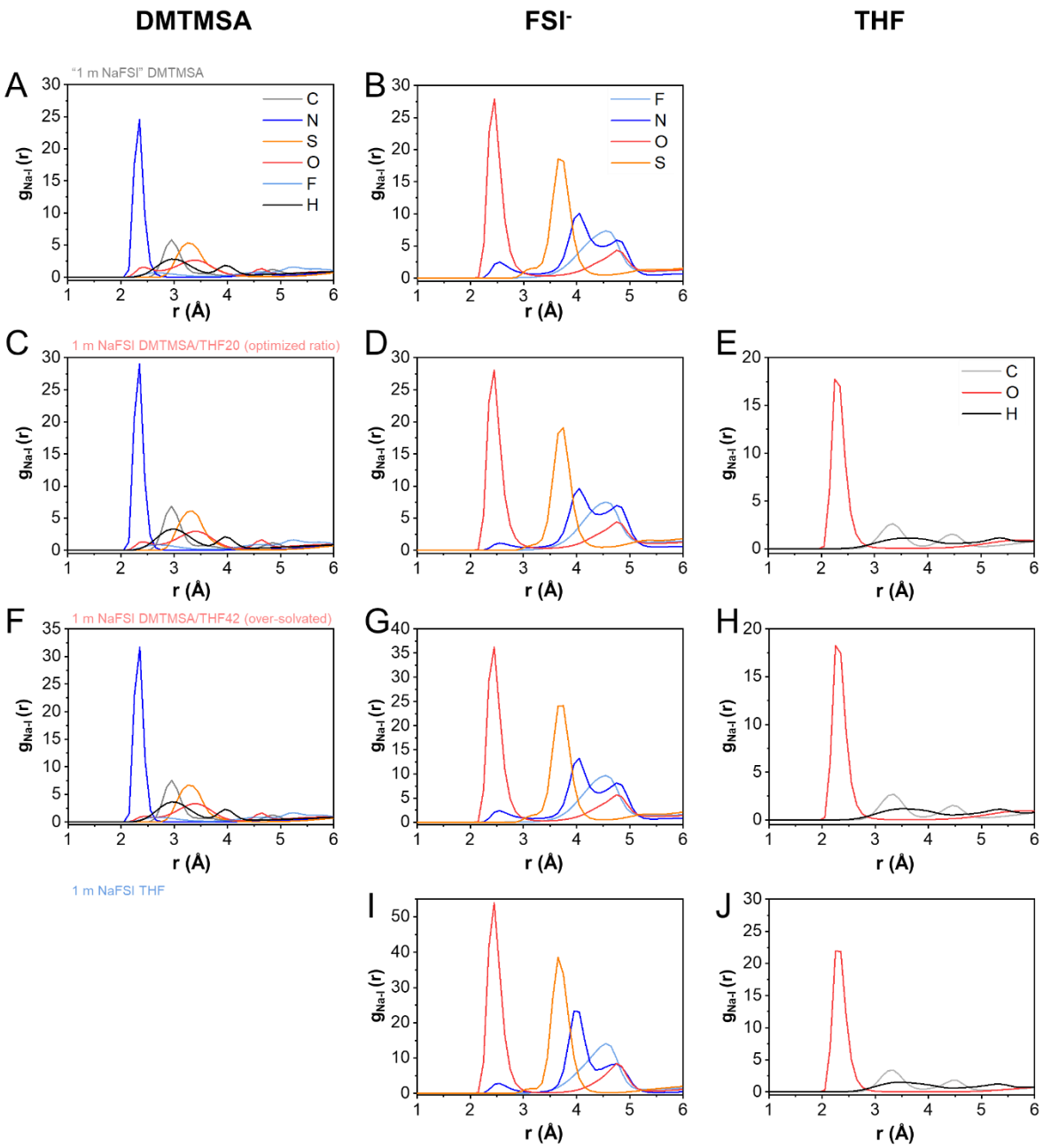

Figure S40. Radial distribution function of anion and solvents for various electrolytes.

(A-B) **"**1 m NaFSI" DMTMSA electrolyte**.**

(C-E) 1 m NaFSI DMTMSA/THF20 electrolyte (optimal ratio)**.**

(F-H) 1 m NaFSI DMTMSA/THF42 electrolyte (over solvated)**.**

(I-J) 1 m NaFSI THF electrolyte**.** The same color lines are used to label the same atom distribution in the graphs.

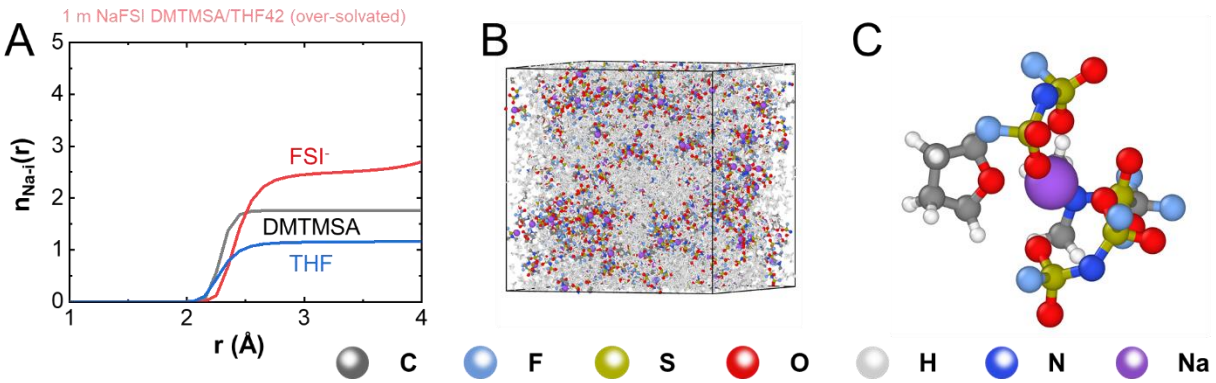

Figure S41. Simulated coordination structures of hybrid solvating electrolyte.

(A) Coordination structures.

(B) Molecular snapshots.

(C) Schematic solvation structure of 1 m NaFSI DMTMSA/THF42 electrolyte.

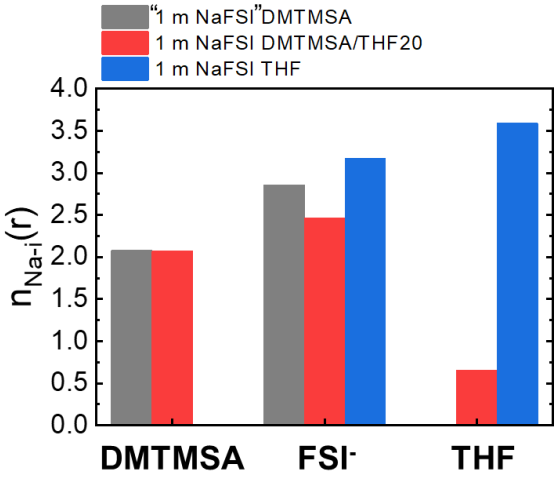

Figure. S42. Simulated coordination numbers of different electrolytes.

"1 m NaFSI" DMTMSA, 1 m NaFSI DMTMSA/THF and 1 m NaFSI THF.

Generalized strategy for hybrid solvating electrolytes

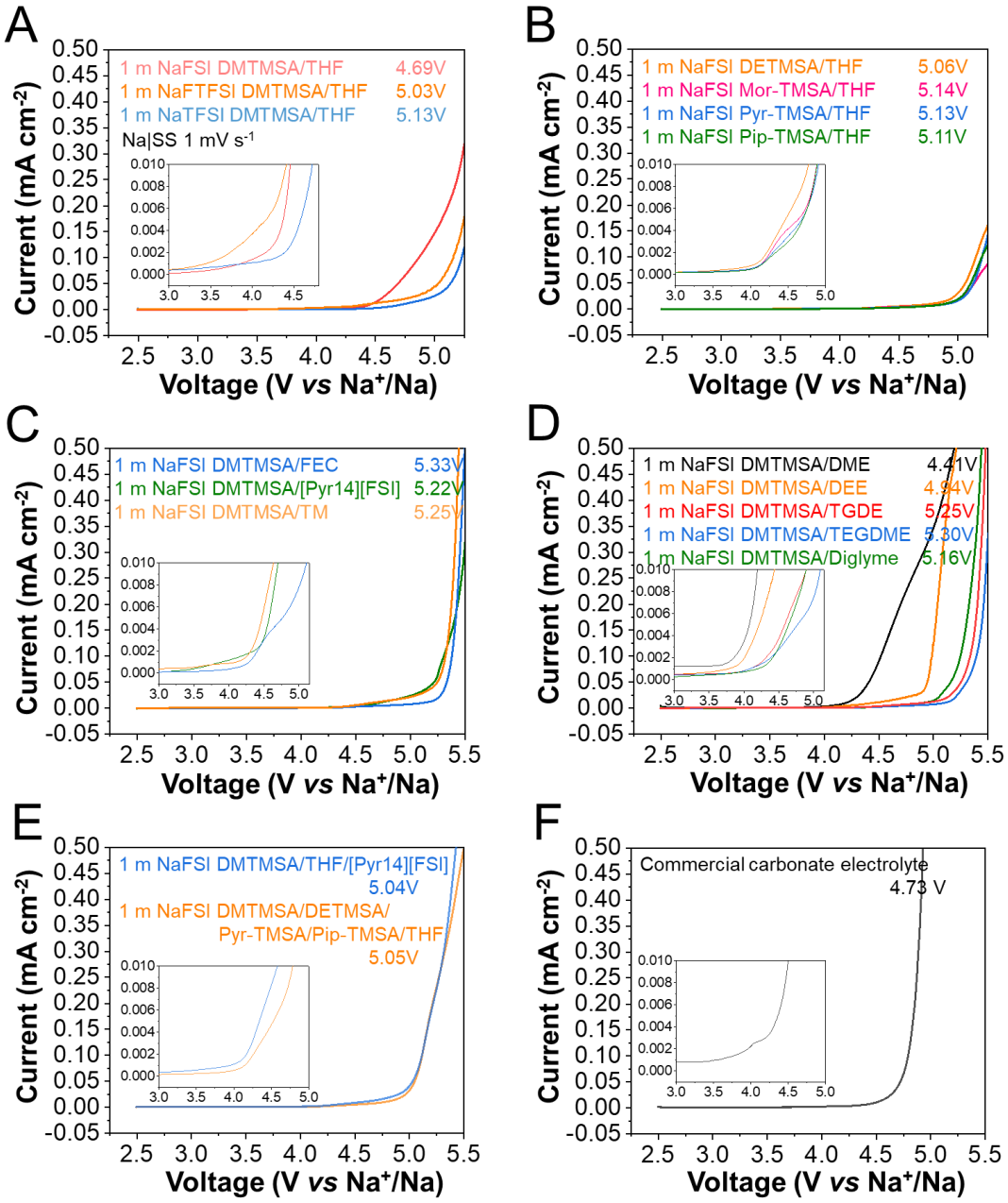

Figure S43. Oxidative stability of various hybrid solvating electrolytes.

(A-C) Hybrid solvating electrolytes with (A) different sodium salts, (B) different fluorinated sulfonate-based weakly solvating solvents, and (C) different types of strong solvating co-solvents, including fluorinated carbonate, and partially fluorinated sulfonates.

(D) Hybrid solvating electrolytes with different types of acyclic ether-based strong solvating co-solvents.

(E) Hybrid solvating electrolytes with different strong and weak solvating electrolyte mixtures.

(F) Commercial carbonate electrolytes. The oxidation stability of various electrolytes was tested using Na||SS half cells with scanning rate of 1 mV s^{-1}. SS, stainless steel. The values show the voltages when the current reached 0.05 mA cm^{-2}.

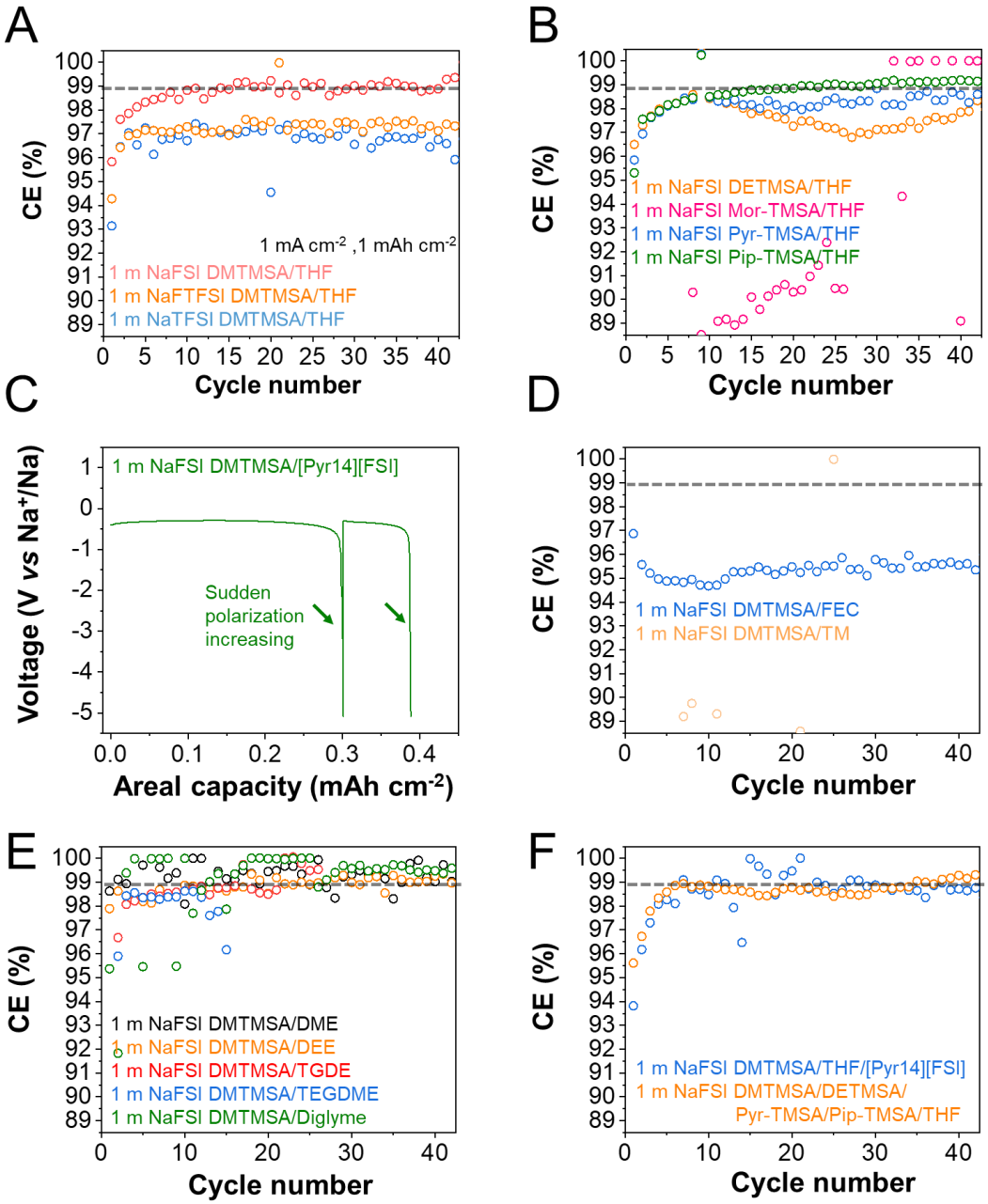

Figure S44. Na^0 cycling stability of various electrolytes.

Hybrid solvating electrolytes with (A) different sodium salts, (B) different fluorinated sulfonate-based weakly solvating solvents, (C-E) different types of strong solvating co-solvents, including fluorinated carbonate, acyclic ether, and partially fluorinated sulfonates, (F) different strong and weak solvating electrolyte mixtures.

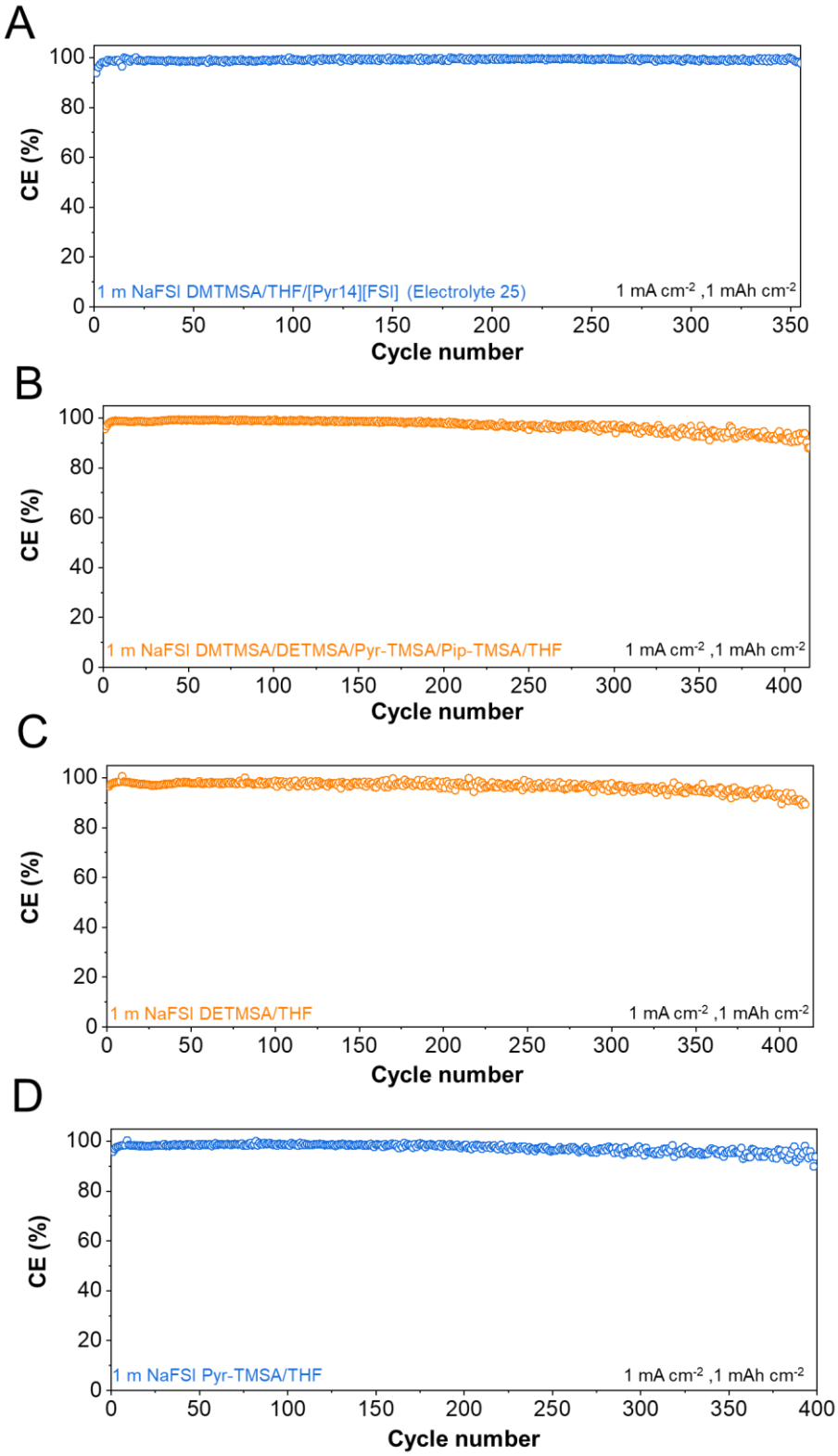
A
CE (%)
Cycle number
1 m NaFSI DMTMSA/THF/[Pyr14][FSI] (Electrolyte 25)
1 mA cm-2 ,1 mAh cm-2
B
CE (%)
Cycle number
1 m NaFSI DMTMSA/DETMSA/Pyr-TMSA/Pip-TMSA/THF
1 mA cm-2 ,1 mAh cm-2
C
CE (%)
Cycle number
1 m NaFSI DETMSA/THF
1 mA cm-2 ,1 mAh cm-2
D
CE (%)
Cycle number
1 m NaFSI Pyr-TMSA/THF
1 mA cm-2 ,1 mAh cm-2

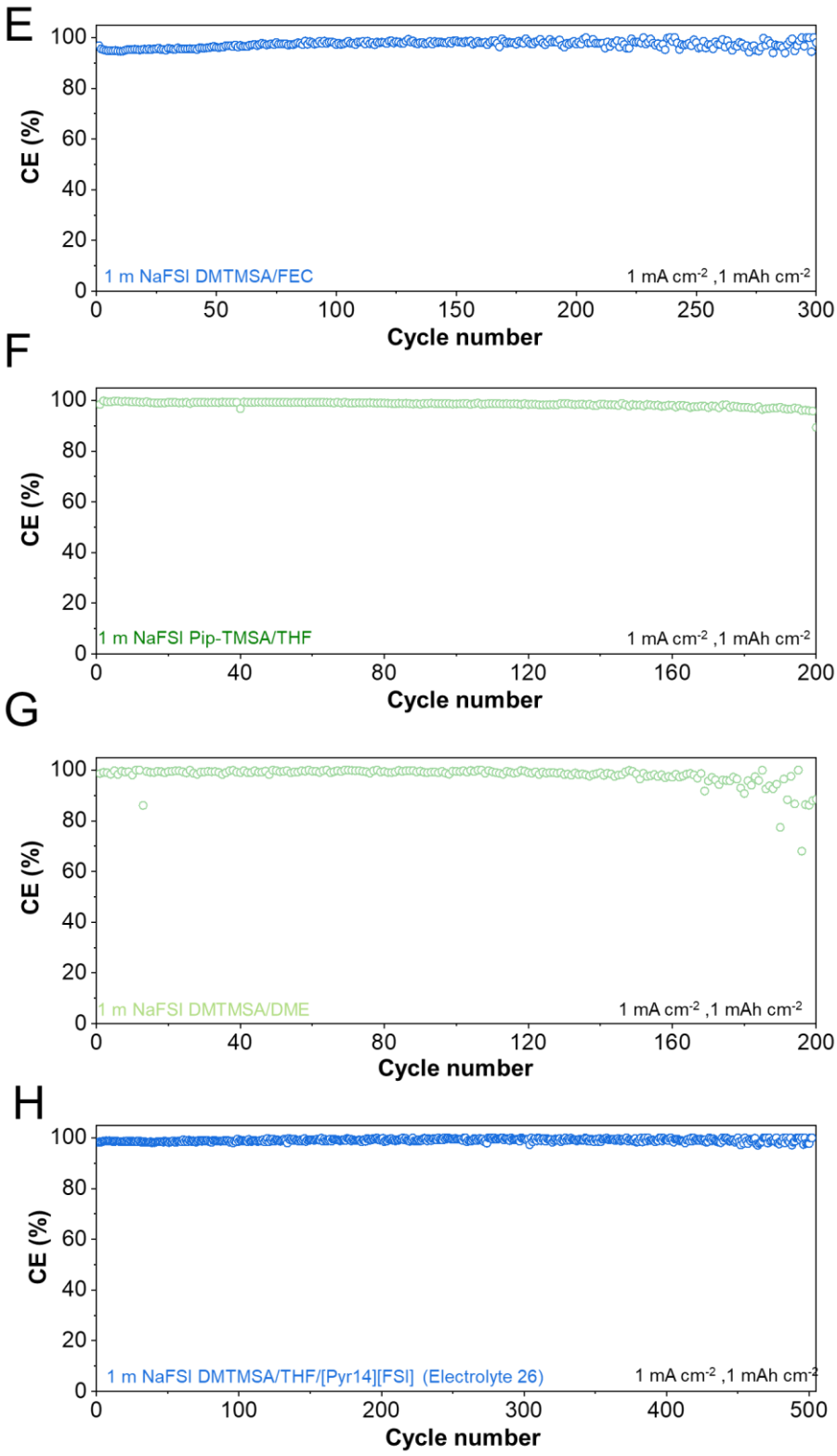
E
CE (%)
1 m NaFSI DMTMSA/FEC
1 mA cm-2 ,1 mAh cm-2
Cycle number
F
CE (%)
1 m NaFSI Pip-TMSA/THF
1 mA cm-2 ,1 mAh cm-2
Cycle number
G
CE (%)
1 m NaFSI DMTMSA/DME
1 mA cm-2 ,1 mAh cm-2
Cycle number
H
CE (%)
1 m NaFSI DMTMSA/THF/[Pyr14][FSI] (Electrolyte 26)
1 mA cm-2 ,1 mAh cm-2
Cycle number

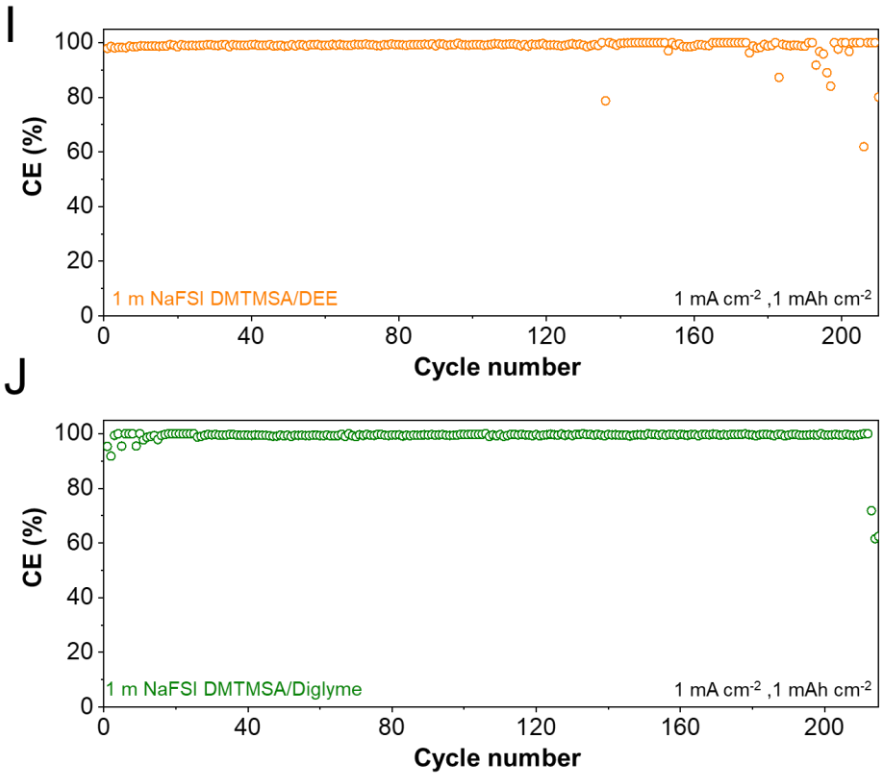

Figure S45. Na^0 cycling stability of various hybrid solvating electrolytes.

(A) 1 m NaFSI DMTMSA/THF/[Pyr14][FSI] (electrolyte 25).

(B) 1 m NaFSI DMTMSA/DETMSA/Pyr-TMSA/Pip-TMSA/THF.

(C) 1 m NaFSI DETMSA/THF.

(D) 1 m NaFSI Pyr-TMSA/THF.

(E) 1 m NaFSI DMTMSA/FEC.

(F) 1 m NaFSI Pip-TMSA/THF.

(G) 1 m NaFSI Pip-TMSA/DME.

(H) 1 m NaFSI DMTMSA/THF/[Pyr14][FSI] (electrolyte 26).

(I) 1 m NaFSI DMTMSA/DEE.

(J) 1 m NaFSI DMTMSA/Diglyme.

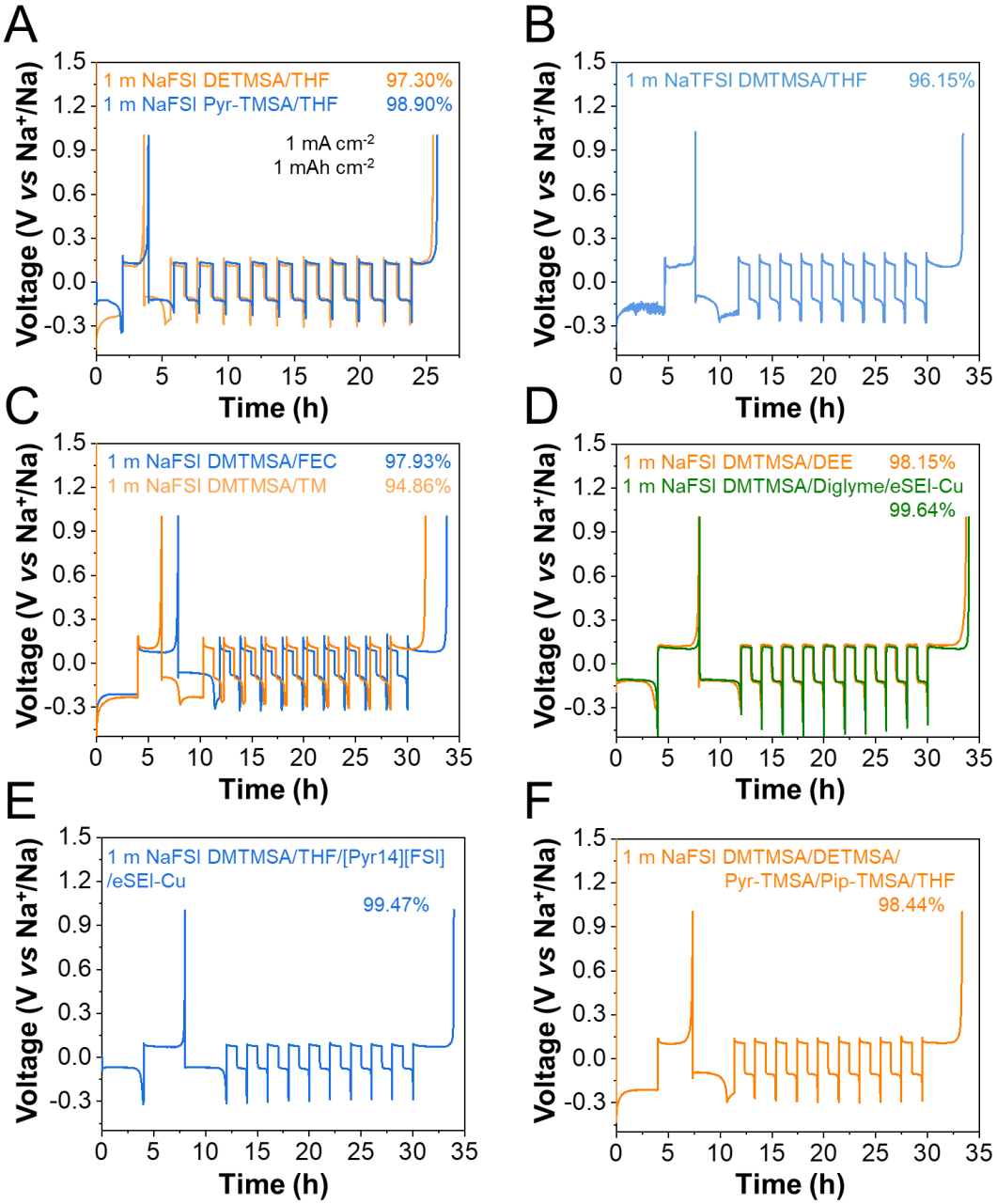

Figure S46. Na^0 cycling stability of various hybrid solvating electrolytes.

The Aurbach method measurement of Na^0 coulombic efficiency in Na||Cu half cells using different electrolytes.

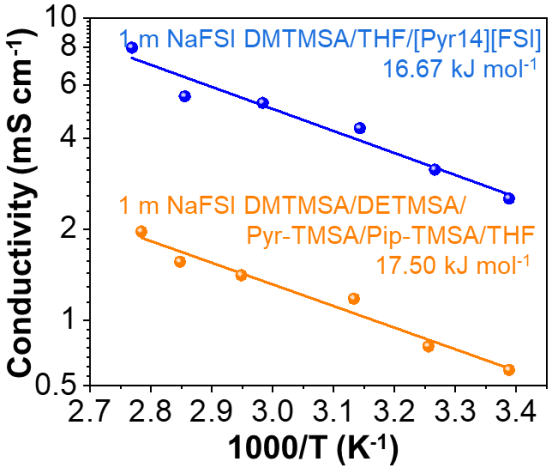

Figure S47. Ionic conductivity of different electrolytes under various temperatures. 1 m NaFSI DMTMSA/DETMSA/Pyr-TMSA/Pip-TMSA/THF (orange) and 1 m NaFSI DMTMSA/THF/[Pyr14][FSI] (electrolyte 25, blue).

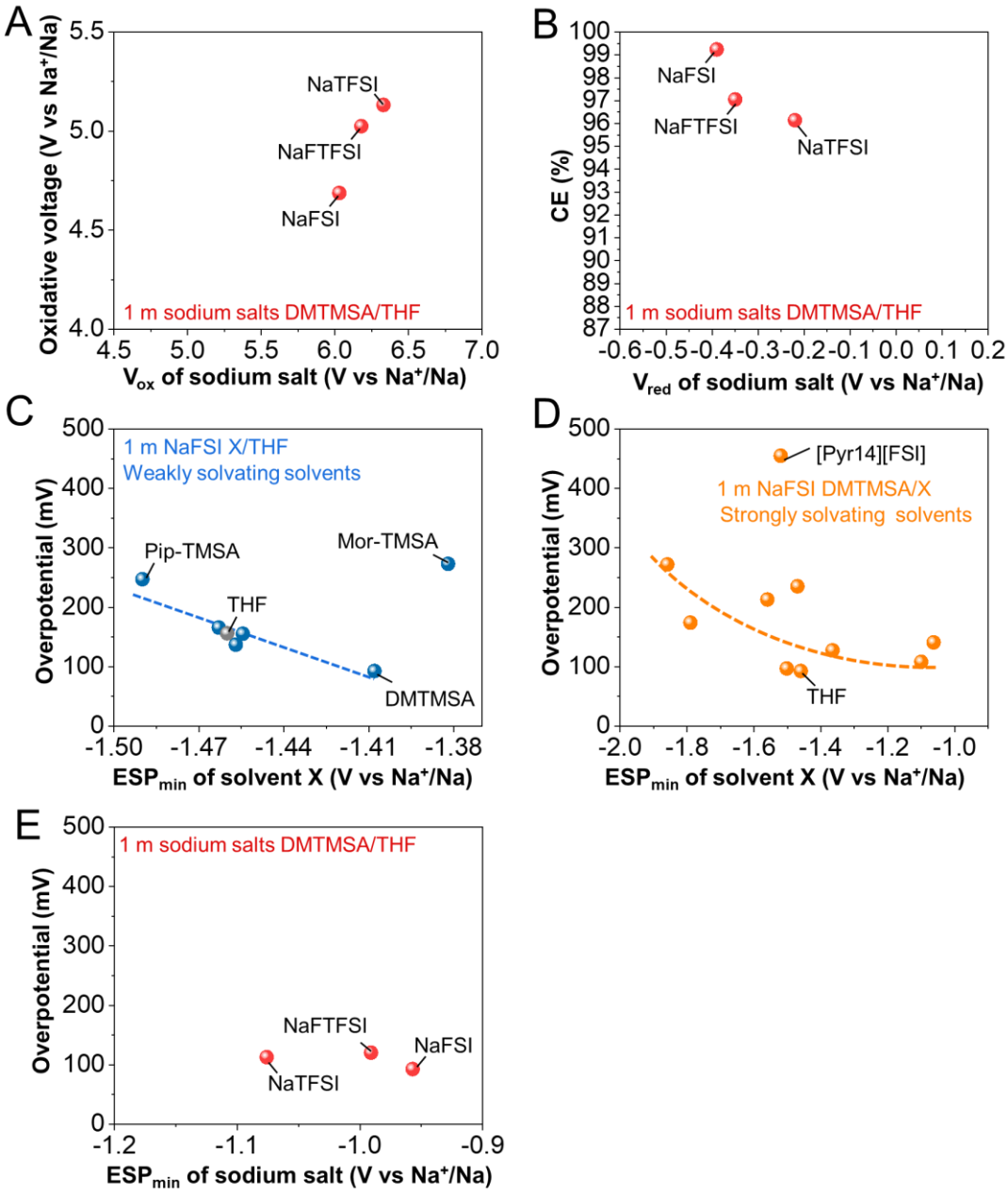

Figure S48. Salts and solvents selection for hybrid solvating electrolytes.

(A) The relationship between V_{ox} of sodium salts and the oxidative voltage of the HSEs.

(B) The relationship between V_{red} of sodium salts and the CE of the HSEs.

(C-E) The relationship between ESP_{min} of (C) weak solvents or (D) strong solvents or (E) sodium salts and the cycling overpotential of HSEs.

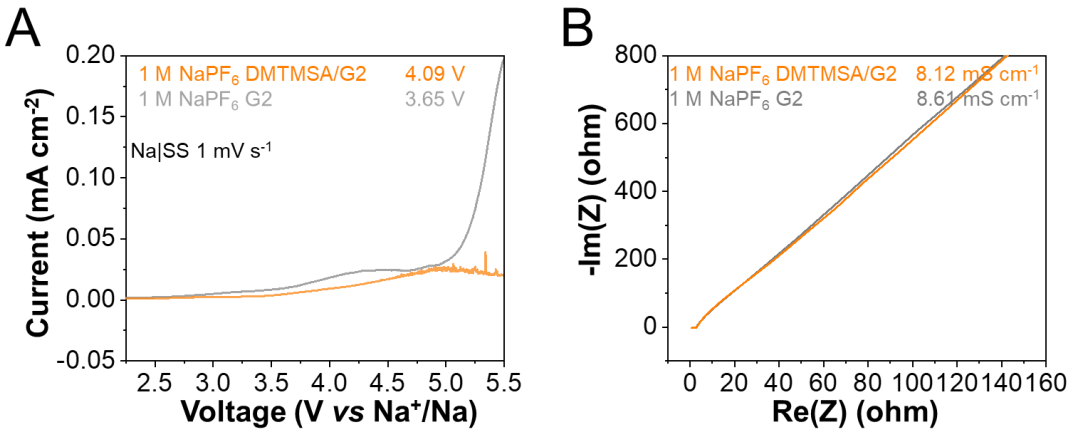

Figure S49. Electrochemical properties of representative HSE.

(A) Oxidative stability of 1 M $NaPF_6$ DMTMSA/diglyme and 1 M $NaPF_6$ diglyme electrolytes.

(B) Electrochemical impedance spectroscopy results.

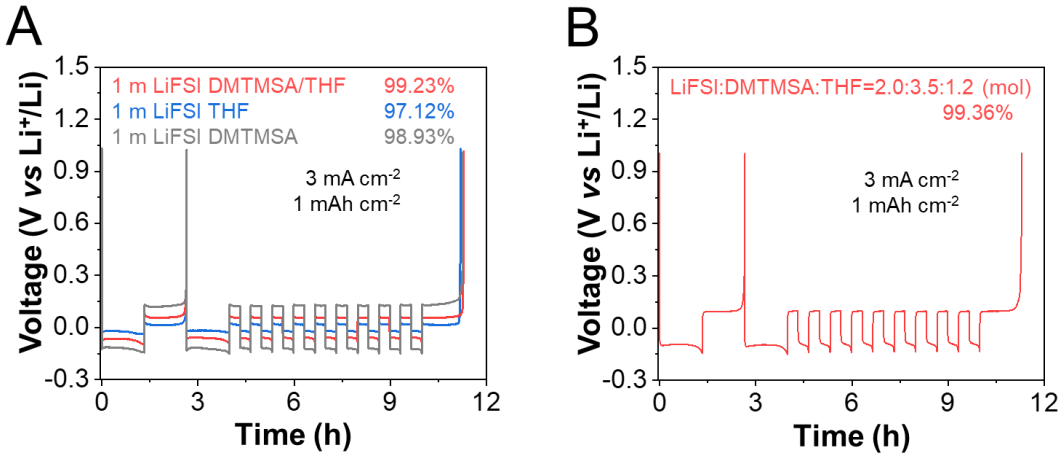

Figure S50. Electrochemical performance of HSEs in lithium metal battery.

(A) Aurbach method measurement of Li^0 coulombic efficiency in Li||Cu half cells using different electrolytes.

(B) Aurbach method measurement of Li^0 coulombic efficiency using hybrid solvating electrolyte and precycled Cu with stable SEI.

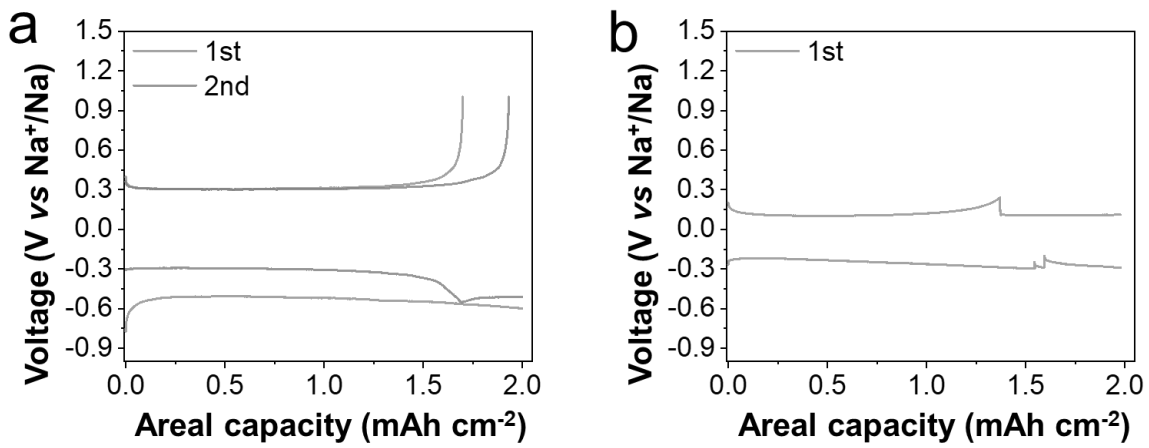

Figure S51. Electrochemical performance using 1 m NaFSI DMTMSA electrolyte.

(A) Supernatant of 1 m NaFSI DMTMSA.

(B) 1 m NaFSI DMTMSA whole suspension at 0.4 mA cm^{-2} with the areal capacity of 2.0 mAh cm^{-2}. Due to the weak solvating properties of DMTMSA, the solubility limitation of NaFSI salt within DMTMSA is measured as ~0.19 m. Here, "1 m NaFSI DMTMSA" means that the electrolyte is prepared by mixing 1 mmol NaFSI and 1 g DMTMSA until reaching the solubility limitation. Based on the above results, the supernatant of 1 m NaFSI DMTMSA is used for electrochemical tests and other characterizations. And it is called "1 m NaFSI DMTMSA" throughout the manuscript. 1 mmol NaFSI can be fully dissolved when the molar ratio between DMTMSA and THF exceeds 5.3:1.

Table S1 The properties of various solvents and sodium salts

No.	Name	Donor number (kcal mol^{-1})	Solvent accessible surface area ($Å^2$)	Polar area ratio	ESP_{min} (eV)	ESP_{max} (eV)
Salts						
1	NaFSI	13.43	132.02	0.62	-0.96	1.78
2	NaTFSI	13.31	200.00	0.41	-1.08	2.74
3	NaFTFSI	12.61	165.10	0.50	-0.99	2.38
4	$NaPF_6$	17.68	77.61	/	/	/
Solvents						
5	DCE	0.30	103.96	0.00	-0.37	0.81
6	Toluene	0.34	154.36	0.00	-0.81	0.38
7	TTE	2.04	206.90	0.04	-0.58	1.71
8	p-Xylene	5.37	180.76	0.00	-0.85	0.34
9	HFE	5.96	173.76	0.05	-0.46	1.04
10	$PhCF_3$	6.78	161.78	0.00	-0.54	0.68
11	TFEO	7.25	283.94	0.10	-0.83	1.66
12	BTFEC	7.65	213.04	0.17	-0.76	0.97
13	TTFM	7.74	189.06	0.23	-0.81	1.23
14	BTFE	9.09	172.74	0.05	-0.80	1.42
15	C_7F_{14}	9.44	244.34	0.00	-0.08	0.94
16	TM	9.59	181.53	0.24	-1.47	1.84
17	Mor-TMSA	11.85	226.39	0.21	-1.38	1.12
18	Pip-TMSA	11.87	245.36	0.15	-1.49	0.84
19	Pyr-TMSA	12.63	219.01	0.17	-1.46	0.94
20	DMTMSA	12.96	184.67	0.20	-1.41	1.13
21	DETMSA	13.65	235.60	0.16	-1.46	1.05
22	Me-THF	12.41	158.14	0.06	-1.24	0.41
23	Cl-DEE	12.90	232.55	0.08	-2.12	0.79

No.	Name	Donor number (kcal mol^{-1})	Solvent accessible surface area (Å^2)	Polar area ratio	ESP_{min} (eV)	ESP_{max} (eV)
24	[Pyr14][FSI]	14.62	237.37	0.35	-1.52	2.75
25	TMS	14.74	163.00	0.21	-2.05	1.19
26	FEC	15.97	111.14	0.32	-1.37	1.70
27	VC	16.01	90.27	0.48	-1.55	1.46
28	EC	16.43	107.87	0.33	-1.53	1.48
29	DMC	16.71	138.15	0.26	-1.44 (ref. 41)	0.77 (ref. 41)
30	EMC	16.80	164.98	0.22	-1.48 (ref. 41)	0.75 (ref. 41)
31	VEC	17.11	147.94	0.24	-1.56	1.33
32	PS	17.13	144.58	0.30	-1.77	1.49
33	DTD	17.38	127.39	0.41	-1.44	1.79
34	TEGDME	18.59	351.86	0.13	-1.56	0.83
35	THF	19.84	130.23	0.07	-1.46 (ref. 41)	0.52 (ref. 41)
36	DME	19.96	160.03	0.12	-1.86	0.50
37	TGDE	21.05	286.86	0.13	-1.79	0.61
38	DEGDEE	21.19	275.76	0.10	-1.63	0.51
39	DEGDBE	22.52	385.18	0.07	-1.90	0.67
40	TEP	25.95	274.33	0.16	-1.74	0.69

Table S2 Electrochemical performance of Na||Cu cells

Electrolyte	Current density (mA cm^{-2})	Areal capacity (mAh cm^{-2})	Activation cycle number (>99.0%)	CE	Cycling overpotential (mV)	Ref.
1 m NaFSI DMTMSA/THF	1.0	1.0	10	99.72%	75	This work
	1.0	3.0	2	99.25%	75	This work
	3.0	1.0	5	99.40%	230	This work
1 m NaFSI DMTMSA/Diglyme	1.0	1.0	12	99.64%	110	This work
1.1 M NaFSI + 0.3 M $NaNO_3$ TMP	1.0	1.0	/	~99%	~20	13
1.5 M NaFSI DME:BTFE=1:3 (mol)	1.0	1.0	>30	~99%	~170	31
2.1 M NaFSI DME:BTFE=1:2 (mol)	1.0	1.0	>30	98.95%	~145	31
2.3 M NaFSI DME:TTE=1:1 (mol)	1.0	1.0	N/A	~98%	/	31
5.2 M NaFSI DME	1.0	1.0	N/A	~98%	~230	31
4.0 M NaFSI DME	1.0	1.0	>30	~99%	~130	1
NaFSI:THF=1:2 (mol)	0.5	0.5	>20	~99%	/	1
1.0 M $NaPF_6$ Diglyme	0.5	1.0	/	99.9%	~15	7
	1.0	1.0	N/A	91.22% (Cu)	~35 (Cu)	8
	1.0	1.0	N/A	98.66% (Sn)	~20 (Sn)	8
	1.0	1.0	~10	99.41% (Au)	~20 (Au)	8
	1.0	1.0	N/A	70% (Cu)	16 (Cu)	52
	1.0	1.0	/	99.9% (SF-Cu)	20 (SF-Cu)	52
	3.0	1.0	/	99.2% (COF-Cu)	/	25
1.0 M $NaPF_6$ FEC:FEMC=1:1 (vol) 0.3 wt% LiDFOB	0.5	1.0	N/A	98.42%	~75	53
2.0 M NaOTf + 0.08 M $Bi(OTf)_3$ + 0.4 M DTD DME	0.5	0.5	~8	99.1%	~32	54
NaFSI:Diglyme:HFME =1:1.17:3.82 (mol)	0.5	0.5	N/A	97.1%	~104	43
	0.5	1.0	N/A	95.9%	/	43
1.0 M $NaPF_6$ Diglyme: Me-THF=1:1 (vol)	0.5	1.0	/	99.74%	~22	55

Note:

1. “~” indicates that the values are estimated based on the graphs in the reference.
2. “/” indicates that the values are hard to distinguish.
3. “N/A” indicates that the CE never exceeds 99.0% and the activation cycle number is not applicable here.
4. The default working electrode is Cu foil unless otherwise specified.

Table S3 Electrochemical performance of sodium metal batteries

Electrode	Electrolyte	Current density (mA cm^{-2})	Areal capacity (mAh cm^{-2})	Charging voltage (V)	Cell type	Capacity retention	Ref.
NVP	1 m NaFSI DMTMSA/THF	0.3	1.5	3.8	Coin	~97.1% after 500 cycles	This work
	1 m NaFSI DMTMSA/THF	3.2	1.0	3.9	Coin	~98.1% after 500 cycles	This work
	1 m NaFSI DMTMSA/THF	5.0	1.0	4.0	Coin	~70% after 1500 cycles	This work
	1 m NaFSI DMTMSA/THF	0.3	1.2	3.8	Pouch	~96% after 125 cycles	This work
	5.2 M NaFSI DME	3.6	0.18	3.7	Coin	~48% after 40000 cycles	31
	2.1 M NaFSI DME:BTFE=1:2 (mol)	3.6	0.18	3.7	Coin	~91% after 40000 cycles	31
	0.75 M $NaClO_4$ FEC:PC=1:1 (wt)	6.0	0.10	3.8	Coin	~48% after 8000 cycles	68
	0.75 M $NaClO_4$ + 0.01 M LiTFSI FEC:PC=1:1 (wt)	6.0	0.10	3.8	Coin	~89% after 10000 cycles	68
	NaTFSI:[Pyr13][FSI]: TFEE=1:3:1 (mol)	1.35	0.27	3.8	Coin	~95% after 2000 cycles	69
	1.0 M $NaPF_6$ FEC:DMC=1:1 (vol) TTE/DMTP additives	0.4	0.4	4.0	Coin	~89% after 1000 cycles	70
	1.0 M $NaPF_6$ Diglyme	2.2	1.1	3.9	Coin	~93% after 160 cycles	52
	1.0 M $NaPF_6$ Diglyme	2.2	1.1	3.9	Coin	~96% after 800 cycles (SF-Na)	52
NMO	1 m NaFSI DMTMSA/THF	0.3	1.0	3.8	Coin	~78% after 600 cycles	This work
	1.0 M $NaPF_6$ Diglyme: Me-THF=1:1 (vol)	0.23	0.45	3.6	Coin	~80% after 500 cycles	55
	1.0 M $NaPF_6$ Diglyme: THF=3:2 (vol)	0.23	0.45	3.6	Coin	~80% after 210 cycles	55
	NaFSI:Diglyme:HFME =1:1.17:3.82 (mol)	0.6	0.3	4.2	Coin	~87% after 350 cycles	43

Table S4. The composition of hybrid solvating electrolytes.

No.	Salt(s)	Molar ratio	Strong solvent(s)	Molar ratio	Weak solvent(s)	Molar ratio
1	NaFSI	1.0	THF	13.9	/	/
2	NaFSI	1.0	/	/	DMTMSA	5.6
3	NaFSI	1.0	THF	3.2	DMTMSA	4.3
4	NaFSI	1.0	THF	2.4	DMTMSA	4.7
5	NaFSI	1.0	THF	1.6	DMTMSA	5.0
6	NaFSI	1.0	THF	1.3	DMTMSA	5.1
7	NaFSI	1.0	THF	0.9	DMTMSA	5.3
8	NaFSI	1.0	Diglyme	0.8	DMTMSA	5.6
9	NaFSI	1.0	THF	1.5	Pip-TMSA	4.7
10	NaFSI	1.0	THF	1.5	Pyr-TMSA	5.0
11	NaFSI	1.0	THF	1.5	DETMSA	4.9
12	NaFSI	1.0	THF	3.0	Mor-TMSA	4.6
13	NaTFSI	1.0	THF	2.3	DMTMSA	5.6
14	NaFTFSI	1.0	THF	1.5	DMTMSA	5.6
15	NaFSI	1.0	DME	0.8	DMTMSA	5.6
16	NaFSI	1.0	DME	1.4	DMTMSA	5.6
17	NaFSI	1.0	DEE	0.9	DMTMSA	5.6
18	NaFSI	1.0	DEE	1.4	DMTMSA	5.6
19	NaFSI	1.0	TGDE	0.6	DMTMSA	5.6
20	NaFSI	1.0	TGDE	1.1	DMTMSA	2.2
21	NaFSI	1.0	TEGDME	0.6	DMTMSA	5.6
22	NaFSI	1.0	FEC	1.9	DMTMSA	5.6
23	NaFSI	1.0	TM	0.6	DMTMSA	5.6
24	NaFSI	1.0	/	/	[Pyr14][FSI] DMTMSA	1.3 5.6
25	NaFSI	1.0	THF	0.8	[Pyr14][FSI] DMTMSA	0.4 5.6
26	NaFSI	1.0	THF	1.1	[Pyr14][FSI] DMTMSA	0.3 5.6

No.	Salt(s)	Molar ratio	Strong solvent(s)	Molar ratio	Weak solvent(s)	Molar ratio
27	NaFSI	1.0	THF	1.5	DMTMSA DETMSA Pip-TMSA Pyr-TMSA	1.4 1.2 1.2 1.2
28	NaTFSI	1.0	FEC	3.7	DMTMSA	6.3
29	NaTFSI	1.0	DME	1.5	DMTMSA	5.7
30	NaTFSI	1.0	TM	6.8	DMTMSA	6.0
31	NaFSI	1.0	/	/	Me-THF DMTMSA	1.5 5.6
32	NaFSI	1.0	/	/	Cl-DEE DMTMSA	1.2 5.6
33	NaFSI	1.0	THF	1.5	DMTMSA DETMSA Pip-TMSA Mor-TMSA Pyr-TMSA	1.1 1.0 1.0 1.0 0.9
34	NaFSI	1.0	THF	1.4	DMTMSA DETMSA Mor-TMSA Pyr-TMSA	1.4 1.2 1.2 1.2
35	NaFSI	1.0	THF	2.0	DMTMSA DETMSA Pip-TMSA Mor-TMSA	1.4 1.2 1.2 1.2
36	NaFSI	1.0	THF FEC	2.0 0.2	DMTMSA DETMSA Mor-TMSA Pyr-TMSA	1.4 1.2 1.2 1.2
37	NaFSI	1.0	DME	1.3	DMTMSA DETMSA Mor-TMSA Pyr-TMSA	0.7 0.7 0.7 0.7
38	NaFSI	1.0	TMS	0.6	DMTMSA	5.6
39	NaFSI	1.0	TMS	1.1	DMTMSA	5.6
40	NaFSI	1.0	PS	0.6	DMTMSA	5.6
41	NaFSI	1.0	DTD	0.6	DMTMSA	5.6
42	NaFSI	1.0	THF DME	0.7 0.9	DMTMSA	5.6
43	NaFSI	1.0	FEC DME	0.7 0.7	DMTMSA	5.6
44	NaFSI	1.0	DME	1.5	DMTMSA	2.6
45	NaFSI	1.0	DME	0.7	Cl-DEE DMTMSA	0.4 5.6
46	NaFSI	1.0	DME	0.7	Me-THF DMTMSA	0.7 5.6

No.	Salt(s)	Molar ratio	Strong solvent(s)	Molar ratio	Weak solvent(s)	Molar ratio
47	NaFSI	1.0	DME	2.0	[Pyr14][FSI] DMTMSA	0.6 3.9
48	NaFSI	1.0	TMS DME	0.6 0.8	DMTMSA	5.6
49	NaFSI	1.0	THF FEC	0.6 0.7	[Pyr14][FSI] DMTMSA	0.4 5.6
50	NaFSI	1.0	TMS THF DME FEC	0.2 0.4 0.3 0.3	[Pyr14][FSI] DMTMSA	0.1 5.6

References

1. Cao, R., Mishra, K., Li, X., Qian, J., Engelhard, M.H., Bowden, M.E., Han, K.S., Mueller, K.T., Henderson, W.A., Zhang, J.-G. (2016). Enabling room temperature sodium metal batteries. Nano Energy *30*, 825-830.
2. Li, Y., Zhou, Q., Weng, S., Ding, F., Qi, X., Lu, J., Li, Y., Zhang, X., Rong, X., Lu, Y., et al. (2022). Interfacial engineering to achieve an energy density of over 200 Wh kg^{-1} in sodium batteries. Nat. Energy *7*, 511-519.
3. Tian, Z., Zou, Y., Liu, G., Wang, Y., Yin, J., Ming, J., Alshareef, H.N. (2022). Electrolyte solvation structure design for sodium ion batteries. Adv. Sci. *9*, 2201207.
4. Zhu, Y., Leverick, G., Accogli, A., Gordiz, K., Zhang, Y., Shao-Horn, Y. A high-rate and high-efficiency molten-salt sodium–oxygen battery. Energy Environ. Sci. *15*, 4636-4646
5. Sayahpour, B., Li, W., Bai, S., Lu, B., Han, B., Chen, Y.-T., Deysher, G., Parab, S., Ridley, P., Raghavendran, G., et al. (2024). Quantitative analysis of sodium metal deposition and interphase in Na metal batteries. Energy Environ. Sci. *17*, 1216-1228.
6. Schmuch, R., Wagner, R., Hörpel, G., Placke, T., Winter, M. (2018). Performance and cost of materials for lithium-based rechargeable automotive batteries. Nat. Energy *3*, 267-278.
7. Seh, Z.W., Sun, J., Sun, Y., Cui, Y. (2015). A highly reversible room-temperature sodium metal anode. ACS Cent. Sci. *1*, 449-455.
8. Deng, Y., Zheng, J., Zhao, Q., Yin, J., Biswal, P., Hibi, Y., Jin, S., Archer, L.A. (2022). Highly reversible sodium metal battery anodes via alloying heterointerfaces. Small *18*, 2203409.
9. Ji, Y., Qiu, J., Zhao, W., Liu, T., Dong, Z., Yang, K., Zheng, G., Qian, G., Yang, M., Chen, Q., et al. (2023). In situ probing the origin of interfacial instability of Na metal anode. Chem *9*, 2943-2955.
10. Dai, T., Wu, S., Lu, Y., Yang, Y., Liu, Y., Chang, C., Rong, X., Xiao, R., Zhao, J., Liu, Y., et al. (2023). Inorganic glass electrolytes with polymer-like viscoelasticity. Nat. Energy *8*, 1221-1228.

11. Liu, Q., Zhang, L., Sun, H., Geng, L., Li, Y., Tang, Y., Jia, P., Wang, Z., Dai, Q., Sheng, T., et al. (2020). In situ observation of sodium dendrite growth and concurrent mechanical property measurements using an environmental transmission electron microscopy−atomic force microscopy (ETEM-AFM) platform. ACS Energy Lett. *5*, 2546-2559.

12. Niu, Y., Hu, Z., Zhang, B., Xiao, D., Mao, H., Zhou, L., Ding, F., Liu, Y., Yang, Y., Xu, J., et al. (2023). Earth-abundant Na-Mg-Fe-Mn-O cathode with reversible hybrid anionic and cationic redox. Adv. Energy Mater. *13*, 2300746.

13. He, J., Bhargav, A., Su, L., Lamb, J., Okasinski, J., Shin, W., Manthiram, A. Tuning the solvation structure with salts for stable sodium-metal batteries. Nat. Energy *9*, 446-456.

14. Liu, X., Zhao, J., Dong, H., Zhang, L., Zhang, H., Gao, Y., Zhou, X., Zhang, L., Li, L., Liu, Y., et al. (2024). Sodium difluoro(oxalato)borate additive-induced robust SEI and CEI layers enable dendrite-free and long-cycling sodium-ion batteries. Adv. Funct. Mater. *34*, 2402310.

15. Bao, C., Wang, B., Liu, P., Wu, H., Zhou, Y., Wang, D., Liu, H., Dou, S. (2020). Solid electrolyte interphases on sodium metal anodes. Adv. Funct. Mater. *30*, 2004891.

16. Chen, W., Salvatierra, R.V., Li, J.T., Luong, D.X., Beckham, J.L., Li, V.D., La, N., Xu, J., Tour, J.M. (2022). Brushed metals for rechargeable metal batteries. Adv. Mater. *34*, 2202668.

17. Jiang, K., Xu, S., Guo, S., Zhang, X., Zhang, X., Qiao, Y., Fang, T., Wang, P., He, P., Zhou, H. (2018). A phase-transition-free cathode for sodium-ion batteries with ultralong cycle life. Nano Energy *52*, 88-94.

18. Wang, P.-F., You, Y., Yin, Y.-X., Guo, Y.-G. (2018). Layered oxide cathodes for sodium-ion batteries: phase transition, air stability, and performance. Adv. Energy Mater. *8*, 1701912.

19. Han, B., Li, X., Wang, Q., Zou, Y., Xu, G., Cheng, Y., Zhang, Z., Zhao, Y., Deng, Y., Li, J., et al. (2022). Cryo-electron tomography of highly deformable and adherent solid-electrolyte interphase exoskeleton in Li-metal batteries with ether-based electrolyte. Adv. Mater. *34*, 2108252.

20. Hu, J., Wang, H., Yuan, F., Wang, J., Zhang, H., Zhao, R., Wu, Y., Kang, F., Zhai, D. (2024). Deciphering the formation and accumulation of solid-electrolyte interphases in Na and K carbonate-based batteries. Nano Lett. *24*, 1673-1678.

21. Gao, L., Chen, J., Chen, Q., Kong, X. (2022). The chemical evolution of solid electrolyte interface in sodium metal batteries. Sci. Adv. *8*, eabm4606.

22. Li, X., Zhao, L., Li, P., Zhang, Q., Wang, M.-S. (2017). In-situ electron microscopy observation of electrochemical sodium plating and stripping dynamics on carbon nanofiber current collectors. Nano Energy *42*, 122-128.

23. Zeng, Z., Barai, P., Lee, S.-Y., Yang, J., Zhang, X., Zheng, W., Liu, Y.-S., Bustillo, K.C., Ercius, P., Guo, J., et al. (2020). Electrode roughness dependent electrodeposition of sodium at the nanoscale. Nano Energy 72, 104721.

24. Yang, H., He, F., Li, M., Huang, F., Chen, Z., Shi, P., Liu, F., Jiang, Y., He, L., Gu, M., et al. (2021). Design principles of sodium/potassium protection layer for high-power high-energy sodium/potassium-metal batteries in carbonate electrolytes: a case study of Na_2Te/K_2Te. Adv. Mater. *33*, 2106353.

25. Zhuang, R., Zhang, X., Qu, C., Xu, X., Yang, J., Ye, Q., Liu, Z., Kaskel, S., Xu, F., Wang, H. (2023). Fluorinated porous frameworks enable robust anode-less sodium metal batteries. Sci. Adv. *9*, eadh8060.

26. Yuan, X., Liu, B., Mecklenburg, M., Li, Y. (2023). Ultrafast deposition of faceted lithium polyhedra by outpacing SEI formation. Nature *620*, 86-91.

27. Chen, X., Li, Z., Zhao, H., Li, J., Li, W., Han, C., Zhang, Y., Lu, L., Li, J., Qiu, X. (2024). Dominant solvent-separated ion pairs in electrolytes enable superhigh conductivity for fast-charging and low-temperature lithium ion batteries. ACS Nano *18*, 8350-8359.

28. Zhong, S., Yu, Y., Yang, Y., Yao, Y., Wang, L., He, S., Yang, Y., Liu, L., Sun, W., Feng, Y., et al. (2023). Molecular engineering on solvation structure of carbonate electrolyte toward durable sodium metal battery at -40 ^{o}C. Angew. Chem. Int. Ed. *62*, e202301169.

29. Fang, H., Huang, Y., Hu, W., Song, Z., Wei, X., Geng, J., Jiang, Z., Qu, H., Chen, J., Li, F. (2024). Regulating ion-dipole interactions in weakly solvating electrolyte towards ultra-low temperature sodium-ion batteries. Angew. Chem. Int. Ed. *63*, e202400539.

30. Wang, S., Zhang, X.-G., Gu, Y., Tang, S., Fu, Y. (2024). An ultrastable low-temperature Na metal battery enabled by synergy between weakly solvating solvents. J. Am. Chem. Soc. *146*, 3854-3860.

31. Zheng, J., Chen, S., Zhao, W., Song, J., Engelhard, M.H., Zhang, J.-G. (2018). Extremely stable sodium metal batteries enabled by localized high-concentration electrolytes. ACS Energy Lett. *3*, 315-321.

32. Kim, S.C., Wang, J., Xu, R., Zhang, P., Chen, Y., Huang, Z., Yang ,Y., Yu, Z., Oyakhire, S.T., Zhang, W., et al. (2023). High-entropy electrolytes for practical lithium metal batteries. Nat. Energy *8*, 814-826.

33. Lin, Y., Yu, Z., Yu, W., Liao, S.-L., Zhang, E., Guo, X., Huang, Z., Chen, Y., Qin, J., Cui, Y., et al. (2024). Impact of the fluorination degree of ether-based electrolyte solvents on Li-metal battery performance. J. Mater. Chem. A, *12*, 2986-2993.

34. Xue, W., Huang, M., Li, Y., Zhu, Y.G., Gao, R., Xiao, X., Zhang, W., Li, S., Xu, G., Yu, Y., et al. (2021). Ultra-high-voltage Ni-rich layered cathodes in practical Li metal batteries enabled by a sulfonamide-based electrolyte. Nat. Energy *6*, 495-505.

35. Yu, Z., Wang, H., Kong, X., Huang, W., Tsao, Y., Mackanic, D.G., Wang, .K., Wang, X., Huang, W., Choudhury, S., et al. (2020). Molecular design for electrolyte solvents enabling energy-dense and long-cycling lithium metal batteries. Nat. Energy *5*, 526-533.

36. Li, A.-M., Borodin, O., Pollard, T.P., Zhang, W., Zhang, N., Tan, S., Chen, F., Jayawardana, C., Lucht, B.L., Hu, E., et al. (2024). Methylation enables the use of fluorine-free ether electrolytes in high-voltage lithium metal batteries. Nat. Chem. *16*, 922-929.

37. Mao, M., Gong, L., Wang, X., Wang, Q., Zhang, G., Wang, H., Xie, W., Suo, L., Wang, C. (2024). Electrolyte design combining fluoro-with cyano-substitution solvents for anode-free Li metal batteries. Proc. Natl. Acad. Sci. *121*, e2316212121.

38. Li, G.-X., Koverga, V., Nguyen, A., Kou, R., Ncube, M., Jiang, H., Wang, K., Liao, M., Guo, H., Chen, J., et al. (2024). Enhancing lithium-metal battery longevity through minimized coordinating diluent. Nat. Energy *9*, 817-827.

39. Zhang, J., Zhang, H., Weng, S., Li, R., Lu, D., Deng, T., Zhang, S., Lv, L., Qi, J., Xiao, X., et al. (2023). Multifunctional solvent molecule design enables high-voltage Li-ion batteries. Nat. Commun. *14*, 2211.

40. Chen, J., Zhang, H., Fang, M., Ke, C., Liu, S., Wang, J. (2023). Design of localized high-concentration electrolytes via donor number. ACS. Energy Lett. *8*, 1723-1734.

41. Wu, Y., Hu, Q., Liang, H., Wang, A., Xu, H., Wang, L., He, X. (2023). Electrostatic potential as solvent descriptor to enable rational electrolyte design for lithium batteries. Adv. Energy Mater. *13*, 2300259.

42. Zhao, Y., Zhou, T., Jeurgens, L.P.H., Kong, X., Choi, J.K., Coskun, A. (2023). Electrolyte engineering for highly inorganic solid electrolyte interphase in high-performance lithium metal batteries. Chem *9*, 682-697.

43. Li, J., Sui, S., Zhou, X., Lei, K., Yang, Q., Chu, S., Li, L., Zhao, Y., Gu, M., Chou, S., et al. (2024). Weakly coordinating diluent modulated solvation chemistry for high-performance sodium metal batteries. Angew. Chem. Int. Ed. *63*, e202400406.

44. Jin, Y., Le, P.M.L., Gao, P., Xu, Y., Xiao, B., Engelhard, M.H., Cao, X., Vo, T.D., Hu, J., Zhong, L., et al. (2022). Low-solvation electrolytes for high-voltage sodium-ion batteries. Nat. Energy *7*, 718-725.

45. Hobold, G.M., Lopez, J., Guo, R., Minafra, N., Banerjee, A., Meng, Y.S., Shao-Horn, Y., Gallant, B.M. (2021). Moving beyond 99.9% Coulombic efficiency for lithium anodes in liquid electrolytes. Nat. Energy *6*, 951-960.

46. Boyle, D.T., Li, Y., Pei, A., Vila, R.A., Zhang, Z., Sayavong, P., Kim, M.S., Huang, W., Wang, H., Liu, Y., et al. (2022). Resolving current-dependent regimes of electroplating mechanisms for fast charging lithium metal anodes. Nano Lett. *22*, 8224-8232.

47. Ko, S., Obukata, T., Shimada, T., Takenaka, N., Nakayama, M., Yamada, A., Yamada, Y. (2022). Electrode potential influences the reversibility of lithium-metal anodes. Nat. Energy *7*, 1217-1224.

48. Lu, Z., Geng, C., Yang, H., He, P., Wu, S., Yang, Q.-H., Zhou, H. (2022). Step-by-step desolvation enables high-rate and ultra-stable sodium storage in hard carbon anodes. Proc. Natl. Acad. Sci. *119*, e2210203119.

49. Kim, S., Lee, J.-A., Lee, T.K., Baek, K., Kim, J., Kim, B., Byun, J.H., Lee, H.W., Kang, S.J., Choi, J.-A., et al. (2023). Wide-temperature-range operation of lithium-metal batteries using partially and weakly solvating liquid electrolytes. Energy Environ. Sci. *16*, 5108-5122.

50. Ma, B., Lee, Y., Bai, P. (2021) Dynamic interfacial stability confirmed by microscopic optical operando experiments enables high-retention-rate anode-free Na metal full cells. Adv. Sci. *8*, 2005006.

51. Xie, H., Cheng, .H, Kumar, P., Wang, Y., Liang, H., Cai, T., Zhao, F., Cao, Z., Cavallo, L., Ma, Z., et al. (2024). Thermodynamic and kinetic behaviors of electrolytes mediated by intermolecular interactions enabling high-performance lithium-ion batteries. ACS Nano *18*, 22503-22517.

52. Wang, C., Zheng, Y., Chen, Z.N., Zhang, R., He, W., Li, K., Yan, S., Cui, J., Fang, X., Yan, J., et al. (2023). Robust anode-free sodium metal batteries enabled by artificial sodium formate interface. Adv. Energy Mater. *13*, 2204125.

53. Yu, Q., Xiao, Y., Zhao, S., Miao, Y., Wan S., Zhou, L., Rong, J., Hou, G., Chen, S. (2024). All-fluorinated low-solvation electrolytes for high-voltage sodium metal batteries with appealing stability. Adv. Funct. Mater. *34*, 2401868.

54. Ren, Y., Lai, T., Manthiram, A. (2023). Reversible sodium−sulfur batteries enabled by a synergistic dual-additive design. ACS Energy Lett. *8*, 2746-2752.

55. Vaidyula, R.R., Nguyen, M.H., Weeks, J.A., Wang, Y., Wang, Z., Kawashima, K., Paul-Orecchio, A.G., Celio, H., Dolocan, A., Henkelman, G., et al. (2024). Binary solvent induced stable interphase layer for ultra-long life sodium metal batteries. Adv. Mater. *36*, 2312508.

56. Kilgallon, L.J., Shao-Horn, Y., Johnson, J.A. (2023). Safe and scalable syntheses of N,N-dimethyltrifluoromethanesulfonamide (DMTMSA) and Other trifluoromethanesulfonamide solvents for high energy density battery applications. J. Org. Chem. *88*, 16644-16648.

57. Noviandri, I., Brown, K.N., Fleming, D.S., Gulyas, P.T., Lay, P.A., Masters, A.F., Phillips, L. (1999). The decamethylferrocenium/decamethylferrocene redox couple: A superior

redox standard to the ferrocenium/ferrocene redox couple for studying solvent effects on the thermodynamics of electron transfer. J. Phys. Chem. B *103*, 6713–6722.

58. Hobold, G.M., Kim, K.-H., Gallant, B.M. (2023). Beneficial vs. inhibiting passivation by the native lithium solid electrolyte interphase revealed by electrochemical Li^+ exchange. Energy Environ. Sci. 16, 2247–2261.

59. Zeng, Y., Smith, R.B., Bai, P., Bazant, M.Z. (2014). Simple formula for Marcus–Hush–Chidsey kinetics. J. Electroanal. Chem. *735*, 77–83.

60. Kirilov, A., Mintun, E., Ravi, N., Mao, H., Rolland, C., Gustafson, L., Xiao, T., Whitehead, S., Berg, A.C., Lo, W.Y., et al. (2023). Segment anything. arXiv:2304.02643.

61. Parrish, R.M., Burns, L.A., Smith, D.G.A., Simmonett, A.C., DePrince, III, A.G., Hohenstein, E.G., Bozkaya, U., Sokolov, A.Y., Remigio, R.D., Richard, R.M., et al. (2017). Psi4 1.1: An open-source electronic structure program emphasizing automation, advanced libraries, and interoperability. J. Chem. Theory Comput. *13*, 3185-3197.

62. Mitternacht, S. (2016). FreeSASA: An open source C library for solvent accessible surface area calculations [version 1; peer review: 2 approved]. F1000Research 5, 189.

63. Wang, Y., Wang, J., Cao, Z., Farimani, A.B. (2022). Molecular contrastive learning of representations via graph neural networks. Nat. Mach. Intell. *4*, 279-287.

64. Stenutz, R. Gutmann acceptor and donor number (retrieved July 27, 2024). https://www.stenutz.eu/chem/solv21.php?sort=6

65. Plimpton, S. (1995). Fast parallel algorithms for short-range molecular dynamics. J. Comput. Phys. *117*, 1-19.

66. Jorgensen, W.L., Maxwell, D.S., Tirado-Rives, J. (1996). Development and testing of the OPLS all-atom force field on conformational energetics and properties of organic liquids. J. Am. Chem. Soc. *118*, 11225-11236.

67. Dodda, L.S., Vilseck, J.Z.; Tirado-Rives, J., Jorgensen, W.L. (2017). 1.14*CM1A-LBCC: Localized bond-charge corrected CM1A charges for condensed-phase simulations. J. Phys. Chem. B *121*, 3864-3870.

68. Wan, S., Song, K., Chen, J., Zhao, S., Ma, W., Chen, W., Chen, S. (2023). Reductive competition effect-derived solid electrolyte interphase with evenly scattered inorganics enabling ultrahigh rate and long-life span sodium metal batteries. J. Am. Chem. Soc. *145*, 21661-21671.

69. Liu, Y., Lu, S., Wang, Z., Xu, J., Weng, S., Xue, J., Tu, H., Zhang, F., Liu, L., Gao, Y., et al. (2024). Weakly polar ether-aided ionic liquid electrolyte enables high-performance sodium metal batteries over wide temperature range. Adv. Funct. Mater. *34*, 2312295.

70. Liu, X., Zheng, X., Deng, Y., Qin, X., Huang, Y., Dai, Y., Wu, W., Wang, Z., Luo, W. (2021). Implanting a fire-extinguishing alkyl in sodium metal battery electrolytes via a functional molecule. Adv. Funct. Mater. *32*, 2109378.